FINAL REPORT - VOLUME 2 OF 2

"*Numerical Simulation of 3-D Shock Wave
Turbulent Boundary Layer Interaction Using a Two
Equation Model of Turbulence*"

Doyle D. Knight
Department of Mechanical and Aerospace Engineering
Rutgers University - The State University of New Jersey
PO Box 909
Piscataway, NJ   08855-0909
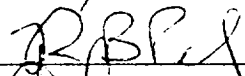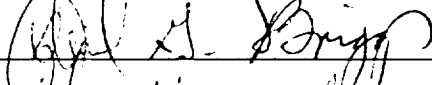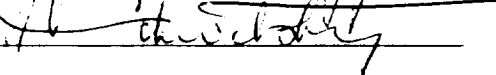
Grant Period: 1 July 1992 - 31 October 1995

NUMERICAL SIMULATION OF 3-D SHOCK WAVE TURBULENT BOUNDARY LAYER INTERACTION USING A TWO EQUATION MODEL OF TURBULENCE.

BY MARIANNA GNEDIN

A dissertation submitted to the

Graduate School—New Brunswick

Rutgers, The State University of New Jersey

in partial fulfillment of the requirements

for the degree of

Doctor of Philosophy

Graduate Program in Mechanical and Aerospace Engineering

Written under the direction of

Professor Doyle D. Knight

and approved by

_____

_____

_____

_____

New Brunswick, New Jersey

May, 1996

Numerical Simulation of 3-D Shock Wave Turbulent Boundary Layer Interaction Using a Two Equation Model of Turbulence.

by Marianna Gnedin, Ph.D.

Dissertation Director: Professor Doyle D. Knight

A computational study of the crossing shock wave-turbulent boundary layer interaction is presented. The shock waves are generated by a pair of fins which are mounted normal to a flat plate and form a converging channel. The focus of the study is to investigate the ability of the theoretical turbulence model to provide for improvement in the predictions of adiabatic wall temperature and heat transfer rates during the interaction of the shock waves with the turbulent boundary layer on the flat plate. Three configurations with fin angles of $15° \times 15°$, $7° \times 11°$ and $7° \times 7°$ have been examined at Mach 3.9. Experimental data available for comparison includes surface pressure, heat transfer, adiabatic wall temperature and surface flow visualization. Computations solve the 3-D Reynolds-averaged compressible Navier-Stokes equations incorporating the new low Reynolds number correction of Knight to the two equation $k-\epsilon$ turbulence model. The computed surface pressure displays good agreement with experiment. The computed adiabatic wall temperature exhibits excellent agreement with experiment. The computed and experimental surface and flowfield flow visualization are in general agreement. The computed surface heat transfer displays significant disagreement with experiment for some cases. The flowfield manifests a complex shock wave system, and a pair of counter-rotating vortices.

Acknowledgements

Table of Contents

List of Tables

List of Figures

List of Abbreviations

a speed of sound.

c_f skin friction coefficient.

c_h heat transfer coefficient.

c_p specific heat at constant pressure.

e total energy per unit mass.

H total enthalpy.

h enthalpy.

i grid point number in ξ direction.

I unit matrix.

j grid point number in η direction.

J Jacobian of transformation.

k turbulence kinetic energy.

k grid point number in ζ direction.

M Mach number.

M_t turbulent Mach number.

n time step number.

$\hat{n}$ unit vector normal to surface.

N_ξ number of grid points in ξ direction.

N_η number of grid points in η direction.

N_ζ number of grid points in ζ direction.

p pressure.

Pr Prandtl number.

Pr_t turbulent Prandtl number.

Q flow variable vector.

$q_\mathbf{w}$ heat flux at the wall.

R Universal gas constant.

Re_δ Reynolds number based on upstream boundary layer thickness.

t time.

T temperature.

u x-direction velocity.

v y-direction velocity.

w z-direction velocity.

x, y, z physical coordinates.

y^+ yu_τ/ν_w.

Greek letters

α_1 angle of the left fin

α_2 angle of the right fin

Δx grid spacing in streamwise direction.

Δy grid spacing in vertical direction.

Δz grid spacing in spanvise direction.

γ ratio of specific heats.

ϵ dissipation rate of turbulence energy.

ϵ_d dilatation dissipation.

ϵ_s solenoidal dissipation.

μ dynamic viscosity.

μ_T turbulent eddy viscosity.

μ_w dynamic viscosity at the bottom wall.

ν kinematic viscosity.

ν_T kinematic turbulent eddy viscosity.

ν_w kinematic viscosity at the bottom wall.

ρ density.

τ_w shear stress at the wall.

ξ, η, ζ transformed coordinates.

subscripts

w   wall.

i grid number in ξ direction.

j grid number in η direction.

k grid number in ζ direction.

∞ freestream values.

ξ, η, ζ derivative with respect to corresponding coordinate.

superscripts

n "time step" number.

Chapter 1

INTRODUCTION

1.1 Motivation

Shock wave/turbulent boundary layer interactions commonly occur in a wide range of applications and have strong influence on the characteristics of the flow. The flow pattern of such type of flows commonly involves strong viscous/inviscid interactions, separation of the boundary layer caused by shock waves and formation of large vortical structures.

An important class of flows involving shock wave-turbulent boundary layer interaction is the so called "crossing shock" flow (Fig. 1.1). In this type of flows two intersecting shock waves are generated by two sharp fins mounted on a flat plate. These shock waves interact with the developed boundary layer on the bottom flat plate surface. An adequate understanding of the flow structure caused by the crossing shock wave/turbulent boundary layer interaction and the ability of the theoretical model to accurately predict the surface pressure distribution and heat transfer rates on the bottom surface is crucial for the improved design of supersonic aircraft components such as hypersonic aircraft inlets.

The computed flows generally exhibit good agreement with experimental data for surface pressure, shock structure, and boundary layer profiles of pitot pressure and yaw angle. However the accurate prediction of the surface heat transfer and friction coefficient remains a challenging problem. [19, 24, 40]. While the surface pressure is to a large extent determined by the inviscid flow structure and therefore is not strongly affected by the particular choice of the theoretical turbulence model, the derivative quantities (e.g., surface heat transfer) crucially depend on the turbulence treatment. Consequently, one of the biggest challenges for accurately computing the crossing shock
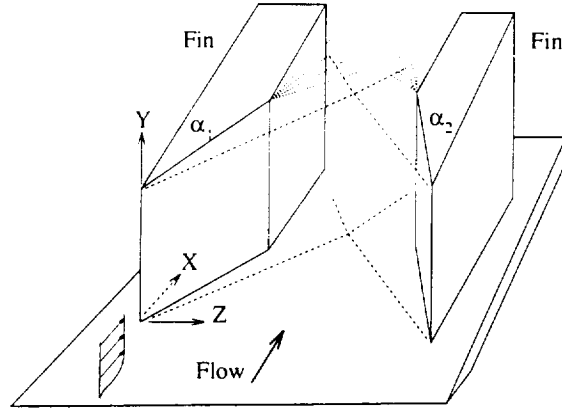
Figure 1.1: Crossing shock ("double fin")

interactions is the modeling of the turbulence quantities of such flows.

The two equation $k - \epsilon$ model is the most common choice since it can in principle better predict complex flowfields than algebraic models and is significantly simpler than sophisticated higher order closures [55]. A major difficulty in the implementation of the $k-\epsilon$ model is the treatment of the near wall region, where the classical high Re number $k-\epsilon$ model is not valid. Alternative approaches are the so called "wall function boundary conditions" which are imposed in the wall layer [61], or a "two-layer $k - \epsilon$ model", when a different model is considered in the near wall region (like Rodi model[46]). However, for many engineering applications, particularly for that involving separation of the boundary layer or when the transport properties are needed, it is desirable to enable integration to the boundary. For this purpose wall damping functions can be introduced which lead to the creation of the so-called "low Reynolds number $k - \epsilon$ model". The examples of the low Reynolds number models include those developed by Jones and Launder [21], Launder and Sharma [33], Lam and Bremhorst [32], Chien [9] and many others. Significant research efforts have been invested into the validation of different turbulence models for the computation of flows with shock wave/boundary layer interaction, in particular, flows with crossing shock interactions (see Table 1.1 for references).

The low Reynolds number model of Knight utilized in the present numerical study is described in detail in [6]. The focus of the present research is to investigate the applicability of this turbulent model to the numerical simulation of the flow involving

the crossing shock wave/boundary layer interaction.

Table 1.1: Crossing Shock Computations

Ref.	M_∞	α_1	α_2	Model
[44]	3.5	10°	10°	B-L
[42]	3	11°	11°	B-L, J-L
[18]	4	15°	15°	B-L
[43]	8.3	10°	10°	B-L
[41]	8.3	15°	15°	B-L, Rodi
[15]	8.3	15°	15°	B-L
[2], [3]	8.3	15°	15°	W,LS,SST,BL
[24]	4	7°	11°	Chien
		11°	15°	
[61]	4	7°	11°	Knight-RSE
Present	4	7°	11°	Knight-$k - \epsilon$
		7°	7°	

LEGEND

α_1	left fin angle	
α_2	right fin angle	
M_∞	freestream Mach number	
B-L	Baldwin-Lomax model	[1]
Chien	Chien model	[9]
J-L	Jones-Launder model	[21]
Knight-RSE	Knight RSE model	[20]
Knight-$k - \epsilon$	Knight model	[6]
LS	Launder-Sharma model	[33]
Rodi	Rodi model	[46]
SST	Menter model	[36]
W	Wilcox $k - \omega$ model	[54]

1.2 Literature Survey

Shock wave-turbulent boundary layer interactions have long been within one of the most interesting and challenging problems in Computational Fluid Dynamics. Significant progress has been achieved in understanding and numerical simulation of geometrically simple flows involving "dimensionless" geometries, such as swept compression corner [25], [29], [30], [50], [57], or a sharp single fin [13], [14], [23], [26], [27], [28], [45], [57]. The principal features of the shock wave-turbulent boundary layer interaction caused

by a single fin, such as bifurcation of the main inviscid shock into separation shock and rear shock, which together with a slip line constitute a quasi-conical λ-shaped wave structure, are summarized, for example, in [10].

In recent years substantial research efforts have been concentrated on flows involving more complex 3-D shock wave/turbulent boundary layer interaction, in particularly, crossing shock ("double fin") interactions, where two sharp fins are mounted on a bottom flat plate to form a converging wedge (Fig. 1.1). Understanding of such flows is important due to applications to high speed inlets. One of the objectives of the inlet design is to obtain a nearly uniform high total pressure flow at the inlet exit [11], [12]. However, flow separation and complex shock pattern can lead to a substantial loss of total pressure and nonuniform pressure distribution in the flow to the engine. Consequently, an adequate understanding of the flow physics and the ability to accurately predict it computationally is very important for improved design of inlets.

Focusing on this relatively simple geometric configuration allows us to separate the complexity associated with the flow physics and turbulence modeling from that caused by sophisticated geometry.

A review of theoretical and experimental studies of the crossing shock interactions can be found in [10], [19],[24]. Available experimental data includes surface pressure, surface flow visualization and, in some cases, measurements of derivative quantities such as skin friction and heat transfer rates with 10-15 % accuracy [4], [16], [17], [31], [35], [56], [62]. Computational studies are very important to improve the understanding of the flow physics and also as an important tool in the design of supersonic inlets.

Significant research efforts have been concentrated on the development and evaluation of turbulence models capable of providing accurate predictions of the flow structure, surface loads and heat transfer rates on the bottom flat plate surface. Turbulence models involved in "double fin" computations range from zero-equation algebraic to two-equation $k - \epsilon$ and $k - \omega$ and full RSE models. Some of the recent computations are summarized in the Table (1.1).

The computed surface pressure and boundary layer profiles of total pressure and yaw angle are relatively insensitive to the choice of the turbulence model, since they

are determined by the inviscid flow structure [10]. These quantities are predicted with reasonable accuracy in most of the computations. However the computed surface heat transfer strongly depends on the particular choice of the turbulence model involved in the computations [19, 40].

The low Reynolds number model of Knight, described in detail in [6], is developed on the basis of three principles, namely, 1) the model employs the physical dissipation rate $\tilde{\epsilon}$, 2) the normal distance y is avoided, and 3) the minimum number of modifications are introduced, as described by Speziale [52]. The modifications include incorporation of molecular diffusion of k and $\tilde{\epsilon}$, modification of the turbulent eddy viscosity μ_T to provide proper asymptotic behavior near the wall, and modification of the dissipation of $\tilde{\epsilon}$ to avoid singularities in the $\tilde{\epsilon}$ equation near the wall.

1.3 Present Research

The objective of the present research is to validate the low Reynolds number correction of Knight to the standard $k - \epsilon$ model in application to the numerical simulation of the flow involving the crossing shock wave/boundary layer interaction. The double fin configuration utilized in the experiments of Zheltovodov *et al.* [62] is considered. Computational results are extensively compared to the experimental results for all cases. Comparison to the previous computational results of Knight *et al.* [24] using the Chein's model and of Zha and Knight using the full Reynolds stress equation model [61] is also reported for the heat transfer rate.

In the present thesis three configurations were considered with $M_\infty = 3.95$, namely, $7° \times 11°$, $7° \times 7°$ and $15° \times 15°$, corresponding to the experiments of Zheltovodov and his colleagues [62].

The governing equations and the turbulence model equations are presented in Chapter 2. The numerical algorithm is described in detail in Chapter 3. The CRAFT Reynolds averaged Navier-Stokes solver is described in detail in [37].

The solver has been modified to incorporate a new low Reynolds number correction to the two equation $k - \epsilon$ model. Chapter 3 also contains details about the boundary

conditions used for the present numerical simulations. Chapter 4 discusses the code validation study for a number of cases through comparison with analytical results and 2-D turbulent boundary layer test computations. Chapter 5 specifies the problem itself. Chapter 6 consists of the results of the present study. Chapter 7 provides a summary of the important results and future work.

Chapter 2

GOVERNING EQUATIONS

This chapter describes the 3-D steady Reynolds-Averaged compressible Navier-Stokes equations and the compressible $k - \epsilon$ turbulence model equations written in conservation form.

2.1 Equations in Cartesian Coordinates

The instantaneous compressible, three-dimensional Navier-Stokes equations in conservation form can be expressed in Cartesian coordinates in the following form using the Einstein summation convention:

- **Conservation of Mass (Continuity)**

$$\frac{\partial \rho}{\partial t} + \frac{\partial(\rho u_k)}{\partial x_k} = 0 \tag{2.1}$$

- **Conservation of Momentum**

$$\frac{\partial(\rho u_i)}{\partial t} + \frac{\partial(\rho u_i u_k)}{\partial x_k} = -\frac{\partial p}{\partial x_i} + \frac{\partial(\tau_{ik})}{\partial x_k} \tag{2.2}$$

- **Conservation of Energy**

$$\frac{\partial(\rho e)}{\partial t} + \frac{\partial[u_k(\rho e + p)]}{\partial x_k} = -\frac{\partial Q_k}{\partial x_k} + \frac{\partial(u_i \tau_{ik})}{\partial x_k} \tag{2.3}$$

The density, ρ, static pressure, p, and the absolute temperature, T, obey the equation of state :

$$p = \rho R T = \rho(\gamma - 1)\{e - \frac{1}{2}u_i u_i\} \tag{2.4}$$

where R is the Universal gas constant, $e = c_v T + \frac{1}{2}u_k u_k$ is the total energy per unit mass, and γ is the ratio of specific heats.

The Reynolds Averaged Navier-Stokes equations are:

- **Reynolds Averaged Conservation of Mass**

$$\frac{\partial \bar{\rho}}{\partial t} + \frac{\partial(\bar{\rho}\tilde{u}_k)}{\partial x_k} = 0 \tag{2.5}$$

- **Reynolds Averaged Conservation of Momentum**

$$\frac{\partial(\bar{\rho}\tilde{u}_i)}{\partial t} + \frac{\partial(\bar{\rho}\tilde{u}_i\tilde{u}_k)}{\partial x_k} = -\frac{\partial \bar{p}}{\partial x_i} + \frac{\partial(-\overline{\rho u_i'' u_k''} + \bar{\tau}_{ik})}{\partial x_k} \tag{2.6}$$

- **Reynolds Averaged Conservation of Energy**

$$\frac{\partial(\bar{\rho}\tilde{e})}{\partial t} + \frac{\partial[\tilde{u}_k(\bar{\rho}\tilde{e} + \bar{p})]}{\partial x_k} = \frac{\partial(-c_p\overline{\rho T'' u_k''} - \bar{Q}_k)}{\partial x_k} +$$
$$\frac{\partial}{\partial x_k}\left(-\overline{\rho u_j'' u_k''}\tilde{u}_j - \frac{1}{2}\overline{\rho u_j'' u_j'' u_k''} + \tilde{u}_j\bar{\tau}_{jk} + \overline{u_j''\tau_{jk}}\right) \tag{2.7}$$

In equations (2.5) - (2.7), $\bar{\rho}$ is the mean density, $\tilde{u}_k$ is the mass-averaged velocity, $\bar{p}$ is the mean pressure, and $\tilde{e}$ is the mass-averaged total energy per unit mass given by:

$$\tilde{e} = c_v\tilde{T} + \frac{1}{2}\tilde{u}_k\tilde{u}_k + \tilde{k} \tag{2.8}$$

where c_v is the specific heat at constant volume and $\tilde{k}$ is the mass-averaged turbulent kinetic energy defined by:

$$\bar{\rho}\tilde{k} = \frac{1}{2}\overline{\rho u_k'' u_k''}. \tag{2.9}$$

The overbar denotes ensemble average, *i.e.*,

$$\bar{f} = \lim_{n\to\infty} \frac{1}{n}\sum_{\nu=1}^{\nu=n} f^{(\nu)} \tag{2.10}$$

where $f^{(\nu)}$ are the individual realizations of the variable $f(x, y, z, t)$. The mass-averaged variable $\tilde{f}$ is defined as the mass-weighted ensemble average,

$$\tilde{f} = \frac{1}{\bar{\rho}}\lim_{n\to\infty} \frac{1}{n}\sum_{\nu=1}^{\nu=n} (\rho f)^{(\nu)} \tag{2.11}$$

and the fluctuating variable f'' in the mass-averaged expansion is

$$f'' = f - \tilde{f} \tag{2.12}$$

Alternately, the fluctuating variable f' in the unweighted expansion is

$$f' = f - \bar{f} \tag{2.13}$$

The molecular viscous stress, $\bar{\tau}_{ik}$, is approximated by assuming a Newtonian fluid

$$\bar{\tau}_{ik} = \bar{\mu}\left(\frac{\partial \tilde{u}_k}{\partial x_i} + \frac{\partial \tilde{u}_i}{\partial x_k}\right) - \frac{2}{3}\bar{\mu}\frac{\partial \tilde{u}_j}{\partial x_j}\delta_{ik} \tag{2.14}$$

The dynamic molecular viscosity is assumed to be a function of averaged temperature and satisfy Sutherland's law:

$$\frac{\mu}{\mu_o} = \left(\frac{T}{T_o}\right)^{\frac{3}{2}}\frac{T_o + T_{\text{ref}}}{T + T_{\text{ref}}} \tag{2.15}$$

where T_{ref} is the Sutherland's reference temperature ($110.3°K$ for air), and $\mu_o = \mu(T_o)$. The molecular Prandtl number, Pr (0.73 for air), and the specific heat at constant pressure, c_p, are assumed constant.

The molecular heat flux, $\bar{Q}_k$, is approximated by assuming the Fourier heat law

$$\bar{Q}_k = -\frac{c_p\bar{\mu}}{Pr}\frac{\partial \tilde{T}}{\partial x_k} \tag{2.16}$$

where Pr is the molecular Prandtl number and c_p is the specific heat at constant pressure.

2.2   Low Reynolds Number Correction

The low Reynolds number modification of Knight to the standard $k - \epsilon$ model is described in detail in [6], and its application to adiabatic and isothermal compressible turbulent boundary layers is also presented in the paper [6].

2.2.1 $k - \epsilon$ Turbulence Model Equations

The set of Reynolds-averaged equations (2.5 - 2.7) is not closed due to the presence of the turbulent stress $-\overline{\rho u_i'' u_j''}$ and turbulent heat flux $-c_p\overline{\rho T'' u_k''}$. Two more transport equations for $\tilde{k}$ and $\tilde{\epsilon}$ are employed in order to close the system of governing equations. The turbulence model equations employed in present work are fully described in [6].

The standard two-equation $k - \epsilon$ model of Jones and Launder [21], extended formally to compressible flow and employing the compressibility correction of Sarkar *et al* [49] and Zeman [58], is chosen in [6] for fully turbulent high Reynolds number regions of the flow. The equation for the turbulence kinetic energy $\tilde{k}$ is taken in [6] to be

$$\frac{\partial \bar{\rho}\tilde{k}}{\partial t} + \frac{\partial \bar{\rho}\tilde{k}\tilde{u}_i}{\partial x_i} = -\overline{\rho u_i'' u_j''} \frac{\partial \tilde{u}_i}{\partial x_j} - \bar{\rho}\tilde{\epsilon} + \frac{\partial}{\partial x_i}\left(\frac{\mu_T}{\bar{\rho}\sigma_k}\frac{\partial \bar{\rho}\tilde{k}}{\partial x_i}\right) \quad (2.17)$$

where the dissipation is a combination of solenoidal $\tilde{\epsilon}_v$ and compressible $\tilde{\epsilon}_d$ components

$$\tilde{\epsilon} = \tilde{\epsilon}_v + \tilde{\epsilon}_d \quad (2.18)$$

and [49, 58]

$$\tilde{\epsilon}_d = C_k M_t^2 \tilde{\epsilon}_v \quad (2.19)$$

where M_t is the turbulence Mach number

$$M_t^2 = \frac{2\tilde{k}}{\gamma R\tilde{T}} \quad (2.20)$$

and C_k is a constant.

The equation for the solenoidal dissipation is

$$\frac{\partial \bar{\rho}\tilde{\epsilon}_v}{\partial t} + \frac{\partial \bar{\rho}\tilde{u}_i\tilde{\epsilon}_v}{\partial x_i} = -C_{\epsilon 1}\frac{\tilde{\epsilon}_v}{\tilde{k}}\overline{\rho u_i'' u_j''}\frac{\partial \tilde{u}_i}{\partial x_j} - C_{\epsilon 2}\bar{\rho}\frac{\tilde{\epsilon}_v^2}{\tilde{k}} + \frac{\partial}{\partial x_i}\left(\frac{\mu_T}{\sigma_\epsilon}\frac{\partial \tilde{\epsilon}_v}{\partial x_i}\right) \quad (2.21)$$

The turbulent stresses are

$$-\overline{\rho u_i'' u_j''} = \mu_T\left(\frac{\partial \tilde{u}_i}{\partial x_j} + \frac{\partial \tilde{u}_j}{\partial x_i} - \frac{2}{3}\frac{\partial \tilde{u}_k}{\partial x_k}\delta_{ij}\right) - \frac{2}{3}\bar{\rho}\tilde{k}\delta_{ij} \quad (2.22)$$

and the turbulent heat flux is

$$-c_p\overline{\rho T'' u_i''} = c_p\frac{\mu_T}{Pr_t}\frac{\partial \tilde{T}}{\partial x_i} \quad (2.23)$$

where the turbulent eddy viscosity is

$$\mu_T = \bar{\rho}C_\mu\frac{\tilde{k}^2}{\tilde{\epsilon}} \quad (2.24)$$

The turbulence model constants are based on the standard values [55] and are presented in Table 2.1. The constant C_k is taken to be zero, since dilatational dissipation is expected to be small in non-hypersonic boundary layers [7].

The equations (2.17) and (2.24) are valid only within fully turbulent regions of the flow. In order to integrate the governing equations to the solid boundary the low Reynolds number modification is developed in [6].

Table 2.1: Standard $k - \epsilon$ Model Constants

Constant	Value
C_μ	0.09
C_{ϵ_1}	1.44
C_{ϵ_2}	1.92
Pr_t	0.9
σ_k	1.0
σ_ϵ	1.3

2.2.2 The Low Reynolds Number Correction of Knight

The advantages of the low Reynolds number model of Knight, compared to other low Reynolds number corrections, are as follows: 1) the model employs the physical dissipation rate $\bar{\epsilon}$, 2) the normal distance y is not used, and 3) the minimum number of modifications is introduced, as described by Speziale [52].

The equation for the turbulence kinetic energy (2.17) is modified, first, by formally incorporating molecular diffusion of $\bar{k}$.

$$\frac{\partial \bar{\rho} \bar{k}}{\partial t} + \frac{\partial \bar{\rho} \bar{k} \tilde{u}_i}{\partial x_i} = -\overline{\rho u_i'' u_j''} \frac{\partial \tilde{u}_i}{\partial x_j} - \bar{\rho} \bar{\epsilon} + \frac{\partial}{\partial x_i} \left(\frac{\mu_T}{\bar{\rho} \sigma_k} \frac{\partial \bar{\rho} \bar{k}}{\partial x_i} + \bar{\mu} \frac{\partial \bar{k}}{\partial x_i} \right) \qquad (2.25)$$

Second, the turbulent eddy viscosity is modified by a dimensionless factor f_μ to provide the correct asymptotic behavior of the turbulent stresses close to a solid boundary

$$\mu_T = \bar{\rho} C_\mu f_\mu \frac{\bar{k}^2}{\bar{\epsilon}} \qquad (2.26)$$

where

$$f_\mu = \mathcal{O}(y^{-1}) \qquad \text{as} \quad y \to 0$$

$$f_\mu \to 1 \qquad \text{as} \quad y \to \infty \qquad (2.27)$$

The equation for the solenoidal dissipation is modified by incorporating molecular diffusion of $\bar{\epsilon}_v$ and including the dimensionless function f_2 for the dissipation term

$$\frac{\partial \bar{\rho} \bar{\epsilon}_v}{\partial t} + \frac{\partial \bar{\rho} \tilde{u}_i \bar{\epsilon}_v}{\partial x_i} = -C_{\epsilon 1} \frac{\bar{\epsilon}_v}{\bar{k}} \overline{\rho u_i'' u_j''} \frac{\partial \tilde{u}_i}{\partial x_j} - C_{\epsilon 2} f_2 \bar{\rho} \frac{\bar{\epsilon}_v^2}{\bar{k}} + \frac{\partial}{\partial x_i} \left[\left(\frac{\mu_T}{\sigma_\epsilon} + \bar{\mu} \right) \frac{\partial \bar{\epsilon}_v}{\partial x_i} \right] (2.28)$$

where asymptotic analysis [52] indicates $f_2 = \mathcal{O}(y^2)$ as $y \to 0$, and $f_2 \to 1$ as $y \to \infty$.

The dimensionless function f_2 is taken to be

$$f_2 = 1 - e^{-C_{\epsilon_3}\sqrt{R_t}} \tag{2.29}$$

where R_t is the turbulence Reynolds number

$$R_t = \frac{\bar{\rho}\bar{k}^2}{\bar{\mu}\bar{\epsilon}} \tag{2.30}$$

This provides the proper asymptotic behavior near the wall assuming $\epsilon \to \epsilon_w$ as $y \to 0$ where ϵ_w is the (positive) value of the turbulence kinetic energy dissipation at the wall, and $\bar{k} = \mathcal{O}(y^2)$ as $y \to 0$. The dimensionless constant C_{ϵ_3} is determined by comparison with Direct Numerical Simulation (DNS) results.

The functional form of f_μ and the constant C_{ϵ_3} in f_2 were determined through consideration of the viscous sublayer and logarithmic region of an incompressible flat plate turbulent boundary layer (i.e., the "constant stress layer"). In this region, convective effects were neglected and the model equations became (the tilda is omitted for convenience)

$$0 = \frac{\partial}{\partial y}\left(-\overline{\rho u''v''} + \mu\frac{\partial u}{\partial y}\right) \tag{2.31}$$

$$0 = -\overline{\rho u''v''}\frac{\partial u}{\partial y} - \rho\epsilon + \frac{\partial}{\partial y}\left[\left(\frac{\mu_T}{\sigma_k} + \mu\right)\frac{\partial k}{\partial y}\right] \tag{2.32}$$

$$0 = -C_{\epsilon_1}\frac{\epsilon}{k}\overline{\rho u''v''}\frac{\partial u}{\partial y} - C_{\epsilon_2}f_2\frac{\rho\epsilon^2}{k} + \frac{\partial}{\partial y}\left[\left(\frac{\mu_T}{\sigma_\epsilon} + \mu\right)\frac{\partial\epsilon}{\partial y}\right] \tag{2.33}$$

where the Reynolds shear stress is

$$-\overline{\rho u''v''} = \mu_T\frac{\partial u}{\partial y} \tag{2.34}$$

and

$$\mu_T = \rho C_\mu f_\mu\frac{k^2}{\epsilon} \tag{2.35}$$

The superscript $\tilde{\ }$ is omitted since the flow is incompressible, and ϵ denotes ϵ_v.

The boundary conditions at the wall were

$$u = 0 \tag{2.36}$$

$$k = 0 \tag{2.37}$$

$$\epsilon = \frac{2\mu}{\rho}\left(\frac{\partial\sqrt{k}}{\partial y}\right)^2 \tag{2.38}$$

and the asymptotic boundary conditions for $y \to \infty$ were [55]

$$u = \frac{u_*}{\kappa} \ln\left(\frac{yu_*}{\nu}\right) + Bu_* \tag{2.39}$$

$$k = \frac{u_*^2}{\sqrt{C_\mu}} \tag{2.40}$$

$$\epsilon = \frac{u_*^3}{\kappa y} \tag{2.41}$$

where $u_* \equiv \sqrt{\tau_w/\rho}$ is the local friction velocity.

For the incompressible constant stress layer, the following form of the turbulent eddy viscosity is assumed

$$\mu_T = \begin{cases} \rho\kappa u_* y_m \left[2\left(\frac{y}{y_m}\right)^3 - \left(\frac{y}{y_m}\right)^5\right] & \text{for } y \leq y_m \\ \rho\kappa u_* y & \text{for } y > y_m \end{cases} \tag{2.42}$$

The functional form for μ_T satisfies the appropriate asymptotic forms [55, 52] as $y \to 0$ and $y \to \infty$, and is continuously differentiable for all y.

The momentum equation (2.31) is directly integrated in [6], using (2.34) and (2.42) and subject to boundary conditions (2.36) and (2.39). The constant B in (2.39) depends on the value of y_m. It was verified that $y_m = 33.0\nu/u_*$ yields $B = 5.0$ in agreement with experiment [38].

The turbulence model equations (2.32) and (2.33) were solved in [6] for k and ϵ subject to boundary conditions (2.37), (2.38), (2.40) and (2.41). The constant C_{ϵ_3} was determined by requiring $\epsilon_w = 0.26u_*^4/\nu$ in agreement with the Direct Numerical Simulations (DNS) of Spalart [51] for a flat plate turbulent boundary layer. This yields $C_{\epsilon_3} = 0.17$. Comparison of the predicted and DNS profiles for ϵ are presented in Fig. 2.2 where $\epsilon^+ \equiv \epsilon\nu/u_*^4$.

The dimensionless function f_μ is then obtained from (2.35) as a function of R_t. The functions f_2 and f_μ are shown in Fig. 2.1. These functions are employed without modification for the compressible 3-D studies. The low Reynolds number modifications are summarized in Table 2.2.

The model was tested on a series of 2-D flat plate boundary layer computations with zero and adverse pressure gradient[6]. Computations were performed for incompressible and compressible, isothermal and adiabatic boundary layers with Mach number up
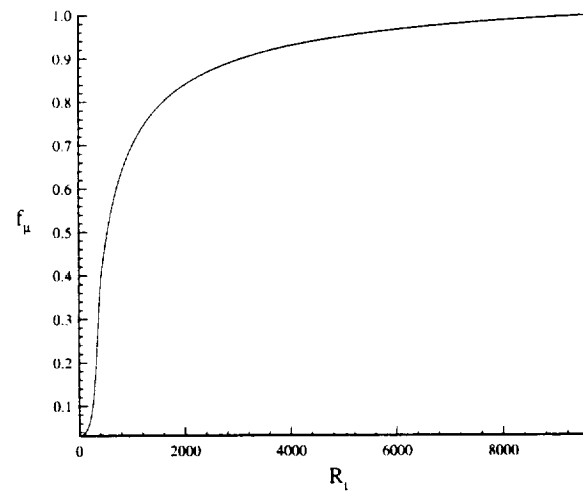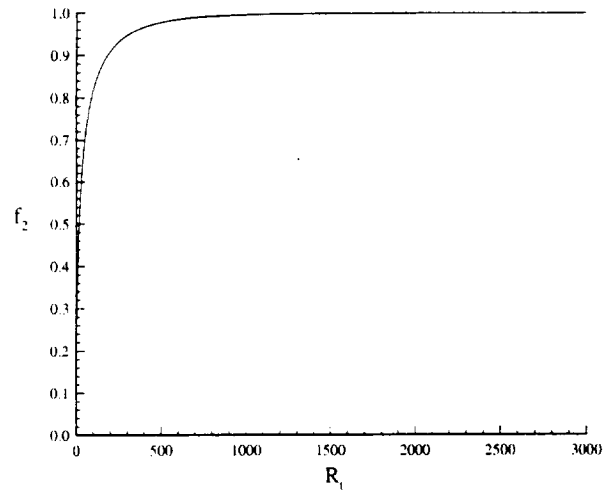
[22]

Figure 2.1: Functions f_2 and f_μ
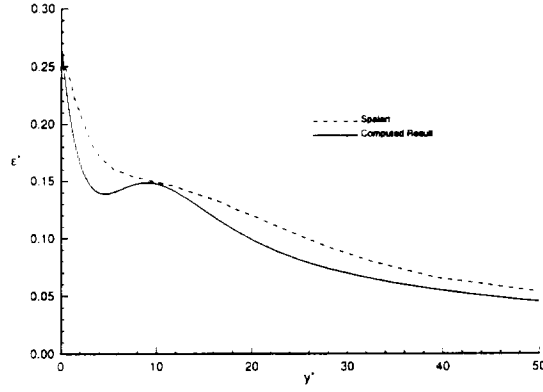
Figure 2.2: Predicted and DNS Results for ϵ

to 6. Good agreement with experiment was obtained for skin friction, heat transfer, adiabatic wall temperature and velocity profiles for the constant pressure flat plate boundary layers. Results for the adverse pressure gradient boundary layer showed close agreement with experimental velocity and Mach number and disagreement for the surface skin friction and Reynolds shear stress.

Table 2.2: Low Reynolds Number Functions

Function	Expression
$f_2(Re_t)$	$1 - e^{-C_{\epsilon 3}\sqrt{R_t}}$ where $C_{\epsilon_3} = 0.17$
$f_\mu(Re_t)$	See Fig. 2.1

2.3 Nondimensionalization

The governing equations are nondimensionalized according to the Table (2.3), where a superscript $*$ denotes a dimensional parameter.

The following nondimensional parameters are formed:

$$M_\infty \equiv \frac{U_\infty}{a_\infty}, \qquad a_\infty = \sqrt{\gamma R T_\infty}$$

$$Re \equiv \frac{U_\infty \rho_\infty \delta_o}{\mu_\infty}, \qquad Pr = \frac{\mu_\infty c_p}{\bar{k}_\infty}, \qquad Pr_t = Pr \frac{\mu_T}{k_T}$$

Here δ_o is the experimental incoming boundary layer thickness equal to 3.5 mm, $\bar{k}_\infty$ is the laminar thermal conductivity, Re is the Reynolds number, Pr, Pr_t are respectively, laminar and turbulent Prandtl number and subscript ∞ denotes freestream values in the incoming flow.

<div align="center">Table 2.3: Nondimensionalization</div>

Variable	Non-Dimensionalization	Variable	Non-Dimensionalization
x	$x^* = x\delta_o^*$	y	$y^* = y\delta_o^*$
z	$z^* = z\delta_o^*$	$\bar{u}$	$\bar{u}^* = \bar{u}U_\infty^*$
$\bar{v}$	$\bar{v}^* = \bar{v}U_\infty^*$	$\bar{w}$	$\bar{w}^* = \bar{w}U_\infty^*$
$\bar{\rho}$	$\bar{\rho}^* = \bar{\rho}\rho_\infty^*$	$\bar{p}$	$\bar{p}^* = \bar{p}\rho_\infty^* U_\infty^{*2}$
$\bar{\mu}$	$\bar{\mu}^* = \bar{\mu}\mu_\infty^*$	μ_T	$\mu_T^* = \mu_T\mu_\infty^*$
$\tilde{\epsilon}_v$	$\tilde{\epsilon}_v^* = \tilde{\epsilon}_v \frac{U_\infty^{*3}}{\delta_o^*}$	$\tilde{T}$	$\tilde{T}^* = \tilde{T}T_\infty^*$
$\bar{k}$	$\bar{k}^* = \bar{k}k_\infty^*$	k_T	$k_T^* = k_T k_\infty^*$
k	$k^* = k\rho_\infty^* U_\infty^{*2}$	t	$t^* = t\frac{\delta_o}{U_\infty^*}$

2.4 Equations in Body Fitted Coordinates

A stationary non-singular coordinate transformation is introduced $(x, y, z) \rightarrow (\xi, \eta, \zeta)$, where [22]

$$\xi = \xi(x, y, z) \tag{2.43}$$
$$\eta = \eta(x, y, z)$$
$$\zeta = \zeta(x, y, z)$$

The numerical flux $\mathcal{F}$ is an approximation of the average flux through the cell interface, which can be defined as, say,

$$\mathcal{F}_{\xi\eta} = \frac{1}{\Delta\xi\Delta\eta} \int_{\Delta\xi} \int_{\Delta\eta} \mathcal{F} d\xi d\eta \tag{2.44}$$

All numerical inviscid and viscous fluxes can be represented in a similar manner. The average dependent variables Q are defined for each cell volume as

$$Q = \frac{1}{\Delta\xi\Delta\eta\Delta\zeta} \int_{\Delta\xi} \int_{\Delta\eta} \int_{\Delta\zeta} Q \, d\xi \, d\eta \, d\zeta \qquad (2.45)$$

The grid steps in the transformed domain $\Delta\xi$, $\Delta\eta$ and $\Delta\zeta$ are taken to be unity without loss of generality.

All numerical fluxes are determined at cell interfaces, and dependent variables are defined at cell centroids.

With the transformation described above the Reynolds-averaged Navier-Stokes equations governing the flow of viscous turbulent gas and applied with respect to the generalized six-sided cell volume shown on Fig. (2.3) can be written in integral form as

$$\nu \frac{\partial Q}{\partial t} + \left(E_{i+1/2} - E_{i-1/2}\right) + \left(F_{j+1/2} - F_{j-1/2}\right) + \left(G_{k+1/2} - G_{k-1/2}\right)$$

$$= \left(R_{i+1/2} - R_{i-1/2}\right) + \left(S_{j+1/2} - S_{j-1/2}\right) + \left(T_{k+1/2} - T_{k-1/2}\right) + \nu D \qquad (2.46)$$

where ν is the cell volume, ξ,η and ζ are the generalized streamwise, body normal and meridional coordinates, respectively, Q is the vector of conserved variables per unit volume, $E,F,$ and G are the inviscid fluxes of dependent variables through the corresponding cell faces, integrated over the appropriate cell area, R, S and T are similar viscous fluxes and D is the turbulent source term. The indices i, j and k represent the cell location in the ξ, η and ζ coordinate directions of the computational mesh respectively. A non-whole index corresponds to the cell interface, and a whole index corresponds to the cell centroid.

The vector of conservative dependent variables and vectors of inviscid fluxes can be presented in a following way (from this point forward the overbar and tilda are omitted for clarity),

$$Q = \begin{pmatrix} \rho \\ \rho u \\ \rho v \\ \rho w \\ \rho e \\ \rho k \\ \rho\epsilon \end{pmatrix} ; E = \begin{pmatrix} \rho U \\ \rho u U + l_x p \\ \rho v U + l_y p \\ \rho w U + l_z p \\ (\rho e + p)U \\ \rho k U \\ \rho\epsilon U \end{pmatrix} ; F = \begin{pmatrix} \rho V \\ \rho u V + m_x p \\ \rho v V + m_y p \\ \rho w V + m_z p \\ (\rho e + p)V \\ \rho k V \\ \rho\epsilon V \end{pmatrix} ; G = \begin{pmatrix} \rho W \\ \rho u W + n_x p \\ \rho v W + n_y p \\ \rho w W + n_z p \\ (\rho e + p)W \\ \rho k W \\ \rho\epsilon W \end{pmatrix}$$
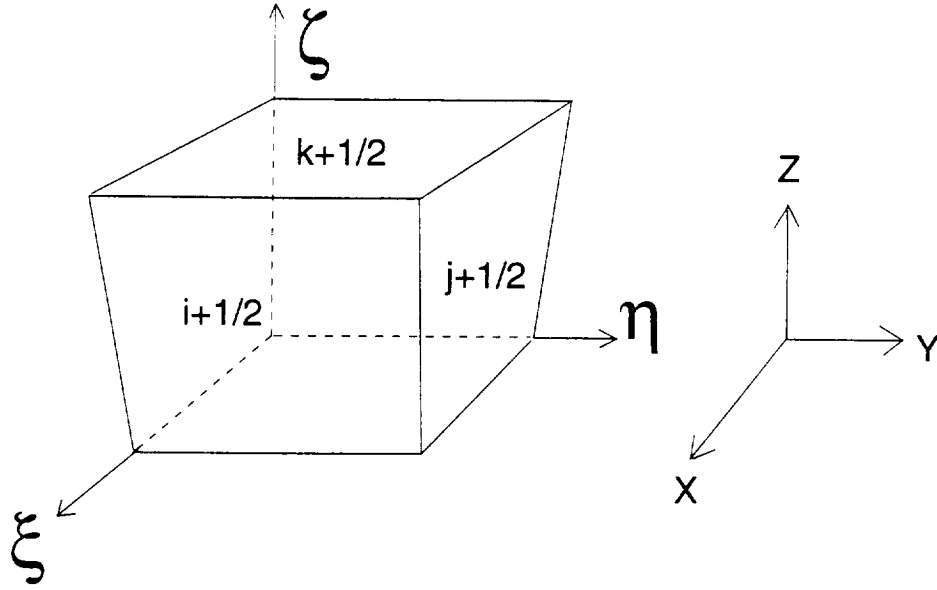
Figure 2.3: Three-dimensional finite volume cell.

Here the transformation metrics l_x, l_y etc. are x, y, or z components of vectors l, m and n. These three vectors have a direction of a normal on ξ, η or ζ faces, respectively, and magnitude equal to the area of the corresponding cell surface.

The volume fluxes through each family of cell interfaces U, V and W can be defined as dot products of velocity vector with the vectors l, m and n, as

$$
\begin{aligned}
U &= ul_x + vl_y + wl_z \\
V &= um_x + vm_y + wm_z \\
W &= un_x + vn_y + wn_z
\end{aligned}
\tag{2.47}
$$

The viscous flux vectors can be written in the following form:

$$
S = \frac{1}{\nu}
\begin{pmatrix}
0 \\
\alpha(b_1 u_\xi + b_2 u_\eta + b_3 u_\zeta + b_4 v_\xi + b_5 v_\eta + b_6 v_\zeta + b_7 w_\xi + b_8 w_\eta + b_9 w_\zeta) - \frac{2}{3}\rho k m_x \\
\alpha(b_{10} u_\xi + b_5 u_\eta + b_{11} u_\zeta + b_{12} v_\xi + b_{13} v_\eta + b_{14} v_\zeta + b_{15} w_\xi + b_{16} w_\eta + b_{17} w_\zeta) - \frac{2}{3}\rho k m_y \\
\alpha(b_{18} u_\xi + b_8 u_\eta + b_{19} u_\zeta + b_{20} v_\xi + b_{16} v_\eta + b_{21} v_\zeta + b_{22} w_\xi + b_{23} w_\eta + b_{24} w_\zeta) - \frac{2}{3}\rho k m_z \\
S_5 \\
\alpha_k \left(b_{26} k_\xi + b_{25} k_\eta + b_{27} k_\zeta \right) + \beta_k \left(b_{26} (\rho k)_\xi + b_{25} (\rho k)_\eta + b_{27} (\rho k)_\zeta \right) \\
\alpha_\epsilon \left(b_{26} \epsilon_\xi + b_{25} \epsilon_\eta + b_{27} \epsilon_\zeta \right)
\end{pmatrix}
\quad (2.48)
$$

Here S_5 and coefficients b are:

$$
\begin{aligned}
S_5 = {} & \alpha_Q \left(b_{25} T_\eta + b_{26} T_\xi + b_{27} T_\zeta \right) \\
& + \alpha \left(\frac{1}{2} b_2 \left(u^2 \right)_\eta + \frac{1}{2} b_{13} \left(v^2 \right)_\eta + \frac{1}{2} b_{23} \left(w^2 \right)_\eta + b_5 \left(uv \right)_\eta + b_8 \left(uw \right)_\eta + b_{16} \left(vw \right)_\eta \right) \\
& + \alpha \left(\left(b_1 u + b_{10} v + b_{18} w \right) u_\xi + \left(b_4 u + b_{12} v + b_{20} w \right) v_\xi + \left(b_7 u + b_{15} v + b_{22} w \right) w_\xi \right. \\
& \left. + \left(b_3 u + b_{11} v + b_{19} w \right) u_\zeta + \left(b_6 u + b_{14} v + b_{21} w \right) v_\zeta + \left(b_9 u + b_{17} v + b_{24} w \right) w_\zeta \right) \\
& - \frac{2}{3} \rho k \left(m_x u + m_y v + m_z w \right)
\end{aligned}
$$

$$
\begin{aligned}
b_1 &= \frac{4}{3} l_x m_x + l_y m_y + l_z m_z \\
b_2 &= \frac{4}{3} m_x^2 + m_y^2 + m_z^2 \\
b_3 &= \frac{4}{3} m_x n_x + m_y n_y + m_z n_z \\
b_4 &= -\frac{2}{3} l_y m_x + l_x m_y \\
b_5 &= \frac{1}{3} m_x m_y \\
b_6 &= -\frac{2}{3} m_x n_y + m_y n_x \\
b_7 &= -\frac{2}{3} l_z m_x + l_x m_z \\
b_8 &= \frac{1}{3} m_x m_z \\
b_9 &= -\frac{2}{3} m_x n_z + m_z n_x \\
b_{10} &= -\frac{2}{3} l_x m_y + l_y m_x
\end{aligned}
$$

$$b_{11} = -\frac{2}{3}m_y n_x + m_x n_y$$

$$b_{12} = l_x m_x + \frac{4}{3}m_y l_y + m_z l_z$$

$$b_{13} = m_x^2 + \frac{4}{3}m_y^2 + m_z^2$$

$$b_{14} = m_x n_x + \frac{4}{3}m_y n_y + m_z n_z$$

$$b_{15} = -\frac{2}{3}l_z m_y + m_z l_y$$

$$b_{16} = \frac{1}{3}m_y m_z$$

$$b_{17} = -\frac{2}{3}m_y n_z + m_z n_y$$

$$b_{18} = -\frac{2}{3}l_x m_z + l_z m_x$$

$$b_{19} = -\frac{2}{3}m_z n_x + m_x n_z$$

$$b_{20} = -\frac{2}{3}l_y m_z + l_z m_y$$

$$b_{21} = -\frac{2}{3}m_z n_y + m_y n_z$$

$$b_{22} = l_x m_x + l_y m_y + \frac{4}{3}l_z m_z$$

$$b_{23} = m_x^2 + m_y^2 + \frac{4}{3}m_z^2$$

$$b_{24} = m_x n_x + m_y n_y + \frac{4}{3}m_z n_z$$

$$b_{25} = m_x^2 + m_y^2 + m_z^2$$

$$b_{26} = m_x l_x + m_y l_y + m_z l_z$$

$$b_{27} = m_x n_x + m_y n_y + m_z n_z$$

$$R = \frac{1}{\nu}\begin{pmatrix} 0 \\ \alpha(c_1 u_\xi + c_2 u_\eta + c_3 u_\zeta + c_4 v_\xi + c_5 v_\eta + c_6 v_\zeta + c_7 w_\xi + c_8 w_\eta + c_9 w_\zeta) - \frac{2}{3}\rho k l_x \\ \alpha(c_4 u_\xi + c_{10} u_\eta + c_{11} u_\zeta + c_{12} v_\xi + c_{13} v_\eta + c_{14} v_\zeta + c_{15} w_\xi + c_{16} w_\eta + c_{17} w_\zeta) - \frac{2}{3}\rho k l_y \\ \alpha(c_7 u_\xi + c_{18} u_\eta + c_{19} u_\zeta + c_{15} v_\xi + c_{20} v_\eta + c_{21} v_\zeta + c_{22} w_\xi + c_{23} w_\eta + c_{24} w_\zeta) - \frac{2}{3}\rho k l_z \\ R_5 \\ \alpha_k (c_{25} k_\xi + c_{26} k_\eta + c_{27} k_\zeta) + \beta_k \left(c_{25}(\rho k)_\xi + c_{26}(\rho k)_\eta + c_{27}(\rho k)_\zeta\right) \\ \alpha_\epsilon (c_{25}\epsilon_\xi + c_{26}\epsilon_\eta + c_{27}\epsilon_\zeta) \end{pmatrix} \quad (2.49)$$

Here R_5 and coefficients c are:

$$R_5 = \alpha_Q \left(c_{25} T_\xi + c_{26} T_\eta + c_{27} T_\zeta \right)$$

$$+ \alpha \left(\frac{1}{2} c_1 \left(u^2 \right)_\xi + \frac{1}{2} c_{12} \left(v^2 \right)_\xi + \frac{1}{2} c_{22} \left(w^2 \right)_\xi + c_4 \left(uv \right)_\xi + c_7 \left(uw \right)_\xi + c_{15} \left(vw \right)_\xi \right)$$

$$+ \alpha \left(\left(c_2 u + c_{10} v + c_{18} w \right) u_\xi + \left(c_5 u + c_{13} v + c_{20} w \right) v_\xi + \left(c_8 u + c_{16} v + c_{23} w \right) w_\xi \right.$$

$$+ \left(c_3 u + c_{11} v + c_{19} w \right) u_\zeta + \left(c_6 u + c_{14} v + c_{21} w \right) v_\zeta + \left(c_9 u + c_{17} v + c_{24} w \right) w_\zeta \right)$$

$$- \frac{2}{3} \rho k \left(l_x u + l_y v + l_z w \right)$$

$$c_1 = \frac{4}{3} l_x^2 + l_y^2 + l_z^2$$

$$c_2 = \frac{4}{3} l_x m_x + l_y m_y + l_z m_z$$

$$c_3 = \frac{4}{3} l_x n_x + l_y n_y + l_z n_z$$

$$c_4 = \frac{1}{3} l_x l_y$$

$$c_5 = -\frac{2}{3} l_x m_y + l_y m_x$$

$$c_6 = -\frac{2}{3} l_x n_y + l_y n_x$$

$$c_7 = \frac{1}{3} l_x l_z$$

$$c_8 = -\frac{2}{3} l_x m_z + l_z m_x$$

$$c_9 = -\frac{2}{3} l_x n_z + l_z n_x$$

$$c_{10} = -\frac{2}{3} l_y m_x + l_x m_y$$

$$c_{11} = -\frac{2}{3} l_y n_x + l_x n_y$$

$$c_{12} = l_x^2 + \frac{4}{3} l_y^2 + l_z^2$$

$$c_{13} = l_x m_x + \frac{4}{3} l_y m_y + l_z m_z$$

$$c_{14} = l_x n_x + \frac{4}{3} l_y n_y + l_z n_z$$

$$c_{15} = \frac{1}{3} l_y l_z$$

$$c_{16} = -\frac{2}{3} l_y m_z + l_z m_y$$

$$c_{17} = -\frac{2}{3} l_y n_z + l_z n_y$$

$$c_{18} = -\frac{2}{3} l_z m_x + l_x m_z$$

$$c_{19} = -\frac{2}{3}l_z n_z + l_x n_x$$

$$c_{20} = -\frac{2}{3}l_z m_y + l_y m_z$$

$$c_{21} = -\frac{2}{3}l_z n_y + l_y n_z$$

$$c_{22} = l_x^2 + l_y^2 + \frac{4}{3}l_z^2$$

$$c_{23} = l_x m_x + l_y m_y + \frac{4}{3}l_z m_z$$

$$c_{24} = l_x n_x + l_y n_y + \frac{4}{3}l_z n_z$$

$$c_{25} = l_x^2 + l_y^2 + l_z^2$$

$$c_{26} = l_x m_x + l_y m_y + l_z m_z$$

$$c_{27} = l_x n_x + l_y n_y + l_z n_z$$

$$
\left\{
\begin{array}{l}
\alpha(d_1 u_\xi + d_2 u_\eta + d_3 u_\zeta + d_4 v_\xi + d_5 v_\eta + d_6 v_\zeta + d_7 w_\xi + d_8 w_\eta + d_9 w_\zeta) - \frac{2}{3}\rho k \tau n_x \\[4pt]
\alpha(d_{10}u_\xi + d_{11}u_\eta + d_6 u_\zeta + d_{12}v_\xi + d_{13}v_\eta + d_{14}v_\zeta + d_{15}w_\xi + d_{16}w_\eta + d_{17}w_\zeta) - \frac{2}{3}\rho k \tau n_y \\[4pt]
\alpha(d_{18}u_\xi + d_{19}u_\eta + d_9 u_\zeta + d_{20}v_\xi + d_{21}v_\eta + d_{17}v_\zeta + d_{22}w_\xi + d_{23}w_\eta + d_{24}w_\zeta) - \frac{2}{3}\rho k \tau n_z \\[4pt]
0 \\[4pt]
T_5 \\[4pt]
\alpha_k(d_{27}k_\xi + d_{26}k_\eta + d_{25}k_\zeta) + \beta_k\left(d_{27}(\rho k)_\xi + d_{26}(\rho k)_\eta + d_{25}(\rho k)_\zeta\right) \\[4pt]
\alpha_\varepsilon(d_{27}\varepsilon_\xi + d_{26}\varepsilon_\eta + d_{25}\varepsilon_\zeta)
\end{array}
\right.
\qquad (2.50)
$$

$$T = \frac{1}{\nu}$$

Here T_5 and coefficients d are:

$$
\begin{aligned}
T_5 = {} & \alpha_Q(d_{25}T_\zeta + d_{26}T_\xi + d_{27}T_\eta) \\
& + \alpha\left(\frac{1}{2}d_3\left(u^2\right)_\zeta + \frac{1}{2}d_{14}\left(v^2\right)_\zeta + d_6\left(uv\right)_\zeta + d_9\left(uw\right)_\zeta + d_{17}\left(vw\right)_\zeta\right) \\
& +\alpha\big((d_1 u + d_{10}v + d_{18}w)u_\xi + (d_4 u + d_{12}v + d_{20}w)v_\xi + (d_7 u + d_{15}v + d_{22}w)w_\xi \\
& \quad + (d_2 u + d_{11}v + d_{19}w)u_\eta + (d_5 u + d_{13}v + d_{21}w)v_\eta + (d_8 u + d_{16}v + d_{23}w)w_\eta\big) \\
& -\frac{2}{3}\rho k(n_x u + n_y v + n_z w)
\end{aligned}
$$

$$d_1 = \frac{4}{3}l_x n_x + l_y n_y + l_z n_z$$

$$d_2 = \frac{4}{3}m_x n_x + m_y n_y + m_z n_z$$

$$d_3 = \frac{4}{3}n_x^2 + n_y^2 + n_z^2$$

$$d_4 = -\frac{2}{3}l_y n_x + l_x n_y$$

$$d_5 = -\frac{2}{3}m_y n_x + m_x n_y$$

$$d_6 = \frac{1}{3}n_x n_y$$

$$d_7 = -\frac{2}{3}l_z n_x + l_x n_z$$

$$d_8 = -\frac{2}{3}m_z n_x + m_x n_z$$

$$d_9 = \frac{1}{3}n_x n_z$$

$$d_{10} = -\frac{2}{3}l_x n_y + l_y n_x$$

$$d_{11} = -\frac{2}{3}m_x n_y + m_y n_x$$

$$d_{12} = l_x n_x + \frac{4}{3}n_y l_y + m_z l_z$$

$$d_{13} = m_x n_x + \frac{4}{3}m_y n_y + m_z n_z$$

$$d_{14} = n_x^2 + \frac{4}{3}n_y^2 + n_z^2$$

$$d_{15} = -\frac{2}{3}l_z n_y + n_z l_y$$

$$d_{16} = -\frac{2}{3}m_z n_y + m_y n_z$$

$$d_{17} = \frac{1}{3}n_y n_z$$

$$d_{18} = -\frac{2}{3}l_x n_z + l_z n_x$$

$$d_{19} = -\frac{2}{3}m_x n_z + m_z n_x$$

$$d_{20} = -\frac{2}{3}l_y n_z + l_z n_y$$

$$d_{21} = -\frac{2}{3}m_y n_z + m_z n_y$$

$$d_{22} = l_x n_x + l_y n_y + \frac{4}{3}l_z n_z$$

$$d_{23} = m_x n_x + m_y n_y + \frac{4}{3}m_z n_z$$

$$d_{24} = n_x^2 + n_y^2 + \frac{4}{3}n_z^2$$

$$d_{25} = n_x^2 + n_y^2 + n_z^2$$

$$d_{26} = m_x n_x + m_y n_y + m_z n_z$$

$$d_{27} = l_x n_x + l_y n_y + l_z n_z$$

Here $\mathcal{V}$ is an elemental volume in the physical domain,

$$\mathcal{V} = \int J^{-1} \left(\frac{\xi, \eta \zeta}{x, y, z} \right) d\xi d\eta d\zeta \tag{2.51}$$

with J being the Jacobian of the transformation,

$$J \equiv \frac{\partial (\xi, \eta, \zeta)}{\partial x, y, z}$$

The diffusion coefficients are defined as

$$\alpha = \frac{1}{\mathrm{Re}} (\mu + \mu_t) \qquad \alpha_Q = \frac{1}{(\gamma - 1) M_\infty^2} \frac{1}{\mathrm{Re}} \left(\frac{\mu_t}{Pr_t} + \frac{\mu}{Pr} \right)$$

$$\alpha_\epsilon = \frac{1}{\mathrm{Re}} \left(\mu + \frac{\mu_t}{\sigma_\epsilon} \right) \qquad \alpha_k = \mu \qquad \beta_k = \frac{\mu_t}{\rho \sigma_k}$$

The turbulent source terms can be presented as

$$D = \begin{pmatrix} P_k - \rho \epsilon \\ C_{\epsilon_1} \frac{\epsilon}{k} P_k - C_{\epsilon_2} f_2 \frac{\rho \epsilon^2}{k} \end{pmatrix} \tag{2.52}$$

The production term P_k in transformed coordinates is

$$
\begin{aligned}
P_k \;=\; & \frac{\mu_t}{\mathrm{Re}} \frac{1}{\mathcal{V}^2} \left\{ \left(u_\xi^2 + v_\xi^2 + w_\xi^2 \right) \left(l_x^2 + l_y^2 + l_z^2 \right) + \frac{1}{3} \left(u_\xi l_x + v_\xi l_y + w_\xi l_z \right)^2 \right. \\
& + \left(u_\eta^2 + v_\eta^2 + w_\eta^2 \right) \left(m_x^2 + m_y^2 + m_z^2 \right) + \frac{1}{3} \left(u_\eta m_x + v_\eta m_y + w_\eta m_z \right)^2 \\
& + \left(u_\zeta^2 + v_\zeta^2 + w_\zeta^2 \right) \left(n_x^2 + n_y^2 + n_z^2 \right) + \frac{1}{3} \left(u_\zeta n_x + v_\zeta n_y + w_\zeta n_z \right)^2 \\
& + 2 * \left[\left(u_\xi u_\eta + v_\xi v_\eta + w_\xi w_\eta \right) \left(l_x m_x + l_y m_y + l_z m_z \right) \right. \\
& + \left(u_\xi m_x + v_\xi m_y + w_\xi m_z \right) \left(u_\eta l_x + v_\eta l_y + w_\eta l_z \right) \\
& + \left(u_\xi u_\zeta + v_\xi v_\zeta + w_\xi w_\zeta \right) \left(l_x n_x + l_y n_y + l_z n_z \right) \\
& + \left(u_\xi n_x + v_\xi n_y + w_\xi n_z \right) \left(u_\zeta l_x + v_\zeta l_y + w_\zeta l_z \right) \\
& + \left(u_\eta u_\zeta + v_\eta v_\zeta + w_\eta w_\zeta \right) \left(m_x n_x + m_y n_y + m_z n_z \right) \\
& + \left(u_\eta n_x + v_\eta n_y + w_\eta n_z \right) \left(u_\zeta m_x + v_\zeta m_y + w_\zeta m_z \right) \\
& - \frac{2}{3} * \left(u_\xi l_x + v_\xi l_y + w_\zeta l_z \right) \left(u_\eta m_x + v_\eta m_y + w_\eta m_z \right) \\
& - \frac{2}{3} * \left(u_\xi l_x + v_\xi l_y + w_\zeta l_z \right) \left(u_\zeta n_x + v_\zeta n_y + w_\zeta n_z \right) \\
& \left. \left. - \frac{2}{3} * \left(u_\eta m_x + v_\eta m_y + w_\eta m_z \right) \left(u_\zeta n_x + v_\zeta n_y + w_\zeta n_z \right) \right] \right\} \\
& - \frac{2}{3} \frac{1}{\mathcal{V}} \rho k \left(u_\xi l_x + v_\xi l_y + w_\xi l_z + u_\eta m_x + v_\eta m_y + w_\eta m_z \right. \\
& \left. + u_\zeta n_x + v_\zeta n_y + w_\zeta n_z \right) \tag{2.53}
\end{aligned}
$$

Chapter 3

NUMERICAL ALGORITHM

The CRAFT code, originally designed to simulate the flow of viscous hypersonic chemically reacting gases by solving compressible Navier-Stokes equations in thin layer approximation [37], and modified by SAIC and CRAFT Corporations by incorporating turbulence $k-\epsilon$ equations, was utilized in the present research. Consequently, the current numerical algorithm is that employed in the CRAFT code, with several important changes. These changes include addition of cross-derivative viscous terms in order to consider full Navier-Stokes equations, a different implementation of certain boundary conditions, and incorporation of the low Reynolds number model of Knight.

The current problem of shock-boundary layer interaction requires a solution of the system of *full* Reynolds averaged Navier-Stokes equations, with no terms omitted. These equations in body fitted coordinates are listed in the previous chapter.

A shock-capturing approach allows to capture a complex pattern of flow field discontinuities without any prior knowledge about the flow structure. A Roe scheme together with TVD type second order correction of Chakravarthy [8] provides for high resolution of complex shock wave structure and other discontinuities. Shock waves in the present flow are sometimes weak and accurate determination of their location and strength might be important for accurate prediction of dynamic loading and heat transfer at the bottom solid wall.

The numerical method involves strong coupling between mean flow and turbulent model equations and is made fully implicit to eliminate restrictions on the step size of explicit schemes. It is necessary since the turbulence model equations contain highly nonlinear source terms, which are capable to make step size prohibitively small for an explicit scheme. The schemes are made implicit by fully linearizing all fluxes and source

terms.

3.0.1   First Order Inviscid Flux

The first order accurate numerical flux at a cell interface is determined with the help of the approximate Riemann solver developed by Roe [47], which provides an algorithm to express a flux of dependent variables through the cell interface based on the set of dependent variables to the left and to the right of the interface. The Roe's method consists in determination the flux change across each of the waves that emanate from the interface. Consider the inviscid flux $F_{j+\frac{1}{2}}$ in (2.46). It is expressed as

$$F_{j+\frac{1}{2}}^{1st} = \frac{1}{2}\left(F_j + F_{j+1} + \Delta F_{j+\frac{1}{2}}^- - \Delta F_{j+\frac{1}{2}}^+\right) \tag{3.1}$$

Here vector $\Delta F_{j+\frac{1}{2}}^+$ represents the flux changes associated with waves traveling in the positive η direction, and vector $\Delta F_{j+\frac{1}{2}}^-$ corresponds to the flux changes due to waves traveling in the negative η direction. An eigenvalue analysis of the Jacobian matrix $\frac{\partial F}{\partial Q}$ reveals the speed and direction of each wave (all Jacobian matrices are listed in appendix A). Let Λ be a diagonal matrix which consists of wave speeds, and let L and R denote the matrix of left and right eigenvectors respectively. All these three matrices are evaluated at the cell interface. The flux difference across the positive and negative velocity waves can be computed as follows,

$$
\begin{aligned}
\Delta F_{j+\frac{1}{2}}^+ &= \frac{1}{2}\left(R_{j+\frac{1}{2}}\left(\Lambda + |\Lambda|\right)_{j+\frac{1}{2}} L_{j+\frac{1}{2}}\right)\left(Q_{j+1} - Q_j\right) \\
&= \left(\frac{\partial F}{\partial Q}\right)^+ \left(Q_{j+1} - Q_j\right) \tag{3.2} \\
\Delta F_{j+\frac{1}{2}}^- &= \frac{1}{2}\left(R_{j+\frac{1}{2}}\left(\Lambda - |\Lambda|\right)_{j+\frac{1}{2}} L_{j+\frac{1}{2}}\right)\left(Q_{j+1} - Q_j\right) \\
&= \left(\frac{\partial F}{\partial Q}\right)^- \left(Q_{j+1} - Q_j\right) \tag{3.3}
\end{aligned}
$$

The matrices R, L and Λ are known functions of "Roe-averaged" dependent variables (see Appendix C) at the cell interface, which satisfy the criteria:

$$F_{j+1} - F_j = \left[\left(\frac{\partial F}{\partial Q} \right)^+ + \left(\frac{\partial F}{\partial Q} \right)^- \right]^{\text{Roe}}_{j+\frac{1}{2}} (Q_{j+1} - Q_j)$$

(3.4)

The "Roe-averaged" variables are

$$u_{j+\frac{1}{2}} = \frac{u_j\sqrt{\rho_j} + u_{j+1}\sqrt{\rho_{j+1}}}{\sqrt{\rho_j} + \sqrt{\rho_{j+1}}}$$

$$v_{j+\frac{1}{2}} = \frac{v_j\sqrt{\rho_j} + v_{j+1}\sqrt{\rho_{j+1}}}{\sqrt{\rho_j} + \sqrt{\rho_{j+1}}}$$

$$w_{j+\frac{1}{2}} = \frac{w_j\sqrt{\rho_j} + w_{j+1}\sqrt{\rho_{j+1}}}{\sqrt{\rho_j} + \sqrt{\rho_{j+1}}}$$

$$h_{j+\frac{1}{2}} = \frac{h_j\sqrt{\rho_j} + h_{j+1}\sqrt{\rho_{j+1}} + \frac{1}{2}\sqrt{\rho_j}\sqrt{\rho_{j+1}}\left[(u_{j+1} - u_j)^2 + (v_{j+1} - v_j)^2 + (w_{j+1} - w_j)^2\right]}{\sqrt{\rho_j} + \sqrt{\rho_{j+1}}}$$

It is common to include some sort of entropy fix in the definition of upwind flux in the regions where one of wave speeds changes sign. However, it was shown in [60] that such approach gives significant error in the boundary layer, where the wave speed is close to zero. No entropy fix was used in the present research.

3.0.2 Second Order Correction

A higher order inviscid numerical flux is obtained by adding a correction to the first order flux. The higher order flux can be expressed as:

$$F^{\text{HO}}_{j+\frac{1}{2}} = F^{\text{1st}}_{j+\frac{1}{2}} \quad -R_{j+\frac{1}{2}}\Lambda^-_{j+\frac{1}{2}}\left(\frac{(1-\phi)}{4}\left[\Delta\widetilde{\alpha_{j+\frac{3}{2}}}\right] + \frac{(1+\phi)}{4}\left[\Delta\widetilde{\alpha_{j+\frac{3}{2}}}\right] \right)$$

$$+R_{j+\frac{1}{2}}\Lambda^+_{j+\frac{1}{2}}\left(\frac{(1+\phi)}{4}\left[\Delta\widetilde{\alpha_{j+\frac{1}{2}}}\right] + \frac{(1-\phi)}{4}\left[\Delta\widetilde{\alpha_{j-\frac{1}{2}}}\right] \right)$$

(3.5)

with $\phi = 1/3$ which provides for the 3—$^{\text{rd}}$ order accurate representation. The characteristic variable difference is defined as

$$\Delta\alpha_{j+\frac{1}{2}} = L_{j+\frac{1}{2}}(Q_{j+1} - Q_j)$$

(3.6)

The characteristic variables are limited in order to avoid nonphysical oscillations in the regions with sharp gradients of dependent variables such as shock waves or the viscous/inviscid interface.

$$
\begin{aligned}
\widetilde{(\cdot)}_{j+\frac{1}{2}} &= \text{minmod}\left[(\cdot)_{j+\frac{1}{2}}, \beta(\cdot)_{j-\frac{1}{2}}\right] \\
\widetilde{\widetilde{(\cdot)}}_{j+\frac{1}{2}} &= \text{minmod}\left[(\cdot)_{j+\frac{1}{2}}, \beta(\cdot)_{j+\frac{3}{2}}\right]
\end{aligned}
\tag{3.7}
$$

were the minmod operator is defined as

$$
\text{minmod}[x, y] = sign(x) \times \max\left[0, \min\left\{|x|, y \times sign(x)\right\}\right]
\tag{3.8}
$$

and β is a compression parameter chosen to be 1.

3.1 Viscous Flux Treatment

Second order central differencing is employed for the spatial discretization of the viscous part of numerical flux through cell interfaces. All discretized viscous elements, except cross-derivative terms, have the form

$$
\phi_{j+\frac{1}{2}}\left(\psi_{j+1} - \psi_j\right)
\tag{3.9}
$$

where $\phi_{j+\frac{1}{2}}$ represents a simple average of ϕ in the neighboring cells. For example, the term $\frac{\mu}{\nu}\frac{\partial u}{\partial \eta}$ will be discretized as

$$
\frac{\mu}{\nu}\frac{\partial u}{\partial \eta} = \frac{1}{2}\left(\frac{\mu_{j+1}}{\nu_{j+1}} + \frac{\mu_j}{\nu_j}\right)\left(u_{j+1} - u_j\right)
$$

The metric quantities are defined at the cell interfaces and do not require averaging. The cross-derivative terms in viscous fluxes have the form

$$
l_\alpha m_\beta \phi_{j+\frac{1}{2}}\left(\frac{\partial \psi}{\partial \xi}\right) \quad \text{or} \quad l_\alpha m_\beta \phi_{j+\frac{1}{2}}\left(\frac{\partial \psi}{\partial \eta}\right)
\tag{3.10}
$$

The discretization of cross-derivative terms is illustrated in (Fig.3.1). For example, in evaluating the flux through $(i+1/2, j, k)$ interface again the l metric does not require averaging and again
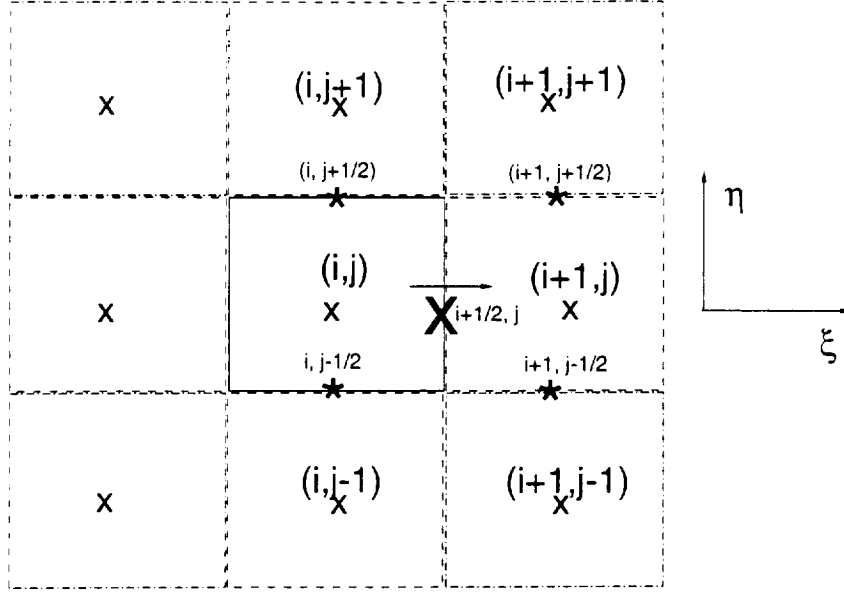
Figure 3.1: Discretization of the cross-derivative viscous terms.

$$u_\xi = u_{i+1,j} - u_{i,j}$$

$$v_\xi = v_{i+1,j} - v_{i,j}$$

$$w_\xi = w_{i+1,j} - w_{i,j}$$

$$T_\xi = t_{i+1,j} - t_{i,j}$$

$$\frac{\mu}{\nu} = \frac{1}{2}\left(\left(\frac{\mu}{\nu}\right)_{i,j} + \left(\frac{\mu}{\nu}\right)_{i+1,j}\right) \qquad (3.11)$$

and

$$u_\eta = \frac{1}{4}\left(u_{i+1,j+1} + u_{i,j+1} - u_{i+1,j-1} - u_{i,j-1}\right)$$

$$m_{x,y,z} = \frac{1}{4}\left(m_{i,j-\frac{1}{2}} + m_{i,j+\frac{1}{2}} + m_{i+1,j-\frac{1}{2}} + m_{i+1,j+\frac{1}{2}}\right) \qquad (3.12)$$

3.2 Source Terms Treatment

The source terms are evaluated at the cell centroids, as well as the dependent variables. The only term which needs to be discretized is the production term, because it contains velocity derivatives.
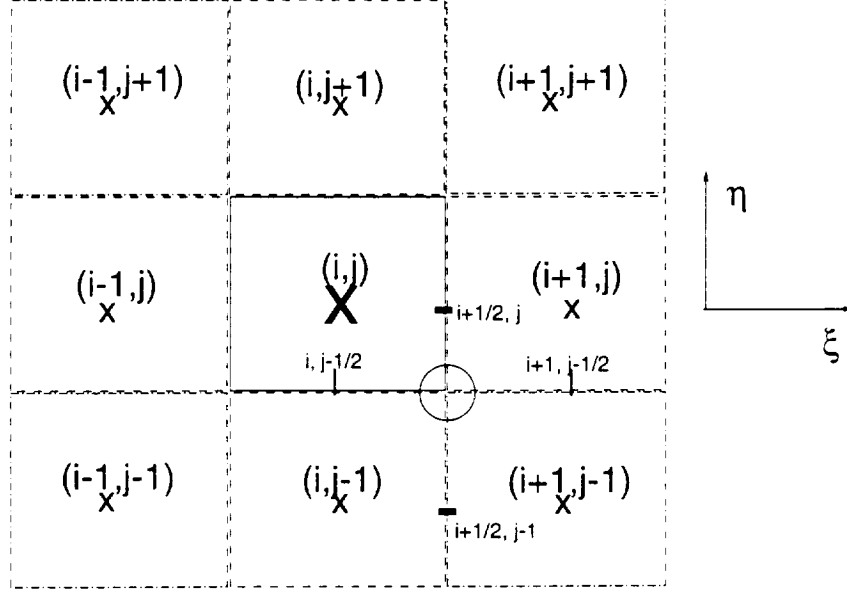
Figure 3.2: Discretization of the production term.

Second order central differencing is employed in order to discretize velocity derivatives in the production term, given by expression (2.53). This expression contains two types of terms. An example of a term of the first type is

$$\left(u_\xi^2 + v_\xi^2 + w_\xi^2\right)\left(l_x^2 + l_y^2 + l_z^2\right)$$

Such terms are approximated at the centroid of the computational cell by second order accurate central differences

$$u_\xi \big|_{i,j} = \frac{1}{2}\left(u_{i+1,j} - u_{i-1,j}\right)$$

$$l_x \big|_{i,j} = \frac{1}{2}\left(l_{x_{i+\frac{1}{2},j}} + l_{x_{i-\frac{1}{2},j}}\right) \tag{3.13}$$

The second group of terms contains terms with velocity derivatives in two directions. In order to achieve higher stability and lower sensitivity to possible mean flow oscillations, such terms are first evaluated at each corner of the 2-D plane computational cell, and then the term in the cell centroid is defined as average over the four corners (Fig. 3.2).

For example, in the corner circled at Fig. 3.2

$$u_\xi = \frac{1}{2}\left[u_{i+1,j} + u_{i+1,j-1} - u_{i,j} - u_{i,j-1}\right]$$

$$v_\xi = \frac{1}{2}\left[v_{i+1,j} + v_{i+1,j-1} - v_{i,j} - v_{i,j-1}\right]$$

$$w_\xi = \frac{1}{2}\left[w_{i+1,j} + w_{i+1,j-1} - w_{i,j} - w_{i,j-1}\right]$$

$$u_\eta = \frac{1}{2}\left[u_{i+1,j} + u_{i,j} - u_{i+1,j-1} - u_{i,j-1}\right]$$

$$v_\eta = \frac{1}{2}\left[v_{i+1,j} + v_{i,j} - v_{i+1,j-1} - v_{i,j-1}\right]$$

$$l_x = \frac{1}{2}\left[l_{x_{i+\frac{1}{2},j}} + l_{x_{i+\frac{1}{2},j-1}}\right]$$

$$l_y = \frac{1}{2}\left[l_{y_{i+\frac{1}{2},j}} + l_{y_{i+\frac{1}{2},j-1}}\right]$$

$$l_z = \frac{1}{2}\left[l_{z_{i+\frac{1}{2},j}} + l_{z_{i+\frac{1}{2},j-1}}\right]$$

$$m_x = \frac{1}{2}\left[m_{x_{i,j-\frac{1}{2}}} + m_{x_{i+1,j-\frac{1}{2}}}\right]$$

$$m_y = \frac{1}{2}\left[m_{y_{i,j-\frac{1}{2}}} + m_{y_{i+1,j-\frac{1}{2}}}\right]$$

$$m_z = \frac{1}{2}\left[m_{z_{i,j-\frac{1}{2}}} + m_{z_{i+1,j-\frac{1}{2}}}\right] \tag{3.14}$$

3.3   Temporal Integration and Linearization

The time-dependent approach has been employed to solve the system of Reynolds-averaged Navier-Stokes equations in body-fitted coordinates. It means, that, despite the fact, that the objective of the present research is to obtain a steady-state solution, the unsteady form of the equations is considered. The steady-state solution is obtained by marching the solution in time until the convergent state is achieved. A simple first order Euler differencing is employed for temporal integration in order to save CPU time and minimize storage requirements.

$$\mathcal{V}_{ijk}\frac{(Q^{n+1}-Q^n)\mid_{ijk}}{\Delta t}+\left(E_{i+\frac{1}{2}}-E_{i-\frac{1}{2}}\right)^{n+1}+\left(F_{j+\frac{1}{2}}-F_{j-\frac{1}{2}}\right)^{n+1}+\left(G_{k+\frac{1}{2}}-G_{k-\frac{1}{2}}\right)^{n+1}$$

$$=\left(R_{i+\frac{1}{2}}-R_{i-\frac{1}{2}}\right)^{n+1}+\left(S_{j+\frac{1}{2}}-S_{j-\frac{1}{2}}\right)^{n+1}+\left(T_{k+\frac{1}{2}}-T_{k-\frac{1}{2}}\right)^{n+1}+\mathcal{V}_{ijk}D_{i,j,k}^{n+1} \quad (3.15)$$

In this vector equation a superscript $n+1$ corresponds to the next time step, and a superscript n corresponds to the previous time step, a subscript $i+\frac{1}{2}$ is a shorthand for $i+\frac{1}{2},j,k$; Q is the vector of independent variables, $\mathcal{V}$ is the physical cell volume, D is the source term vector, vectors E, F and G are inviscid flux vectors and vectors R, S, T are viscous flux vectors in ξ, η and ζ directions respectively.

In order to linearize the inviscid flux, both the second order correction and Roe matrices are evaluated at the previous time step. It yields

$$\left(E_{i+\frac{1}{2}}-E_{i-\frac{1}{2}}\right)^{n+1}=\left(E_{i+\frac{1}{2}}-E_{i-\frac{1}{2}}\right)^n$$
$$+\hat{A}_{i+\frac{1}{2}}^R\Delta Q_{i+1}+\hat{A}_{i+\frac{1}{2}}^L\Delta Q_i-\hat{A}_{i-\frac{1}{2}}^R\Delta Q_i-\hat{A}_{i-\frac{1}{2}}^L\Delta Q_{i-1} \quad (3.16)$$

where

$$\hat{A}_{i+\frac{1}{2}}^R\equiv\frac{1}{2}\left(A_{i+1}^n+(A^--A^+)_{i+\frac{1}{2}}^n\right)$$
$$\hat{A}_{i+\frac{1}{2}}^L\equiv\frac{1}{2}\left(A_i^n-(A^--A^+)_{i+\frac{1}{2}}^n\right)$$

Here A is a Roe's matrix $A=\frac{\partial E}{\partial Q}$, which is evaluated using Roe-averaged variables (see appendix A), and ΔQ is the increment in time of the vector of dependent variables.

Similar linearization holds for the other two inviscid fluxes :

$$\left(F_{j+\frac{1}{2}}-F_{j-\frac{1}{2}}\right)^{n+1}=\left(F_{j+\frac{1}{2}}-F_{j-\frac{1}{2}}\right)^n$$
$$+\hat{B}_{j+\frac{1}{2}}^R\Delta Q_{j+1}+\hat{B}_{j+\frac{1}{2}}^L\Delta Q_j-\hat{B}_{j-\frac{1}{2}}^R\Delta Q_j-\hat{B}_{j-\frac{1}{2}}^L\Delta Q_{j-1}$$

where

$$\hat{B}^R_{j+\frac{1}{2}} \equiv \frac{1}{2}\left(B^n_{j+1} + (B^- - B^+)^n_{j+\frac{1}{2}}\right)$$

$$\hat{B}^L_{j+\frac{1}{2}} \equiv \frac{1}{2}\left(B^n_j - (B^- - B^+)^n_{j+\frac{1}{2}}\right)$$

and B is a Roe's matrix $B = \frac{\partial F}{\partial Q}$.

$$\left(G_{k+\frac{1}{2}} - G_{k-\frac{1}{2}}\right)^{n+1} = \left(G_{k+\frac{1}{2}} - G_{k-\frac{1}{2}}\right)^n$$
$$+\hat{C}^R_{k+\frac{1}{2}}\Delta Q_{k+1} + \hat{C}^L_{k+\frac{1}{2}}\Delta Q_k - \hat{C}^R_{k-\frac{1}{2}}\Delta Q_k - \hat{C}^L_{k-\frac{1}{2}}\Delta Q_{k-1}$$

where

$$\hat{C}^R_{k+\frac{1}{2}} \equiv \frac{1}{2}\left(C^n_{k+1} + (C^- - C^+)^n_{k+\frac{1}{2}}\right)$$

$$\hat{C}^L_{k+\frac{1}{2}} \equiv \frac{1}{2}\left(C^n_k - (C^- - C^+)^n_{k+\frac{1}{2}}\right)$$

and C is a Roe's matrix $C = \frac{\partial G}{\partial Q}$.

The viscous fluxes are linearized by "freezing" the viscosity (laminar and turbulent) and evaluating cross-derivative terms at the previous time step.

$$R^{n+1}_{i+\frac{1}{2}} = R^n_{i+\frac{1}{2}} + \overbrace{\frac{\partial R_{i+\frac{1}{2}}}{\partial Q_{i+1}}}^{L^R_{i+\frac{1}{2}}}\Delta Q^n_{i+1} + \overbrace{\frac{\partial R_{i+\frac{1}{2}}}{\partial Q_i}}^{L^L_{i+\frac{1}{2}}}\Delta Q^n_i$$

$$S^{n+1}_{j+\frac{1}{2}} = S^n_{j+\frac{1}{2}} + \overbrace{\frac{\partial S_{j+\frac{1}{2}}}{\partial Q_{j+1}}}^{M^R_{j+\frac{1}{2}}}\Delta Q^n_{j+1} + \overbrace{\frac{\partial S_{j+\frac{1}{2}}}{\partial Q_j}}^{M^L_{j+\frac{1}{2}}}\Delta Q^n_j$$

$$T^{n+1}_{k+\frac{1}{2}} = T^n_{k+\frac{1}{2}} + \overbrace{\frac{\partial T_{k+\frac{1}{2}}}{\partial Q_{k+1}}}^{N^R_{k+\frac{1}{2}}}\Delta Q^n_{k+1} + \overbrace{\frac{\partial T_{k+\frac{1}{2}}}{\partial Q_k}}^{N^L_{k+\frac{1}{2}}}\Delta Q^n_k \tag{3.17}$$

The source terms are linearized as

$$D^{n+1}_{ijk} = D^n_{ijk} + \overbrace{\frac{\partial D_{i,j,k}}{\partial Q_{i,j,k}}}^{O_{i,j,k}}\Delta Q^n_{i,j,k} \tag{3.18}$$

The numerical scheme can be represented as

$$LHS = RHS \tag{3.19}$$

where LHS and RHS are represented by following expressions:

$$RHS = -\frac{\Delta t}{V} \left\{ \begin{array}{c} \left(E^n_{i+\frac{1}{2}} - E^n_{i-\frac{1}{2}}\right) + \left(F^n_{j+\frac{1}{2}} - F^n_{j-\frac{1}{2}}\right) + \left(G^n_{k+\frac{1}{2}} - G^n_{k-\frac{1}{2}}\right) \\ -\left(R^n_{i+\frac{1}{2}} - R^n_{i-\frac{1}{2}}\right) - \left(S^n_{j+\frac{1}{2}} - S^n_{j-\frac{1}{2}}\right) - \left(T^n_{k+\frac{1}{2}} - T^n_{k-\frac{1}{2}}\right) \\ -\nu D^n \end{array} \right\} \tag{3.20}$$

$$LHS = \left(I - \Delta t O_{i,j,k}\right) \Delta Q_{i,j,k}$$

$$+\frac{\Delta t}{V} \left\{ \begin{array}{c} \left(\hat{A}^R_{i+\frac{1}{2}} - L^R_{i+\frac{1}{2}}\right) \Delta Q_{i+1} \\ +\left[\left(\hat{A}^L_{i+\frac{1}{2}} - L^L_{i+\frac{1}{2}}\right) - \left(\hat{A}^R_{i-\frac{1}{2}} - L^R_{i-\frac{1}{2}}\right)\right] \Delta Q_i \\ -\left(\hat{A}^L_{i-\frac{1}{2}} - L^L_{i-\frac{1}{2}}\right) \Delta Q_{i-1} \end{array} \right\}$$

$$+\frac{\Delta t}{V} \left\{ \begin{array}{c} \left(\hat{B}^R_{j+\frac{1}{2}} - M^R_{j+\frac{1}{2}}\right) \Delta Q_{j+1} \\ +\left[\left(\hat{B}^L_{j+\frac{1}{2}} - M^L_{j+\frac{1}{2}}\right) - \left(\hat{B}^R_{j-\frac{1}{2}} - M^R_{j-\frac{1}{2}}\right)\right] \Delta Q_j \\ -\left(\hat{B}^L_{j-\frac{1}{2}} - M^L_{j-\frac{1}{2}}\right) \Delta Q_{j-1} \end{array} \right\}$$

$$+\frac{\Delta t}{V} \left\{ \begin{array}{c} \left(\hat{C}^R_{k+\frac{1}{2}} - N^R_{k+\frac{1}{2}}\right) \Delta Q_{k+1} \\ +\left[\left(\hat{C}^L_{k+\frac{1}{2}} - N^L_{k+\frac{1}{2}}\right) - \left(\hat{C}^R_{k-\frac{1}{2}} - N^R_{k-\frac{1}{2}}\right)\right] \Delta Q_k \\ -\left(\hat{C}^L_{k-\frac{1}{2}} - N^L_{k-\frac{1}{2}}\right) \Delta Q_{k-1} \end{array} \right\} \tag{3.21}$$

3.4 Approximate Factorization

To avoid the expense of inverting a large sparse matrix, an implicit three-dimensional approximate factorization is employed to break the banded matrix into three block-tridiagonal and one diagonal matrices. The implicit solver is slightly different from standard AF method because the source term Jacobian is split separately, as suggested in [39]. The approximate factorization algorithm can be presented as follows,

$$\left(I - \Delta t O\right) \Delta Q_i^* = RHS \tag{3.22}$$

$$\Delta Q^{\cdot\cdot} + \frac{\Delta t}{\nu}\left(\hat{A}^R_{i+\frac{1}{2}} - L^R_{i+\frac{1}{2}}\right)\Delta Q^{\cdot\cdot}_{i+1} + \frac{\Delta t}{\nu}\left[\left(\hat{A}^L_{i+\frac{1}{2}} - L^L_{i+\frac{1}{2}}\right)\right.$$
$$\left. - \left(\hat{A}^R_{i-\frac{1}{2}} - L^R_{i-\frac{1}{2}}\right)\right]\Delta Q^{\cdot\cdot}_i - \frac{\Delta t}{\nu}\left(\hat{A}^L_{i-\frac{1}{2}} - L^L_{i-\frac{1}{2}}\right)\Delta Q^{\cdot\cdot}_{i-1} = \Delta Q^{\cdot}_i \quad (3.23)$$

$$\Delta Q^{\cdot\cdot\cdot} + \frac{\Delta t}{\nu}\left(\hat{B}^R_{j+\frac{1}{2}} - M^R_{j+\frac{1}{2}}\right)\Delta Q^{\cdot\cdot\cdot}_{j+1} + \frac{\Delta t}{\nu}\left[\left(\hat{B}^L_{j+\frac{1}{2}} - M^L_{j+\frac{1}{2}}\right)\right.$$
$$\left. - \left(\hat{B}^R_{j-\frac{1}{2}} - M^R_{j-\frac{1}{2}}\right)\right]\Delta Q^{\cdot\cdot\cdot}_j - \frac{\Delta t}{\nu}\left(\hat{B}^L_{j-\frac{1}{2}} - M^L_{j-\frac{1}{2}}\right)\Delta Q^{\cdot\cdot\cdot}_{j-1} = \Delta Q^{\cdot\cdot}_j \quad (3.24)$$

$$\Delta Q + \frac{\Delta t}{\nu}\left(\hat{C}^R_{k+\frac{1}{2}} - N^R_{k+\frac{1}{2}}\right)\Delta Q_{k+1} + \frac{\Delta t}{\nu}\left[\left(\hat{C}^L_{k+\frac{1}{2}} - N^L_{k+\frac{1}{2}}\right)\right.$$
$$\left. - \left(\hat{C}^R_{k-\frac{1}{2}} - N^R_{k-\frac{1}{2}}\right)\right]\Delta Q_k - \frac{\Delta t}{\nu}\left(\hat{C}^L_{k-\frac{1}{2}} - N^L_{k-\frac{1}{2}}\right)\Delta Q_{k-1} = \Delta Q^{\cdot\cdot\cdot}_k \quad (3.25)$$

3.5 Boundary Conditions

The following types of boundary conditions are utilized in the present computation: "no-slip" solid wall, "slip" solid wall, or Euler reflection boundary, supersonic inflow boundary, supersonic outflow boundary.

3.5.1 "No-Slip" Solid Wall

The physical viscous "no-slip" boundary conditions at the solid wall is

$$u\,|_W = 0$$
$$v\,|_W = 0$$
$$w\,|_W = 0$$
$$k\,|_W = 0$$
$$q\,|_W = 0 \quad \text{or} \quad T\,|_W \text{ is fixed} \quad (3.26)$$

There is no physical boundary condition for the solenoidal dissipation. The one

derived by considering the equation of turbulence kinetic energy transport in the viscous sublayer, which is the common choice for the turbulence models involving "real" dissipation, is:

$$\epsilon\,|_W = \frac{2\mu_w}{\rho_w} \left(\frac{\partial \sqrt{k}}{\partial y} \right)^2 |_W \qquad . \qquad (3.27)$$

Several other boundary conditions, like zero gradient of dissipation, proposed by Lam and Bremhorst [32] etc. were also tested but all of them turned to be unstable in present computations. The numerical implementation of this boundary conditions have extremely strong influence on the stability of the computation. As suggested in [59], on the solid wall the solution point is put on the surface of the wall instead of the center of the cell, like it is done with internal points. The wall boundary conditions are treated explicitly. When the wall is adiabatic and the first derivative of temperature at the wall has to be zero, it is essential to evaluate it with the second order of accuracy to avoid too big truncation error.

3.5.2   Solid "Slip" Wall Boundary Condition

In order to reduce the number of grid points it was suggested in [24] to treat the side walls in the crossing shock interaction computation as adiabatic slip boundaries and no boundary layers are formed near the side walls. This approach is reasonable when the shocks are reflected from the side walls downstream of the domain of interest. This approach was employed for $7° \times 11°$ and $7° \times 7°$ geometric configurations.

The inviscid flux through the wall is evaluated exactly as

$$F_{\text{inviscid}} = (0, pn_x, pn_y, pn_z, 0, 0, 0)^{\mathrm{T}}$$

It was shown in [60], that computing the inviscid flux through the solid wall utilizing the Roe scheme and fictitious cells can cause additional not physical flux of momentum across the boundary. The fictitious cells are utilized to compute viscous flux through the slip boundary and to evaluate the second order derivative of velocity with respect to ζ to be employed in the production of turbulence kinetic energy. Variables in the

fictitious cells are determined in the following way:

$$\rho_f = \rho_p \tag{3.28}$$

$$p_f = p_p \tag{3.29}$$

$$k_f = k_p \tag{3.30}$$

$$\epsilon_f = \epsilon_p \tag{3.31}$$

$$\tag{3.32}$$

Here subscript f denotes a fictitious cell and subscript p denotes a physical cell adjacent to the wall. The velocity components in the fictitious cell are updated in such a way that the component of the velocity normal to the wall be zero at the wall. The tangential to the wall component of the velocity in the fictitious cell is equal to the corresponding component in the physical cell.

3.5.3 Supersonic Inflow

At the inflow boundary the fictitious cells are utilized. The profiles of all dependent variables in the fictitious cells are determined by the solution of the compressible turbulent flat plate boundary layer using the 2-D boundary layer code, developed by R. Becht [5], and are not updated during the computation.

3.5.4 Supersonic Outflow

The simple zero gradient boundary conditions are employed at the supersonic outflow.

Chapter 4

2-D BOUNDARY LAYER TEST COMPUTATIONS

A 2-D test computation was performed to establish the accuracy of the solver and the ability of the grid used in 3-D simulation to allow to resolve accurately at least the uncoming flat plate turbulent boundary layer [24]. The solver was validated through the application to the following computations:

a Laminar flat plate boundary layer

b Turbulent flat plate adiabatic boundary layer

c Turbulent flat plate isothermal boundary layer

In the present chapter, nondimensional variables are plotted in all figures, unless otherwise stated. The nondimensionalization is described in section (2.3), in Table (2.3).

4.1 Laminar Compressible Flat Plate Boundary Layer

In order to validate the accuracy of the laminar part of the solver, the compressible supersonic laminar 2-D flat plate boundary layer was computed and the solution was compared to the exact self-similar Blasius solution [53].

The Blasius equation is

$$\frac{df}{d\eta} = f' = \frac{u^*}{U_\infty}$$
$$f''' + ff'' = 0 \tag{4.1}$$

with the boundary conditions

$$f(0) = 0$$

$$f'(0) = 0$$

$$f'(\infty) = 1$$

The self-similar variable η is the transformed distance in vertical direction:

$$\eta = \sqrt{\frac{\mathrm{Re}}{2}} \int_0^y \frac{\rho}{\rho_\infty} \frac{dy}{x} \qquad (4.2)$$

The 2-D compressible boundary layer equations can be reduced to the Blasius equation provided that the molecular viscosity is a linear function of temperature, $Pr = 1$ and the flat plate is adiabatic. In order to compare computational and analytical results, these three conditions were incorporated into the Navier-Stokes solver.

The 2-D flat plate boundary layer was simulated with Re, based on the plate length, of 10^4 and $M_\infty = 2$.
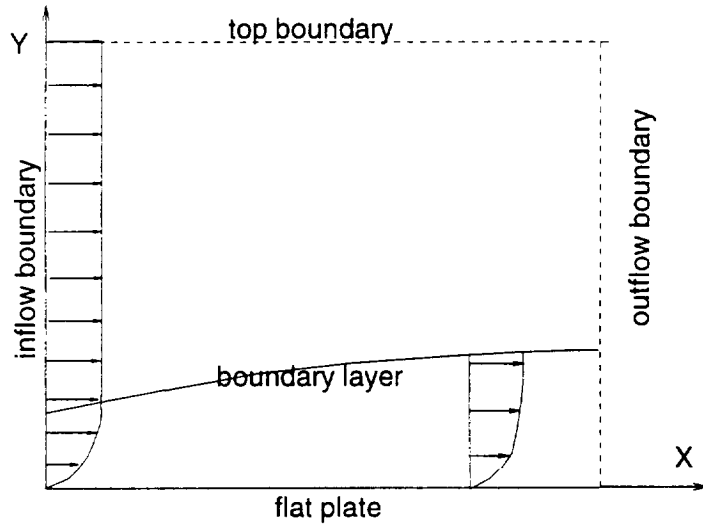
Figure 4.1: Schematic of the computational domain for boundary layer over a flat plate.

The computational configuration is shown in Fig. (4.1). The inflow boundary condition, imposed at $x = 1.$, is a developed laminar Blasius boundary layer profile [53], reinterpolated onto the present grid. Separate computations were performed in two different planes and with the grid rotated at a certain angle in each of the planes.

Nondimensional pressure contours computed in rotated coordinates are presented in Fig. (4.2). The profiles of nondimensional velocity and temperature at several x
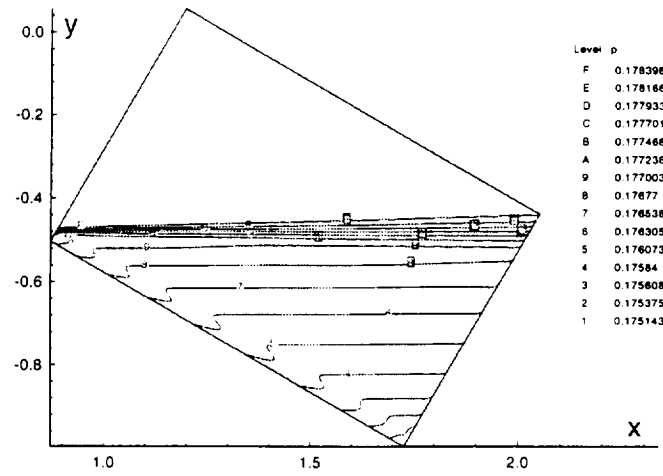
Figure 4.2: Pressure contours for the laminar boundary layer.
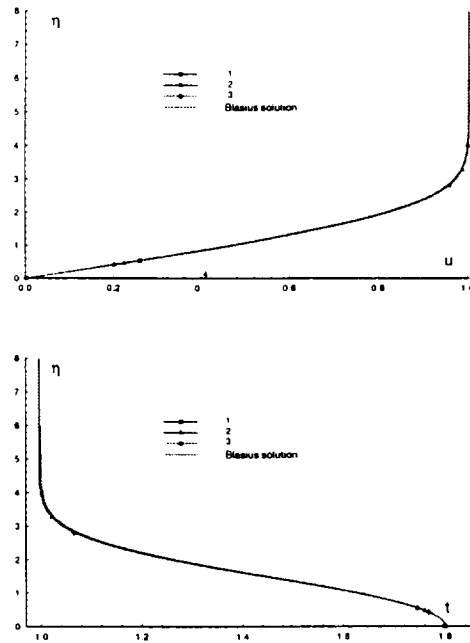
Figure 4.3: Velocity and temperature profiles in the laminar flat plate boundary layer:
1 $Re_x = 0.125 \times 10^4$ 2 $Re_x = 0.5 \times 10^4$ 3 $Re_x = 0.875 \times 10^4$.

locations, plotted *vs* self-similar coordinate, are compared to the exact solution in Fig. (4.3). The agreement is excellent.

4.2 Turbulent Flat Plate Boundary Layer

In order to validate that the 3-D code is correctly solving the governing equations, computational results were compared to the results obtained with the turbulent boundary layer code, developed independently by R. Becht [5], which utilizes the same low Reynolds number correction. Since the boundary layer code uses much more refined grid, than the 3-D code (typically 600 grid points across the boundary layer), the boundary layer code predictions can be considered as being more accurate. The freestream parameters are taken exactly the same as in the 3-D computation, i.e. the Mach number is 3.95 and the Reynolds number based on the inflow boundary layer thickness, is equal to 3×10^5. The computational configuration is the same as shown in Fig. (4.1) for the laminar computation. The inflow is a turbulent boundary layer profile, the same one as in the 3-D computation. The profiles of dependent variables *vs* y coordinate shown at the figures below are taken 10.5 cm downstream, which constitutes 30 characteristic distancies, and the whole computational domain is 12.25 cm (35 characteristic distances) long in streamwise direction. The characteristic distance is chosen equal to the experimental boundary layer thickness at the upstream location.

The grid has $N_x = 72$ nodes in streamwise direction and $N_y = 81$ nodes in vertical direction. The number of grid points within the boundary layer is 52 at the end of the flat plate. The grid is uniform in streamwise direction. The y_1^+ location of the second cell centroid is 0.3. The first 18 cells adjacent to the wall are uniform, then geometrical stretching with stretching coefficient of 1.2 is employed until a computational cell becomes a square.

The grid, employed in the boundary layer computation, consists of 700 nodes, 600 of which are located in the boundary layer. The boundary layer code results were reinterpolated to the sparse grid, used by the 3-D code.

At the supersonic inflow boundary all dependent variables are set according to the

data, obtained with the boundary layer code. The "no-slip" boundary condition is implemented at the flat plate, and zero gradient boundary conditions are imposed at two other boundaries.

4.2.1 Adiabatic Wall Test Case

The results of the test computations over the adiabatic (zero heat flux) flat plate are presented below. The boundary condition on temperature is simply that the temperature derivative at the wall is zero. It is essential to utilize a second order expression for the derivative in order to minimize a truncation error and accurately predict the adiabatic temperature.

The computed streamwise velocity, vertical velocity, static temperature, turbulent kinetic energy and dissipation of turbulence kinetic energy profiles are compared to the boundary layer code results in figures (4.4 - 4.6) at some X location close to the trailing edge of the flat plate. The abscissa is the dimensionless y coordinate. The results obtained with the 3-D Navier-Stokes solver using a grid of 81 nodes in vertical direction, are in excellent agreement with those computed with the boundary layer code.

The distribution of the skin friction coefficient along the flat plate is compared to the boundary layer code results in Fig. (4.7 a). The deviation at any x location does not exceed 0.6%. The adiabatic wall temperature, presented in Fig.(4.7 b), is in excellent agreement with the boundary layer code predictions and the deviation between two results does not exceed 0.04%.

4.2.2 Isothermal Wall Test Case

The isothermal wall temperature is kept constant at 265 K (the inflow static temperature is 63.2 K). All other boundary conditions are the same as in the test case above.

The L-2 norm residual (Fig. 4.8) computed as the square root of the squares of the right hand sides of the seven governing equations is down 11 orders during the computation and reaches the machine zero when the solution is converged. As in the adiabatic wall case, velocity, temperature, turbulence kinetic energy and dissipation
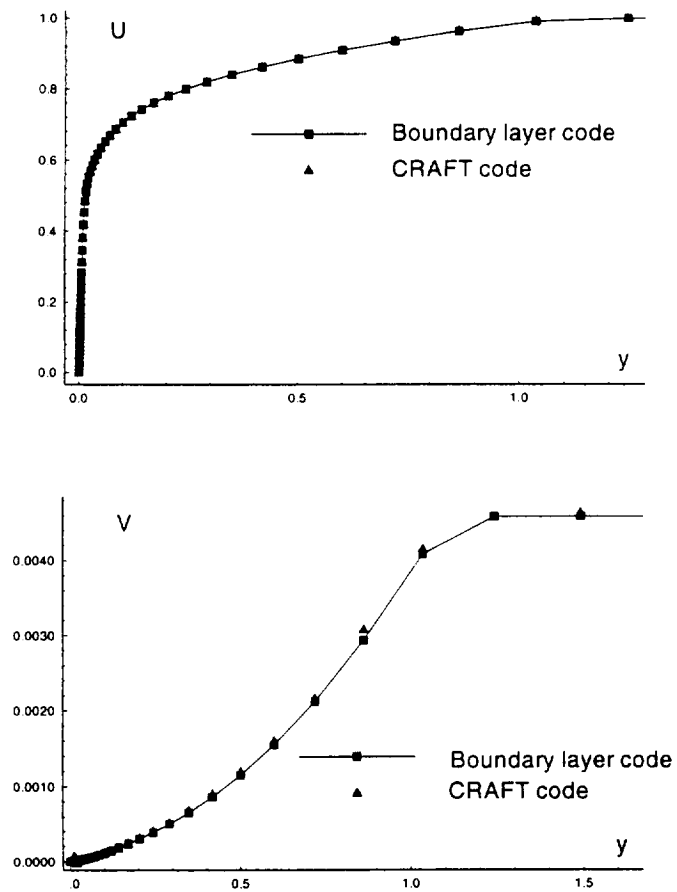
Figure 4.4: Streamwise and vertical velocity profile in the boundary layer over an adiabatic flat plate.
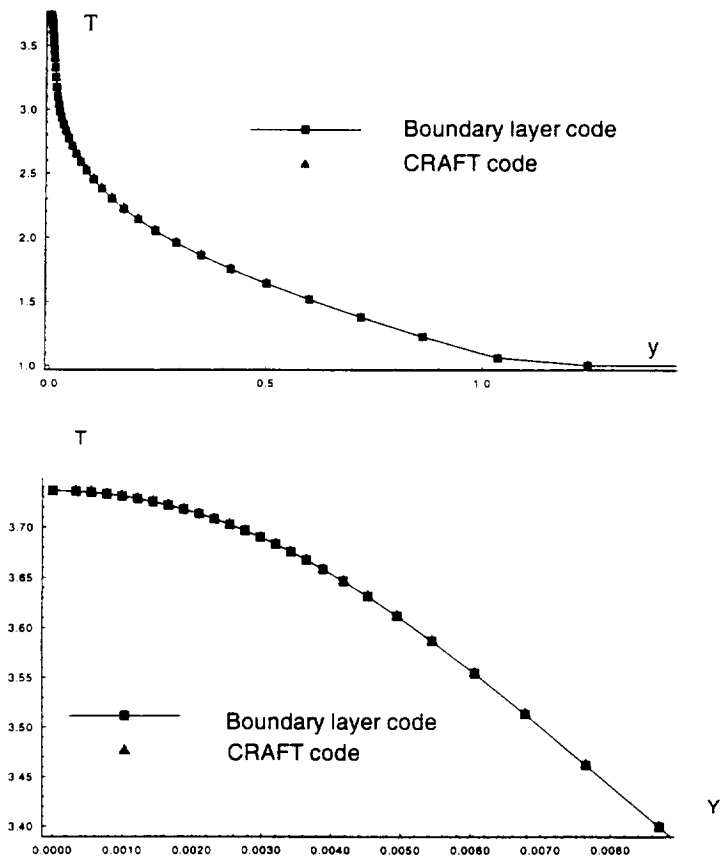
Figure 4.5: Temperature profile in the boundary layer over an adiabatic flat plate.
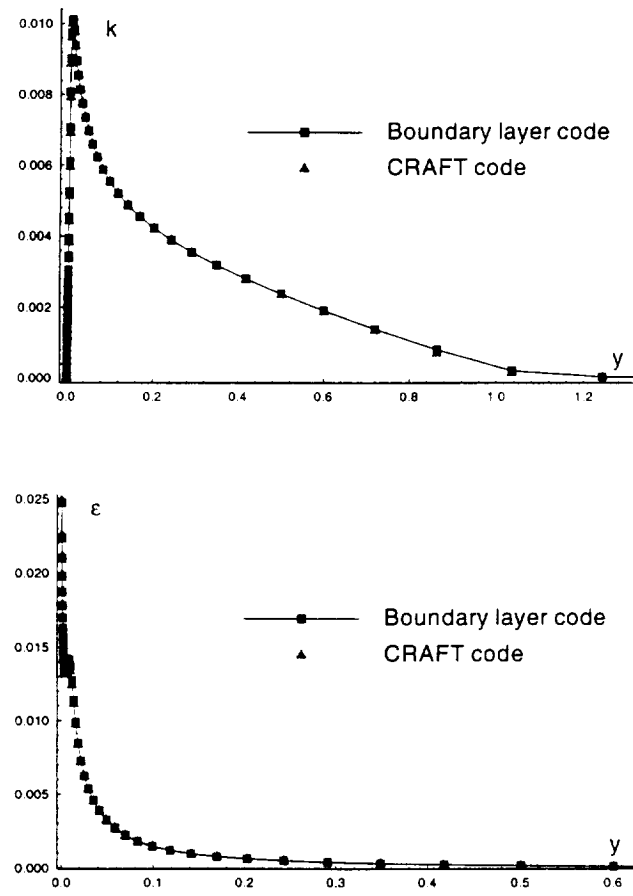
Figure 4.6: Turbulence quantities profiles in the boundary layer over an adiabatic flat plate.
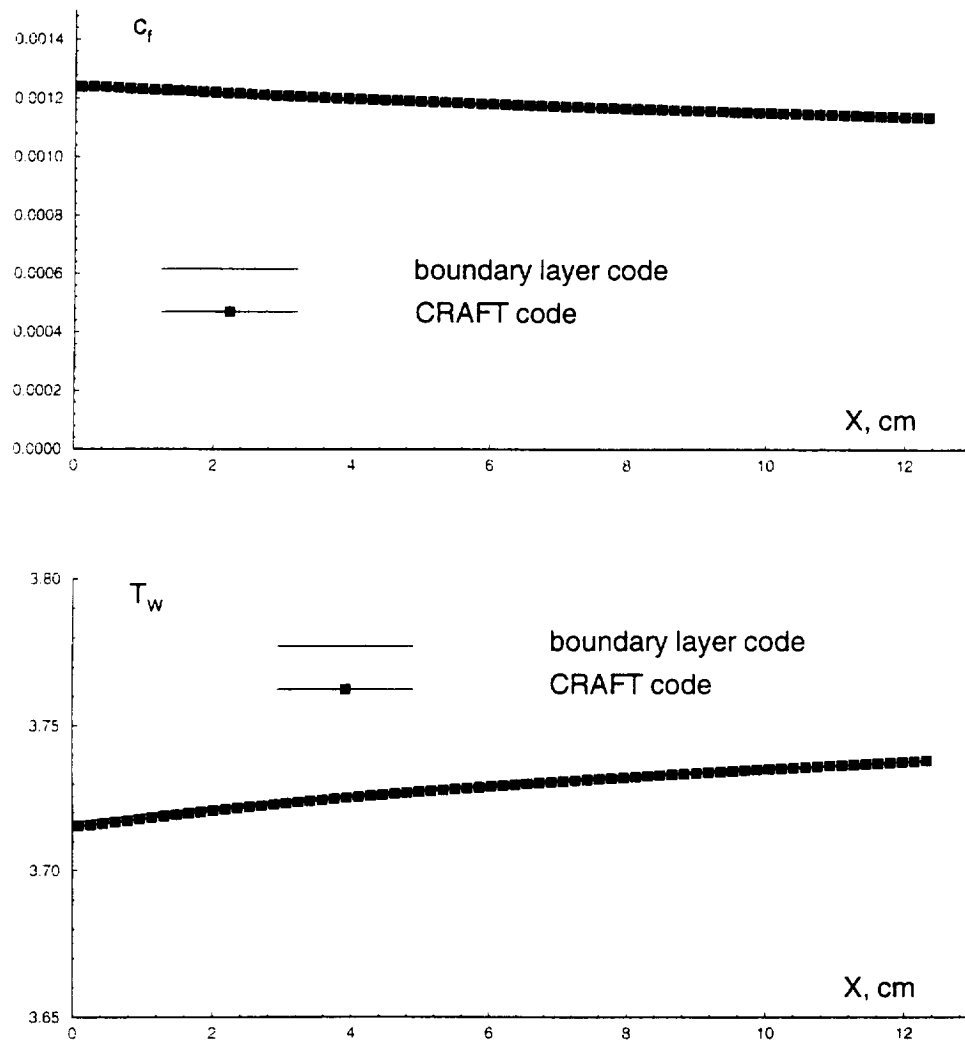
Figure 4.7: Skin friction and adiabatic wall temperature *vs* x.
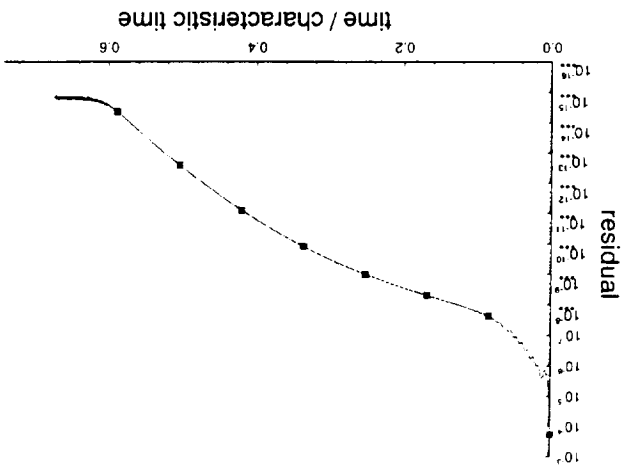
Figure 4.8: L-2 norm residual.

profiles agree well with the boundary layer code results. The skin friction, wall heat flux

$$q_w = -\frac{1}{(\gamma-1)M_\infty^2 Re_\delta}\frac{\mu}{Pr}\frac{\partial(T/T_\infty)}{\partial(y/\delta)}$$

and the heat transfer coefficient Figs. 4.9-4.11 are also in excellent agreement with the corresponding boundary layer code results. The deviation for c_h is approximately 0.6%.
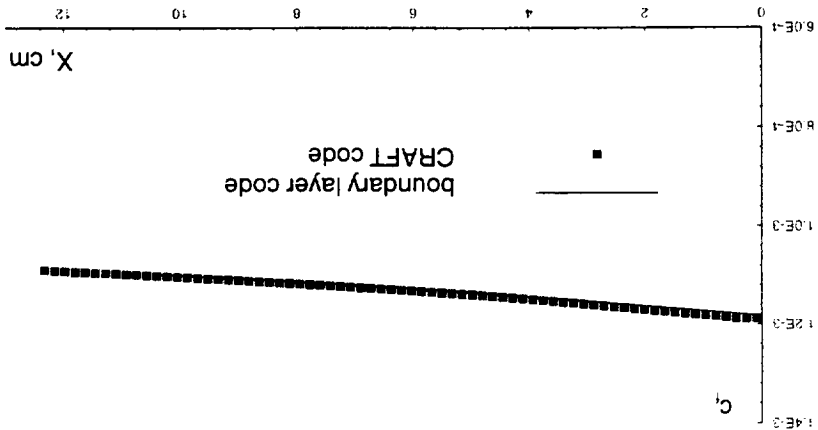
Figure 4.9: Skin friction.
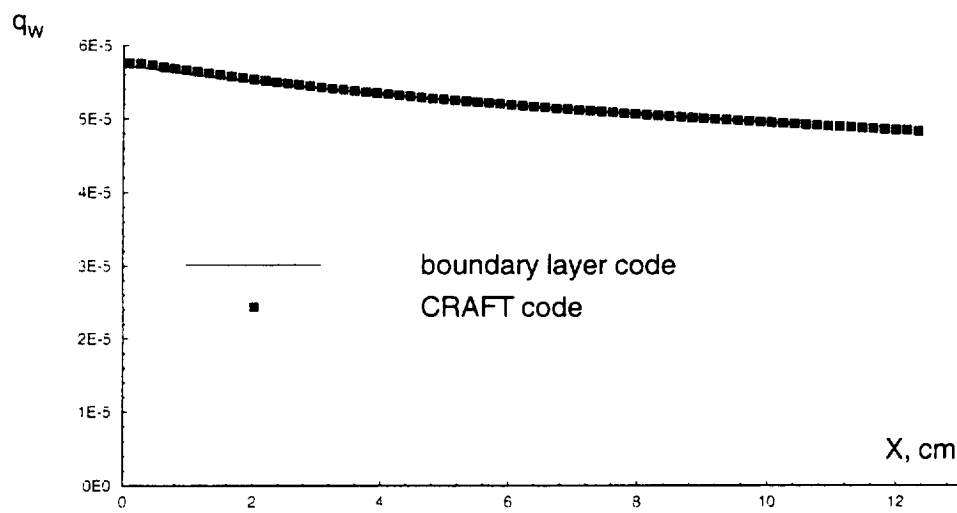
Figure 4.10: Wall heat flux *vs x*
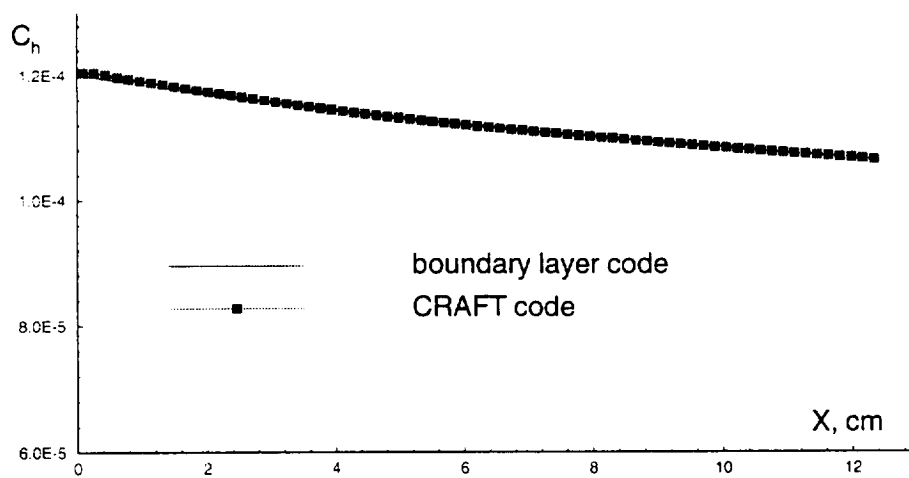
Figure 4.11: Heat transfer coefficient *vs* x.

Chapter 5

PROBLEM DEFINITION

The focus of the present study is to validate the low Reynolds number correction of Knight to the standard $k-\epsilon$ model in numerical simulation of the flow involving the crossing shock wave/boundary layer interaction. The double fin configuration utilized in the experiments of Zheltovodov et al. [62] is chosen for this purpose since both extensive experimental and previous computational results are available for comparison. Experimental data available for comparison includes surface pressure, heat transfer, adiabatic wall temperature and surface flow visualization. Computational results are extensively compared to the experimental results for all cases. Comparison to the previous computational results of Knight et al. [24] using the Chein's model and of Zha and Knight [61] using the full Reynolds stress equation model is also reported for the heat transfer rate and adiabatic wall temperature.

The shock waves are generated by a pair of fins which are mounted normal to a flat plate and form a converging channel. Three configurations with fin angles of $7° \times 11°$, $7° \times 7°$ and $15° \times 15°$ have been examined at Mach 3.9. The experimental configuration is presented in Fig. 5.1. The incoming flow parameters are summarized in Table 5.1.

The inflow profiles were generated with the boundary layer code [6], which utilizes the same turbulence model. The appropriate inflow profile is considered to be the one created by the boundary layer code which matches the experimental value of displacement thickness. As suggested in [24], [61], thin boundary layers on side walls of the double fin channel can be neglected for the $7° \times 11°$ and $7° \times 7°$ cases, since their influence is limited to regions close to the side walls, where no experimental data is available anyway. Consequently, the side walls are treated as slip boundaries in the

Table 5.1: Computational Conditions

Ref.	M_∞	α_1	α_2	Re_{δ_∞}	p_{t_∞} MPa	T_{t_∞} $^\circ K$ mm	δ_∞^*
EXPERIMENT							
Zheltovodov *et al* [62]	3.95	7°	11°	3.0×10^5	1.5	260	1.1
Zheltovodov *et al* [62]	3.95	7°	7°	3.1×10^5	1.5	261	1.1
Zheltovodov *et al* [62]	3.95	15°	15°	3.0×10^5	1.5	262	1.1
COMPUTATION							
Case 1	3.95	7°	11°	3.0×10^5	1.5	260	1.1
Case 2	3.95	7°	7°	3.1×10^5	1.5	261	1.1
Case 3	3.95	15°	15°	3.0×10^5	1.5	262	1.1

LEGEND

M_∞	freestream Mach number	T_{t_∞}	freestream total temperature
Re_{δ_∞}	Reynolds number based on δ_∞	δ_∞^*	upstream displacement thickness
p_{t_∞}	freestream total pressure	α_1, α_2	fin angles (deg)
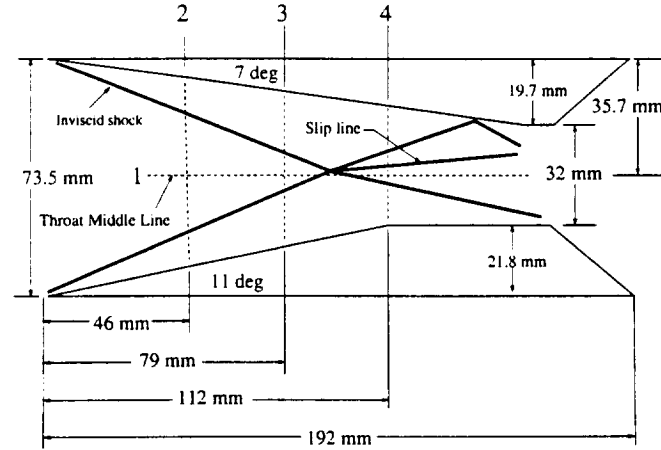
Figure 5.1: 7° × 11° (Zheltovodov *et al.*)

$7° \times 11°$ and $7° \times 7°$ computations, which saves memory and computational time. Of course, after the shocks are reflected from the side walls and come to the central part of the computational domain, computational results will deviate significantly from experiment. However, nearly all of the experimental data for the $7° \times 7°$ and $7° \times 11°$ configurations was obtained upstream of this point. The legitimacy of this approach will be examined. This is not applicable to the $15° \times 15°$ case, since in this case the shock is reflected from the sidewall almost in the middle of the computational domain in streamwise direction, and the shock wave-sidewall turbulent boundary layer interaction should be treated adequately.

Three configurations were considered, with different fin angles: $7° \times 11°$, $7° \times 7°$ and $15° \times 15°$. For each case two separate computations were performed in order to determine the heat transfer coefficient

$$C_h = q_w(x, z) / \{\rho_\infty U_\infty c_p[T_w(x, z) - T_{aw}(x, z)]\} \tag{5.1}$$

where $q_w(x, z) = -\kappa_w \partial T / \partial y$ is the wall heat transfer. First, the wall temperature was fixed at $T_w = 1.031 T_{t_\infty}$, and the local heat transfer $q_w(x, z)$ determined. Then, the wall was assumed adiabatic and the local adiabatic wall temperature $T_{aw}(x, z)$ was determined. This approach has been employed previously for comparison with experimental heat transfer [24], [34], [61].

In addition, a separate computation was performed for the first case in order to investigate the influence of the wall temperature. Details of the computations are presented in Table 5.2. The results of the computations are described in the next chapter.

Table 5.2: Details of Computations

Ref	α_1	α_2	BC	T_w	N_x	N_y	N_z
Case 1a	7°	11°	S	I	101	81	49
Case 1b	7°	11°	S	A	101	81	49
Case 1c	7°	11°	S	I	202	81	49
Case 1d	7°	11°	S	I	101	162	49
Case 1e	7°	11°	S	I	101	81	98
Case 1f	7°	11°	S	I, $T = 270k$	101	81	49
Case 2a	7°	7°	S	I	101	79	49
Case 2b	7°	7°	S	A	101	79	49
Case 3a	15°	15°	N	I	101	79	65
Case 3b	15°	15°	N	A	101	79	65

Ref	$\Delta x/\delta_\infty$	$\Delta y_{min}/\delta_\infty$	$\Delta y_{max}/\delta_\infty$	$\Delta z_{min}/\delta_\infty$	$\Delta z_{max}/\delta_\infty$	$\Delta y_2^+\big|_{rms}$	$\Delta y_2^+\big|_{aver}$
Case 1a	0.5	2.2×10^{-4}	0.5	0.2	0.5	0.70	0.62
Case 1b	0.5	2.2×10^{-4}	0.5	0.2	0.5	0.80	0.72
Case 1c	0.25	2.2×10^{-4}	0.5	0.2	0.5	0.72	0.65
Case 1d	0.5	1.1×10^{-4}	0.25	0.2	0.5	0.35	0.31
Case 1e	0.5	2.2×10^{-4}	0.5	0.1	0.25	0.70	0.63
Case 1f	0.5	2.2×10^{-4}	0.5	0.2	0.5	0.68	0.60
Case 2a	0.5	2.2×10^{-4}	0.5	0.2	0.5	0.55	0.52
Case 2b	0.5	2.2×10^{-4}	0.5	0.2	0.5	0.63	0.59
Case 3a	0.5	2.2×10^{-4}	0.5	1.6×10^{-4}	0.5	1.04	0.87
Case 3b	0.5	2.2×10^{-4}	0.5	1.6×10^{-4}	0.5	1.16	0.97

LEGEND

N_x	number of points in x	I	Isothermal wall
N_y	number of points in y	A	Adiabatic wall
N_z	number of points in z	N	"No-slip" side walls
$\Delta y_2^+\big|_{rms}$	rms grid spacing at wall in wall units	S	"Slip" side walls

Chapter 6

RESULTS

6.1 Crossing Shock $7° \times 11°$

The inviscid shock structure is presented in Fig. 6.1. Two inviscid shocks originate at the sharp fin tips, intersect at approximately $x = 90$mm and are reflected from the wedge side walls at approximately $x = 140$mm (from $7°$ fin) and $x = 157$mm (from $11°$ fin). The oblique shock angles are well predicted by inviscid theory. There is also a rarefaction fan formed by the flow expanding downstream of the corner at $11°$ fin. The wave structure close to the bottom flat plate can be very complex and substantially different from the inviscid wave structure due to the nature of the shock wave-turbulent boundary layer interaction, as will be described later.

General description of the "crossing shock interaction" flow can be found in [3, 15, 40, 42, 43]. The description of the present flow, based on both experimental and computational results, is available in [24] and [61]. The incoming flow separates across the entire spanwise direction and becomes involved in the uplifting motion. The computational domain and 3-D streamlines are presented in Fig. 6.2. The streamlines, which originated at the flat plate at inflow boundary, converge downstream the interaction. The flow is dominated by a pair of counter-rotating cross-flow vortices. They merge and form a counter-rotating vortex pair which moves towards the left fin and forms a low total pressure jet, as shown in Fig. 6.3. The vortex pair entrains the low energy fluid in the incoming boundary layer into a concentrated region. The picture is essentially three-dimensional and asymmetric due to the different fin angles and different shock strength.

Figs. 6.4, 6.5 and 6.6 present the computed surface skin friction lines and experimental surface flow visualization respectively. The streamlines in Fig. 6.4 are colored
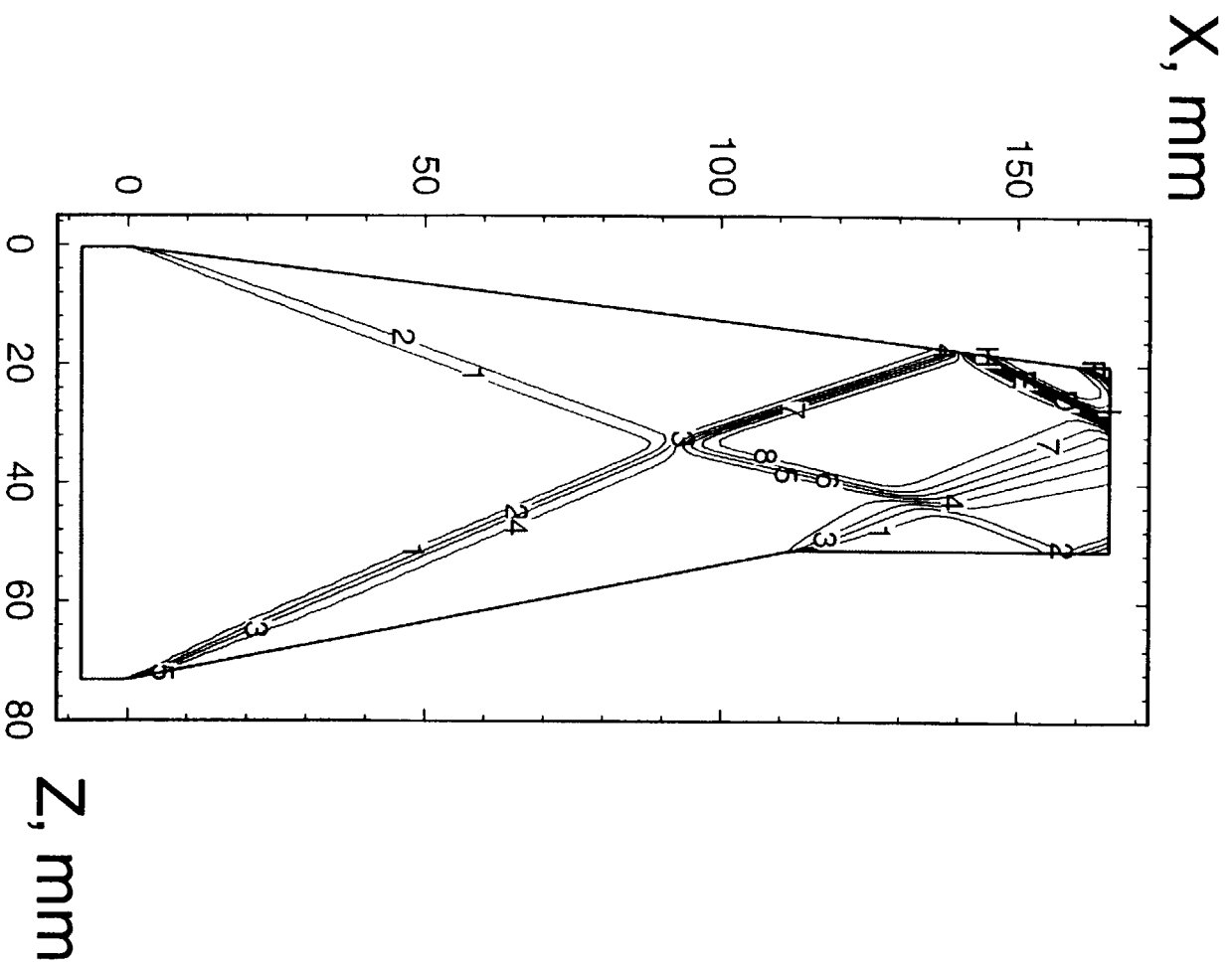
Figure 6.1: Inviscid shock structure for $7° \times 11°$.
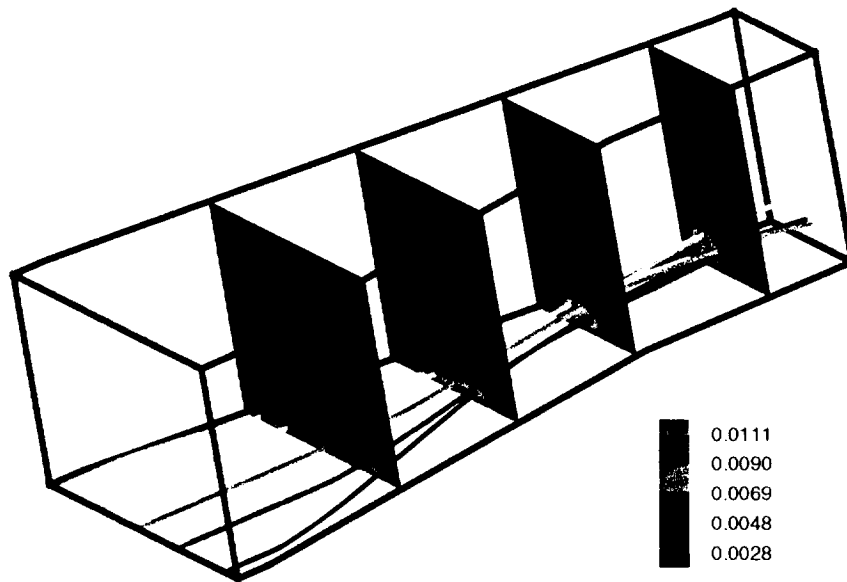
Figure 6.2: Turbulence kinetic energy contours and 3-D streamlines for $7° \times 11°$.
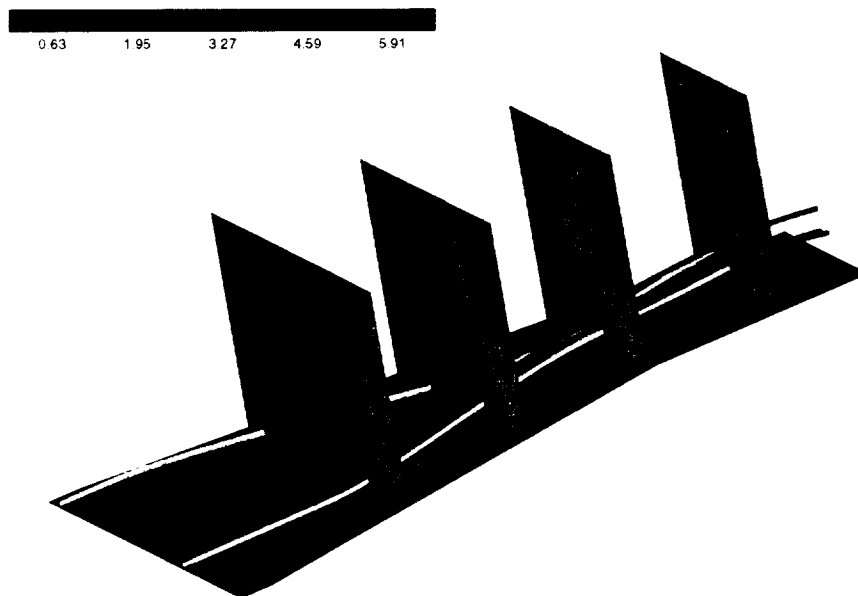
Figure 6.3: Total pressure contours and 3-D streamlines for $7° \times 11°$.

according to the values of static pressure. The Fig. 6.5 is taken from [24]. It has been noted before [24] [41] that the computed surface skin friction lines are sensitive to the turbulence model employed. Comparison of current results with [24] shows general agreement as well as a number of substantially different details. Both incident separation lines (lines of coalescence [48]) emanating from the fin leading edges (1 and 2) are clearly observed in Fig. 6.4 in agreement with experimental results and previous simulations of Knight *et al* [24] using the $k - \epsilon$ model with the Chien low Reynolds number correction. These separation lines are associated with the incident single fin interactions. The computed and experimental separation line angles, measured relative to the x-axis, agree within 9%. However, contrary to the computation [24] with the Chien's model [9] (see Fig.6.5), the incident separation lines do not coalesce near the center of the region but rather continue downstream almost in parallel until they converge at $x \approx 110$ mm to form a narrow band of skin friction lines (3), which is offset to the left side of the channel. It is denoted in [24] as the left downstream coalescence line. This line represents the surface image of the boundary between the left and right vortices generated by the incident single fin interactions. The vortices are evident in the crossflow velocity vectors (Fig. 6.7) at $x = 112$ mm. The crossflow velocity vectors near the surface change direction at 3. Lines of divergence are also apparent near the right fin (4) and left fin (5) associated with the incident single fin interaction. In a major difference with the Chien's model results, a second line of coalescence (the right downstream coalescence line in Fig. 6.5) is not present in this computation. Consequently, the model does not predict a secondary separation underneath the left side of the right vortex (see [24]). The difference is due to deviation in the predictions of the pressure distribution in the spanwise direction, obtained with each turbulence model, as described below.

The computed and experimental surface pressure distribution in the spanwise direction at $x = 112$ mm, normalized by the freestream static pressure p_∞, is displayed in Fig. 6.8. This location corresponds to the streamwise location No. 4 (see previous chapter). The plot contains computational results obtained with three different turbulence models as described above. The abscissa $z - z_{\text{TML}}$ represents the spanwise distance
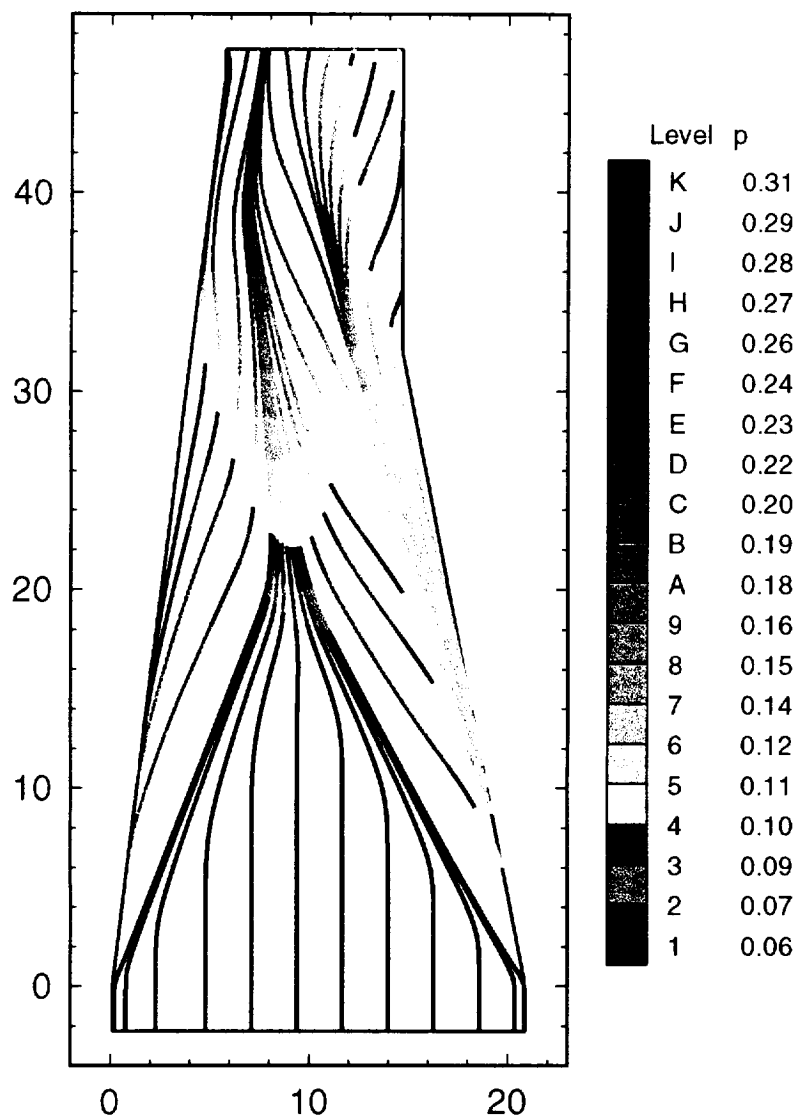
Figure 6.4: Computed skin friction lines for $7° \times 11°$ for $k - \epsilon$ model with low Re number correction of Knight :

1 Left incident separation line

2 Right incident separation line

3 Left downstream coalescence line

4,5 Lines of divergence
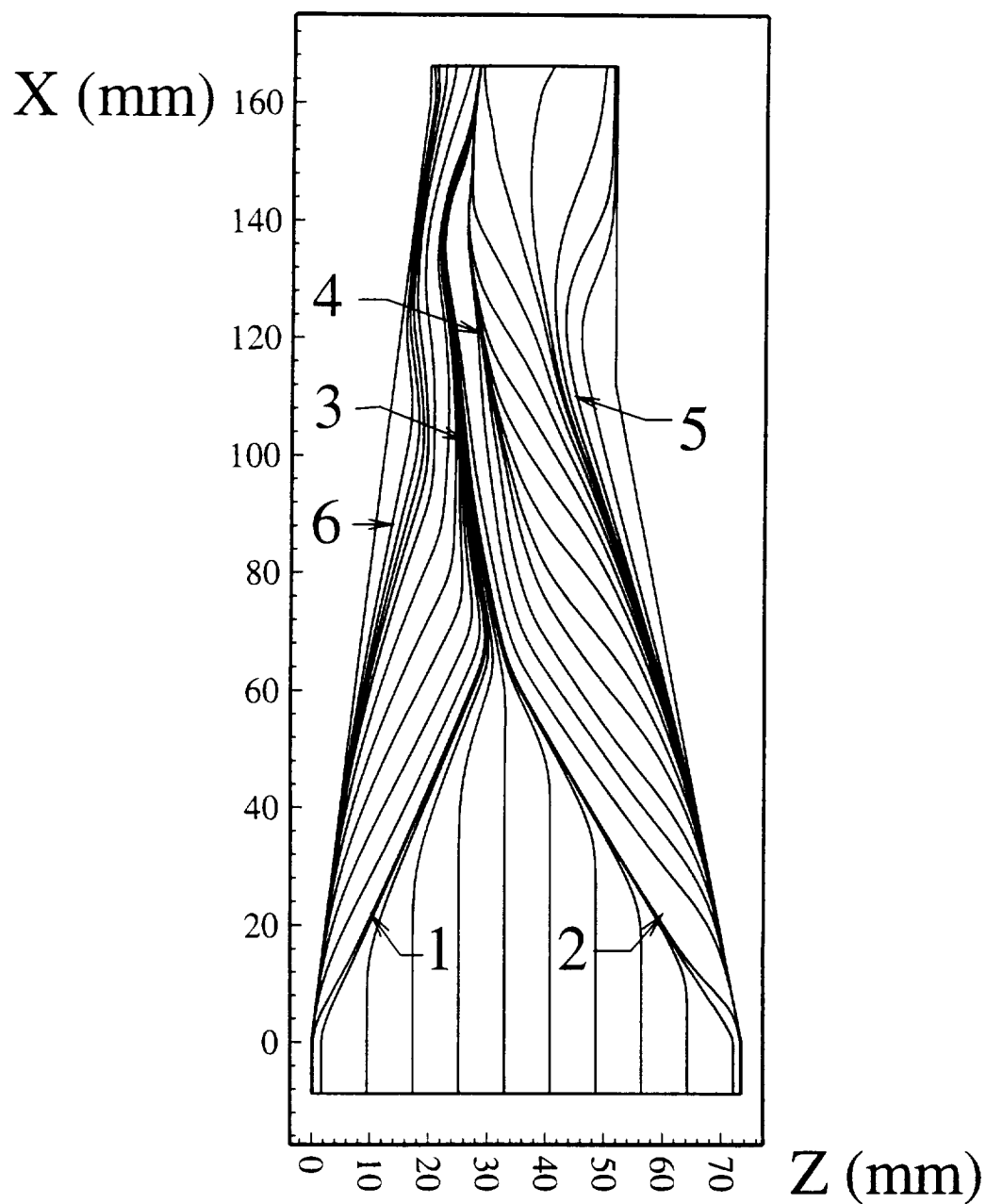
Figure 6.5: Computed skin friction lines for $7° \times 11°$ for $k - \epsilon$ model with low Re number correction of Chien :

1 Left incident separation line
2 Right incident separation line
3 Left downstream coalescence line
4 Right downstream coalescence line
5,6 Lines of divergence

Figure 6.6: Experimental surface flow for $7° \times 11°$

measured from the TML (Throat Middle Line, Fig.5.1). The computed and experimental surface pressure are in general agreement for all three models. However unlike in the present computations, the Chien's model predicts a local adverse pressure gradient in spanwise direction in the region $-7\,\text{mm} < z - z_{\text{TML}} < 0\,\text{mm}$. As described in detail in [24], the flow near the surface at this location is moving towards the left fin and the adverse pressure gradient causes the secondary separation and the appearance of the right downstream coalescence line, which is not predicted by the present computation.
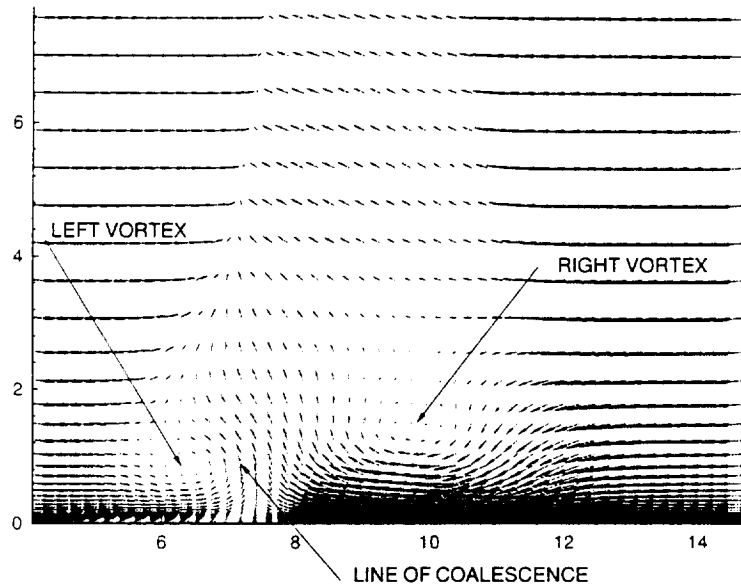
Figure 6.7: Crossflow velocity vectors at $x = 112$ mm for $7° \times 11°$

The computed and experimental surface pressure along the Throat Middle Line and at streamwise locations $x = 46$mm and $x = 79$mm is displayed in Figs. 6.9, 6.10 and 6.11, respectively. The computed and experimental surface pressure on TML are in good agreement for $x < 135$ mm, although the computation underestimates the extent of the upstream influence, as observed in previous studies (e.g., [24], [42]). The computed pressure does not accurately predict the pressure rise (beginning at $x = 145$ mm) associated with the shock reflection from the $7°$ fin, since the computation omits the boundary layers on the fin surfaces. The uncertainty in experimental surface pressure measurements does not exceed $\pm 0.5\%$.
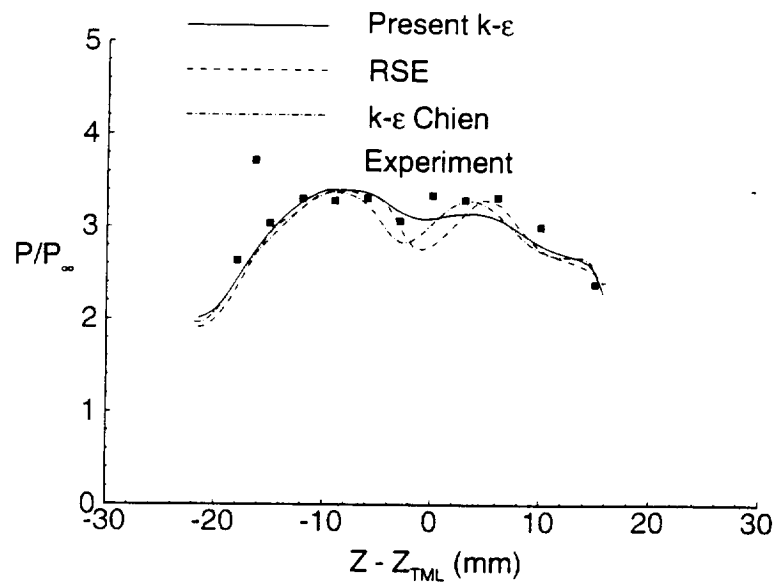
Figure 6.8: Wall pressure at $x = 112$ mm for $7° \times 11°$
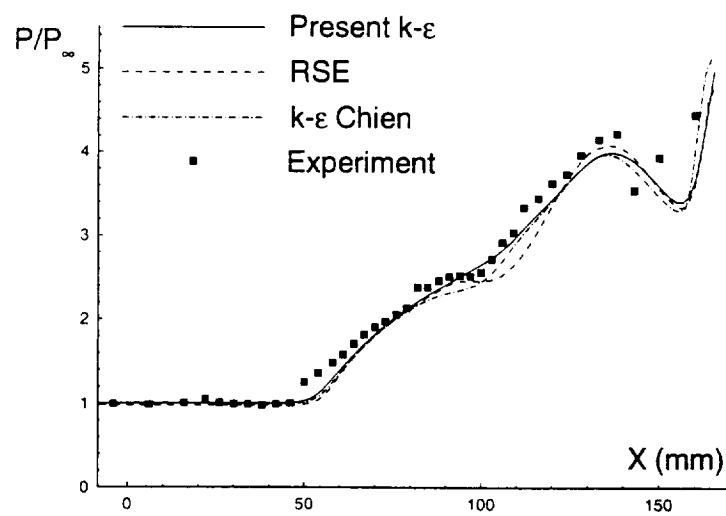
Figure 6.9: Wall pressure on TML for $7° \times 11°$
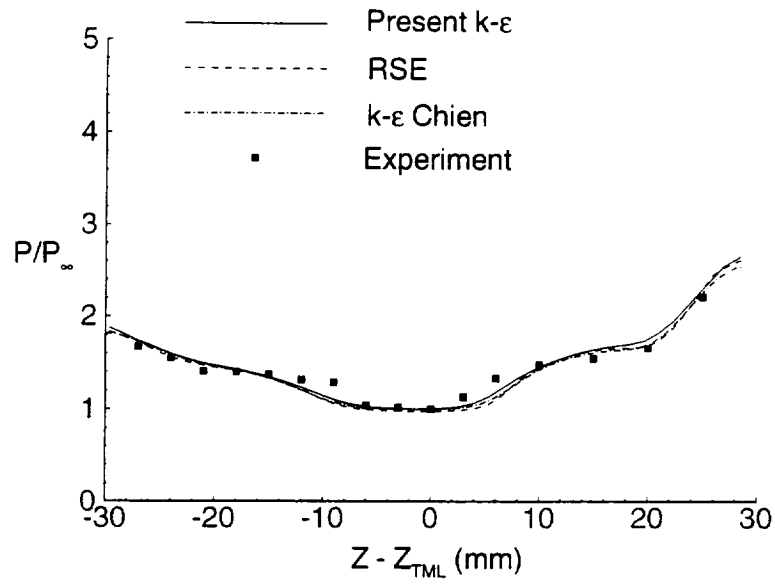
Figure 6.10: Wall pressure at $x = 46$ mm for $7° \times 11°$
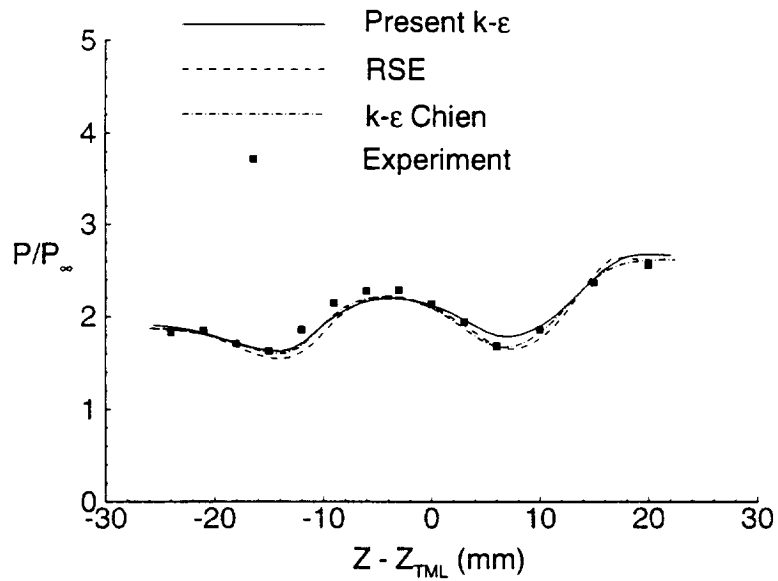
Figure 6.11: Wall pressure at $x = 79$ mm for $7° \times 11°$
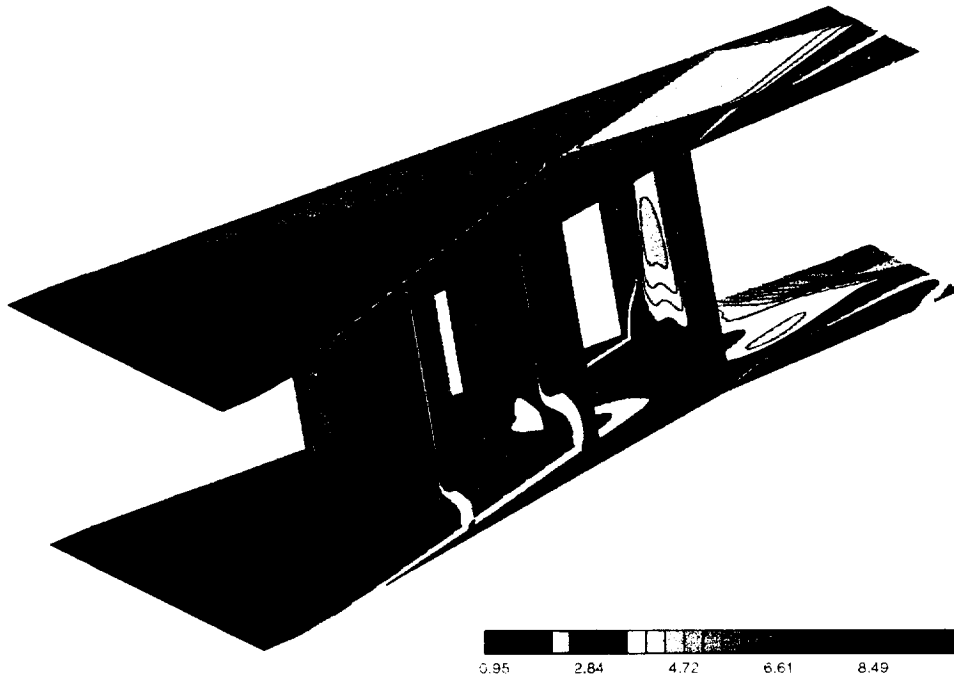
Figure 6.12: 3-D shock structure for $7° \times 11°$.

The 3-D wave structure is presented in Fig. 6.12, which contains nondimensional static pressure contours at the lower surface, in "inviscid" region and at three x locations. The 2-D pressure contours at three successive x locations are presented at Figs. 6.13, 6.15 and 6.17. Schematic plots of corresponding wave structure at each location are presented in Fig. 6.14, 6.16 and 6.18.

The pressure contours are in general agreement with corresponding results described in [24]. At $x = 46$mm (6.13) the pressure contours show two individual λ-shock structures, generated by two fins, which have not yet intersected. The single fin λ-shock structure, which is a result of the interaction of inviscid shock wave and developed boundary layer, is described in detail in [10]. The primary shock bifurcates into a separation shock and a rear shock. The separation vortex is located beneath the main shock. At $x = 79$mm inviscid shocks have not yet intersected, but separation shocks have reflected from one another. At $x = 112$mm inviscid shocks have already intersected, and, as described in [24], there is an expansion region in the central part of the flowfield, between the reflected shocks, which extends downward.
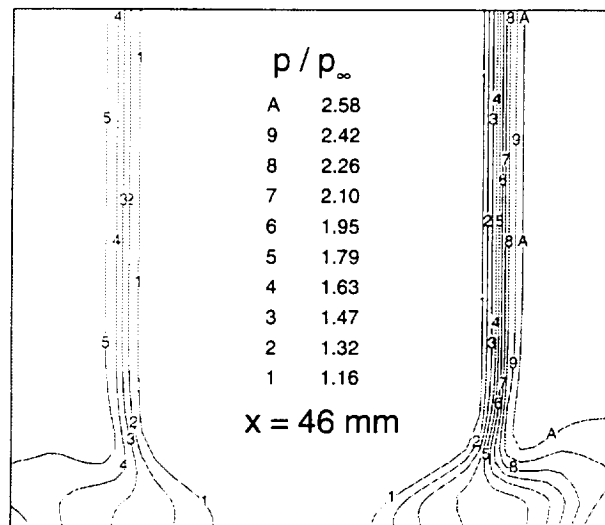
Figure 6.13: Pressure contours at $x = 46$ mm for $7° \times 11°$
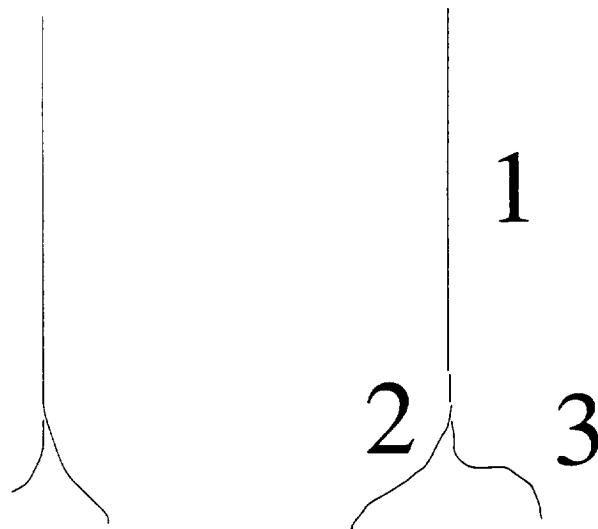
Figure 6.14: Wave structure at $x = 46$ mm for $7° \times 11°$:

1 Inviscid shock
2 Separation shock
3 Rear shock
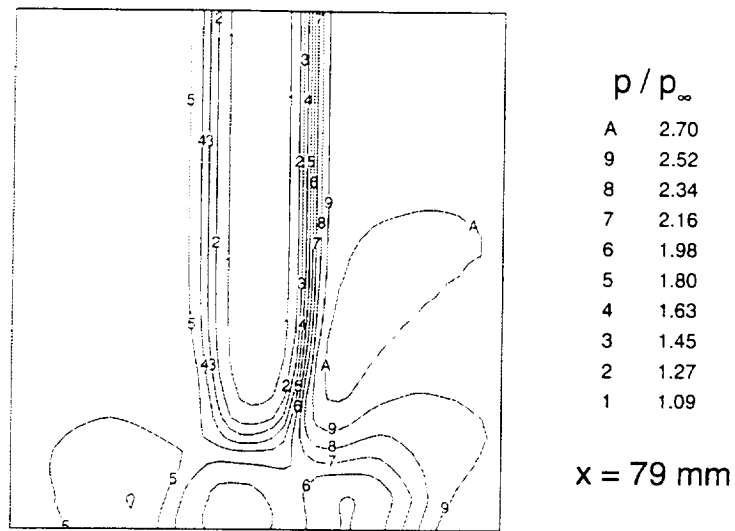
Figure 6.15: Pressure contours at $x = 79$ mm for $7° \times 11°$
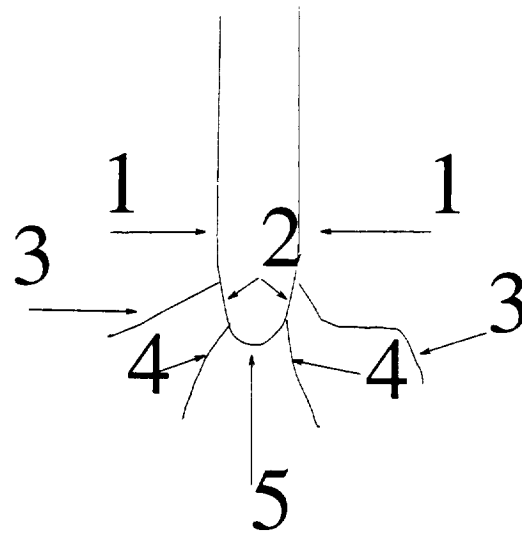
Figure 6.16: Wave structure at $x = 79$ mm for $7° \times 11°$:

1 Inviscid shock

2 Separation shock

3 Rear shock

4 Reflected separation shock

5 Bridge shock
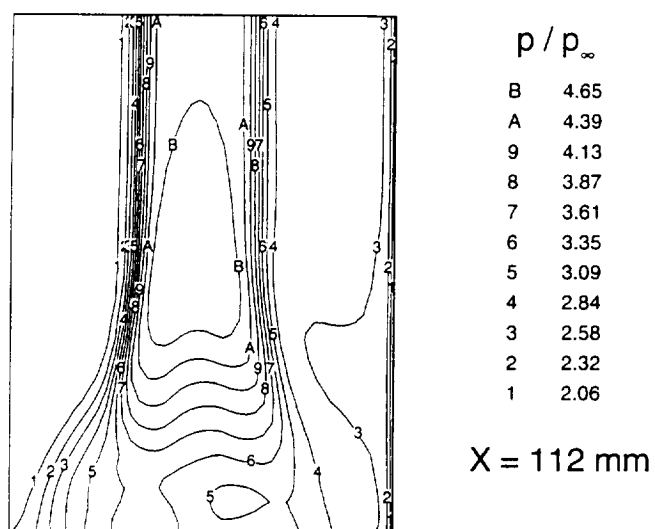
Figure 6.17: Pressure contours at $x = 112$ mm for $7° \times 11°$
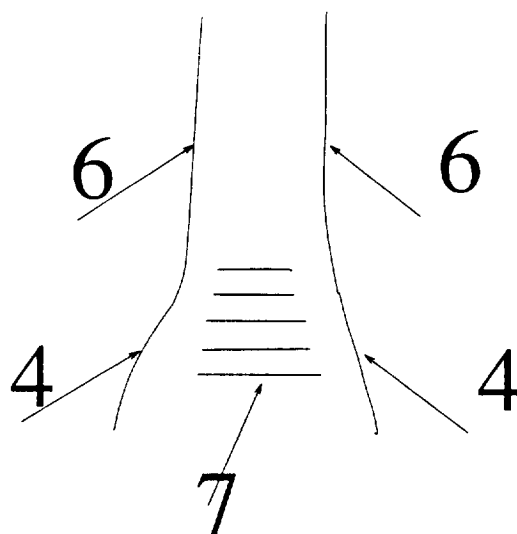
Figure 6.18: Wave structure at $x = 112$ mm for $7° \times 11°$

4 Reflected separation shock

6 Reflected inviscid shock

7 Expansion fan

The turbulence kinetic energy contours at the same three subsequent x locations are presented at Figs. 6.19, 6.20 and 6.21 together with 2-D "streamlines" in the $y - z$ plane. These three plots are made not to scale. The 2-D "streamlines" are not real streamlines, but curves tangent to the component of velocity in the $y - z$ plane. These lines are plotted to indicate the location of vortices. Unfortunately, no experimental measurements of turbulence kinetic energy are available for comparison.

The two maxima at Fig. 6.19 correspond to the individual separation vortices generated by two single fin interactions, with the highest k in the vortex which corresponds to the $11°$ fin. These vortices converge (Fig. 6.20) to form a counter-rotating vortex pair with a maximum of k located between two vortices. Similar to the results described in [61], downstream of the interaction (Fig. 6.21) the turbulence kinetic energy contours have a typical mushroom-like shape. The merged vortex pair has entrained most of the boundary layer. In a major difference with the results obtained with the RSE model [61], the maximum value of turbulence kinetic energy is two times lower, than similar value in [61]. The two vortices, obtained in the present computation, are significantly weaker than in [61]. All this differences may be attributable to the differences in turbulence models employed in the computation.

The computed and experimental surface heat transfer coefficient C_h is presented in Figs. 6.22 to 6.25. The uncertainty in the experimental heat transfer measurements is $\pm 10\%$ to 15%. The computed T_{aw}, required for the computation of C_h, is within 1 to 1.5% of the experimental measurement (see [24]) obtained using the thermovision technique as well as the thermocouple measurements. The x-locations represented at Figs. 6.23 and 6.24 are upstream of the interaction of the shocks. The computed heat transfer at these locations is in reasonable agreement with experimental values, but all experimental measurements where taken in the region of the flow located in front of the shocks. Downstream of the intersection of the fin-generated λ−shock structures ($i.e.$, for $x > 90$ mm on the TML) the computations with all three considered turbulence models overpredict the heat transfer by approximately a factor of two, with a modest improvement in the computations performed with RSE and present models. This discrepancy is attributable to the limitations of turbulence models. Comparison of the
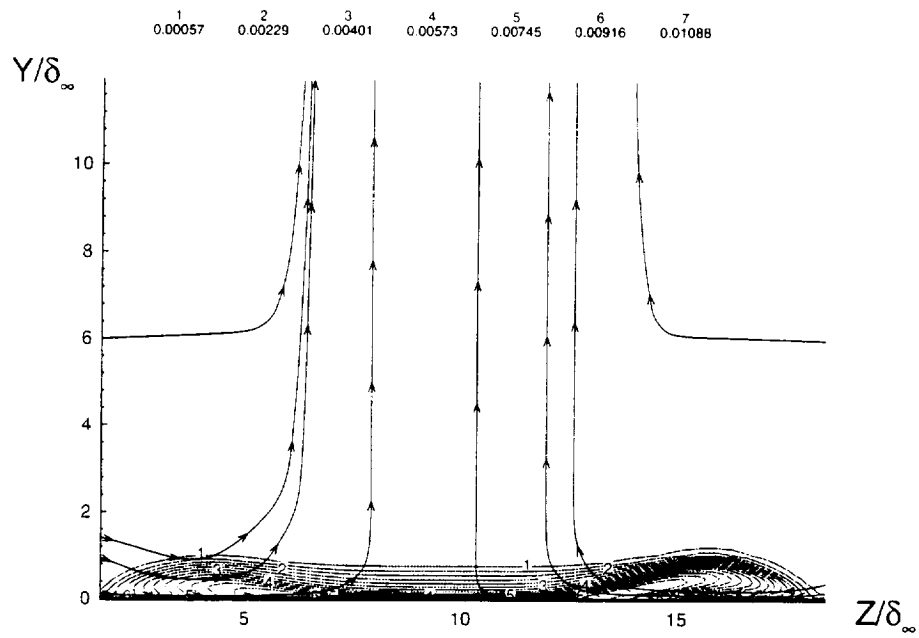
Figure 6.19: Turbulence kinetic energy contours at $x = 46$ mm for $7° \times 11°$
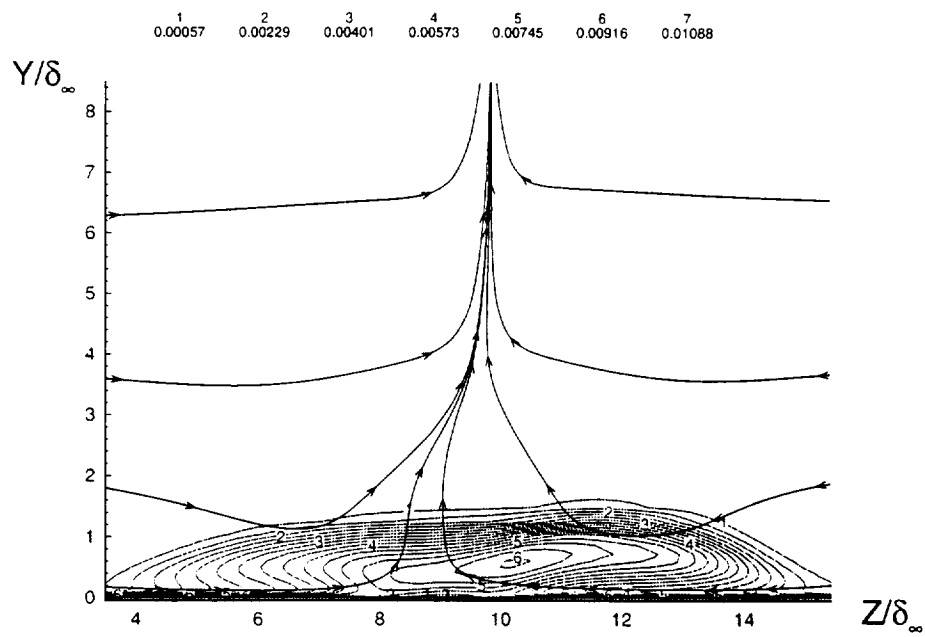
Figure 6.20: Turbulence kinetic energy contours at $x = 79$ mm for $7° \times 11°$
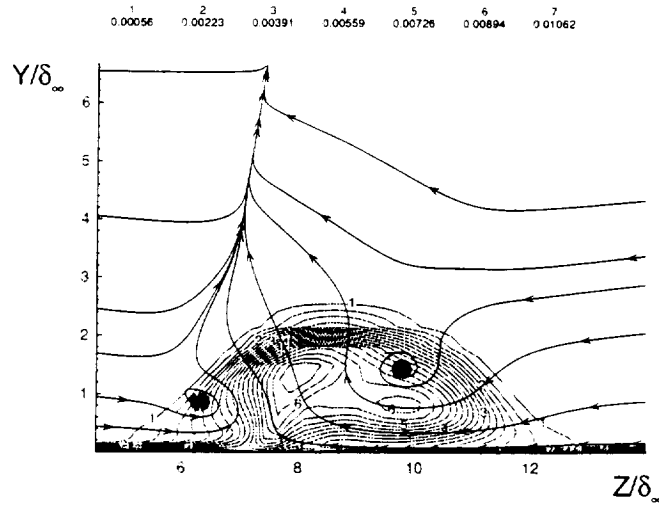
Figure 6.21: Turbulence kinetic energy contours at $x = 112$ mm for $7° \times 11°$

computed and experimental heat transfer at $x = 112$ mm downstream of the intersection of the λ–shock structures, shows significant disagreement. In summary, the computed C_h displays qualitatively the trends observed in the experiment, but does not provide reliable values downstream of the interaction of the λ-shocks.

The computed and experimental adiabatic wall temperature distributions in streamwise and spanwise directions are displayed in Figs. 6.26 to 6.29 respectively. The results are compared to the computational results from [24] and [61]. Figs.6.30-6.33 contain comparison of the adiabatic wall temperature to the experimental results, obtained with two different techniques: thermocouple and thermovision measurements. The experimental uncertainty in the adiabatic wall temperature measurements is extremely low ($\pm 0.15°K$). The results of the present computation exhibit excellent agreement with the experiment.

Figs. 6.34 and 6.35 contain contour plots of the adiabatic wall temperature, nondimensionalized by the adiabatic wall temperature at infinity. The experimental results were obtained using thermovision technique.

The results are in qualitative agreement. Computations correctly predict a slight temperature rise downstream of the interaction of the two crossing shocks and in the vicinity of the line of coalescence of the two vortices. The temperature decrease at the
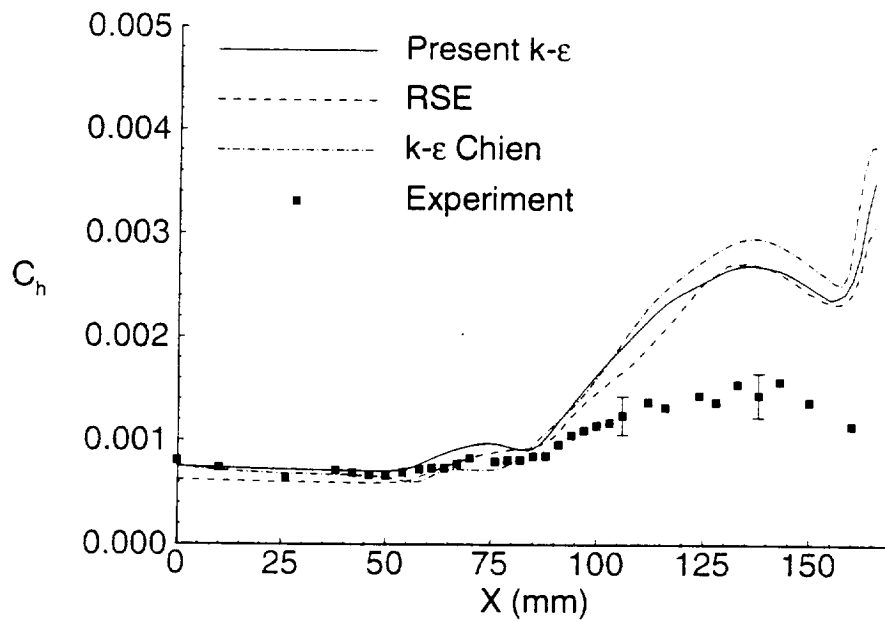
Figure 6.22: Heat transfer on TML for $7° \times 11°$
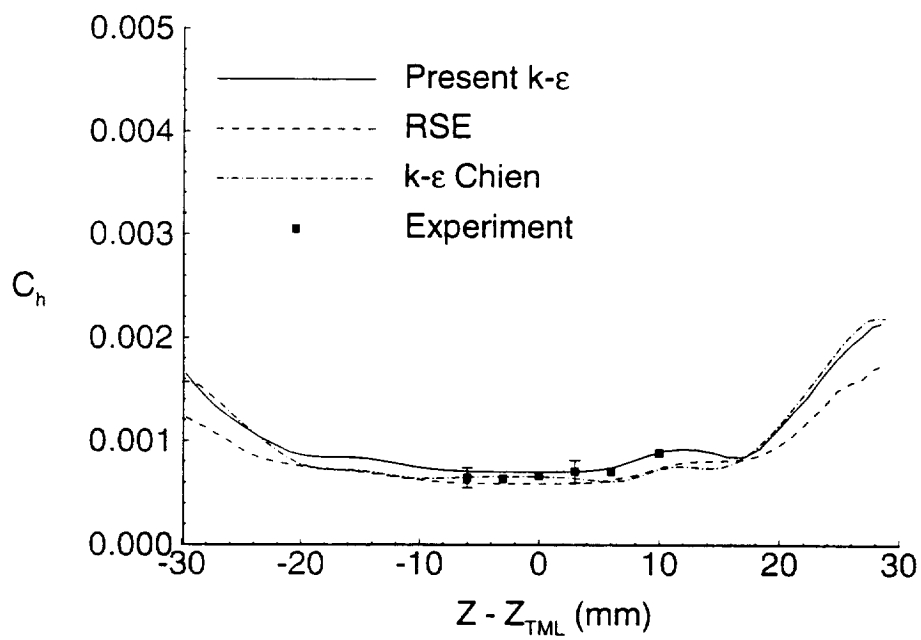
Figure 6.23: Heat transfer at $x = 46$ mm for $7° \times 11°$
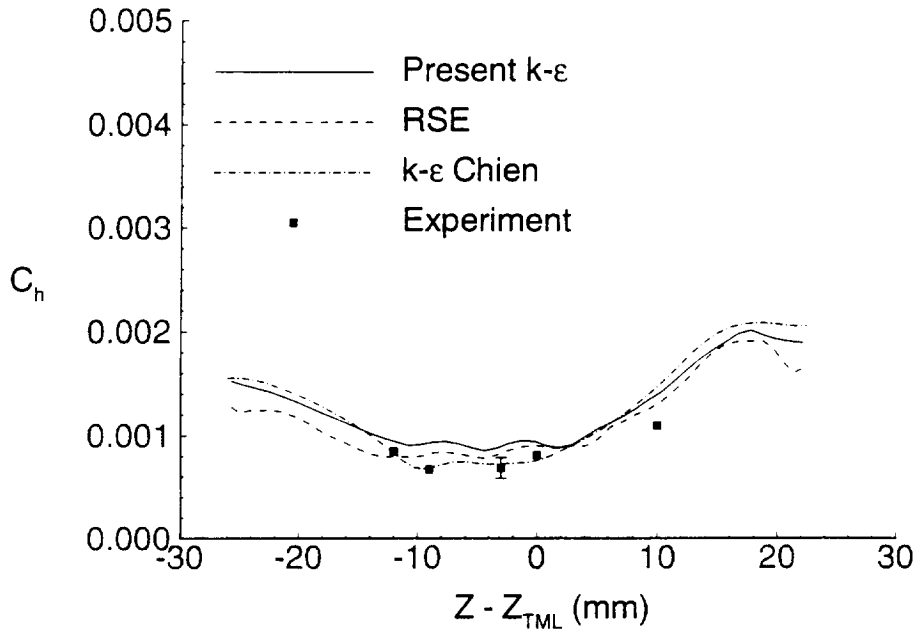
Figure 6.24: Heat transfer at $x = 79$ mm for $7° \times 11°$
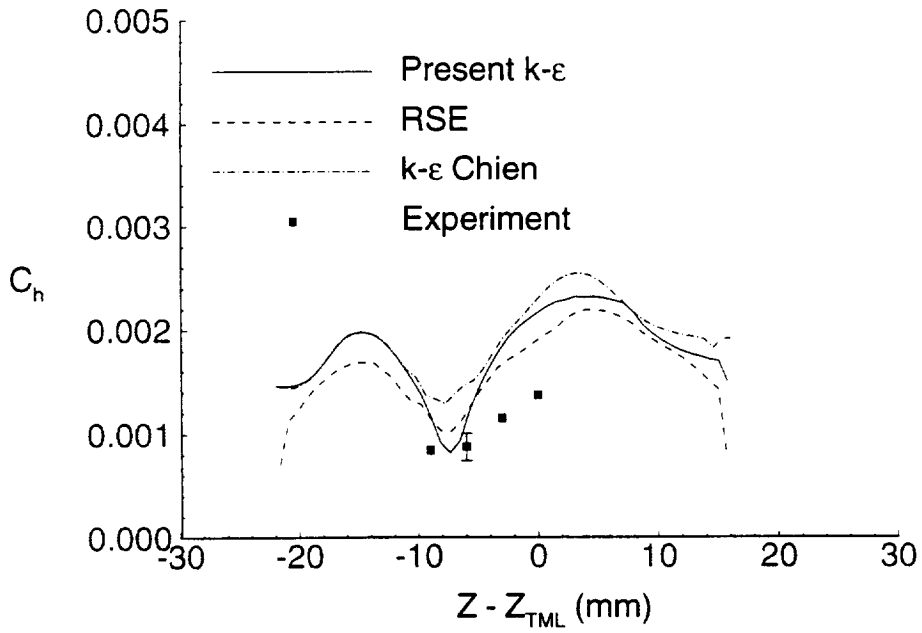
Figure 6.25: Heat transfer at $x = 112$ mm for $7° \times 11°$

rarefaction fan when the flow expands behind the corner at 11° fin, is also predicted. The computational results for the temperature at x/δ_{∞} more than 42 are not accurate, since information in these locations is affected by the shocks reflected from the side walls. However, in the present computations boundary layers on the side wall surfaces are not resolved and fins are treated as inviscid boundaries.
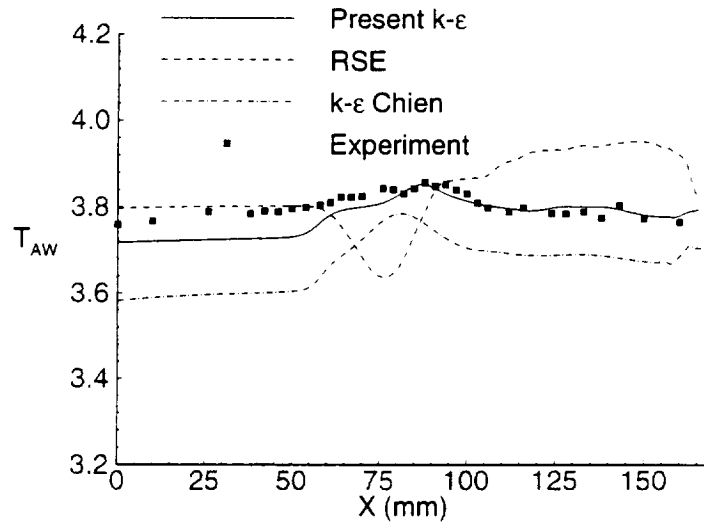
Figure 6.26: Adiabatic wall temperature on TML for $7^{\circ} \times 11^{\circ}$

Figure 6.27: Adiabatic wall temperature at $x = 46$ mm for $7^{\circ} \times 11^{\circ}$

Figure 6.28: Adiabatic wall temperature at $x = 79$ mm for $7° \times 11°$
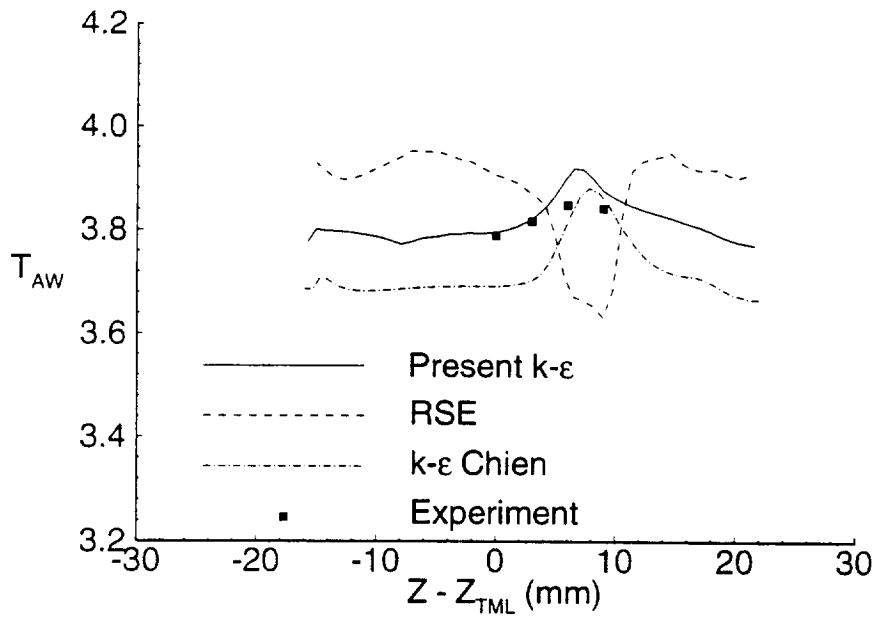
Figure 6.29: Adiabatic wall temperature at $x = 112$ mm for $7° \times 11°$
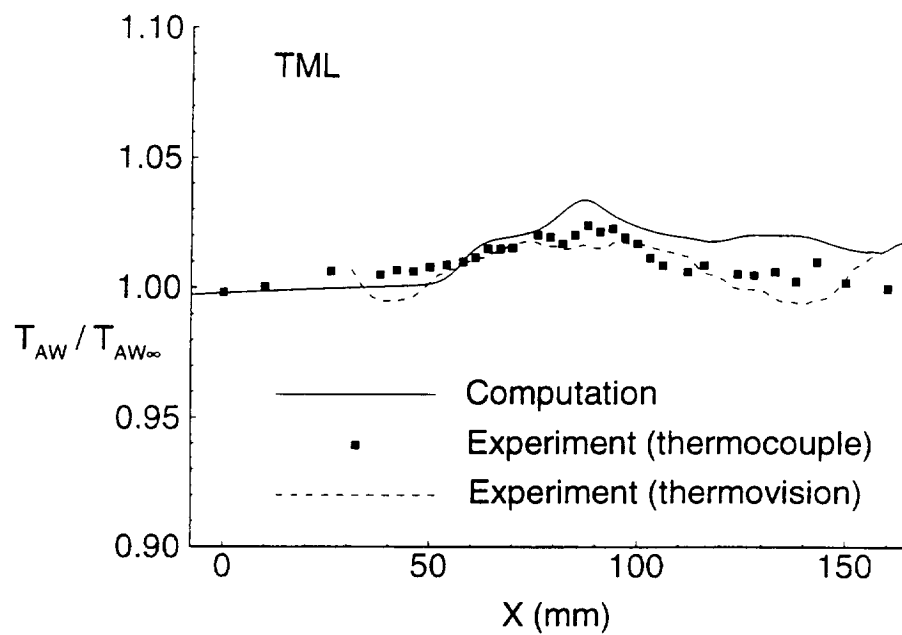
Figure 6.30: Adiabatic wall temperature on TML for $7° \times 11°$
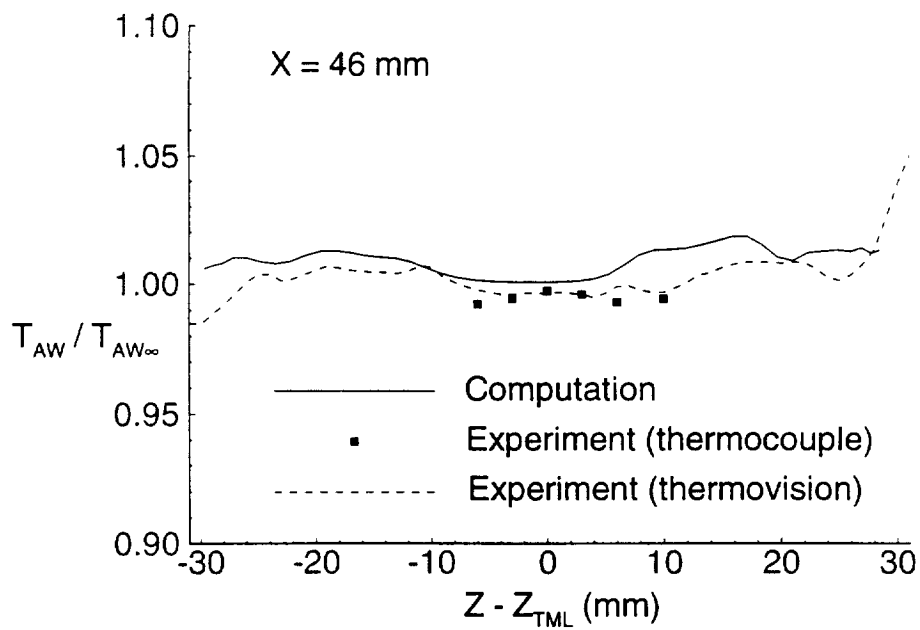
Figure 6.31: Adiabatic wall temperature at $x = 46$ mm for $7° \times 11°$
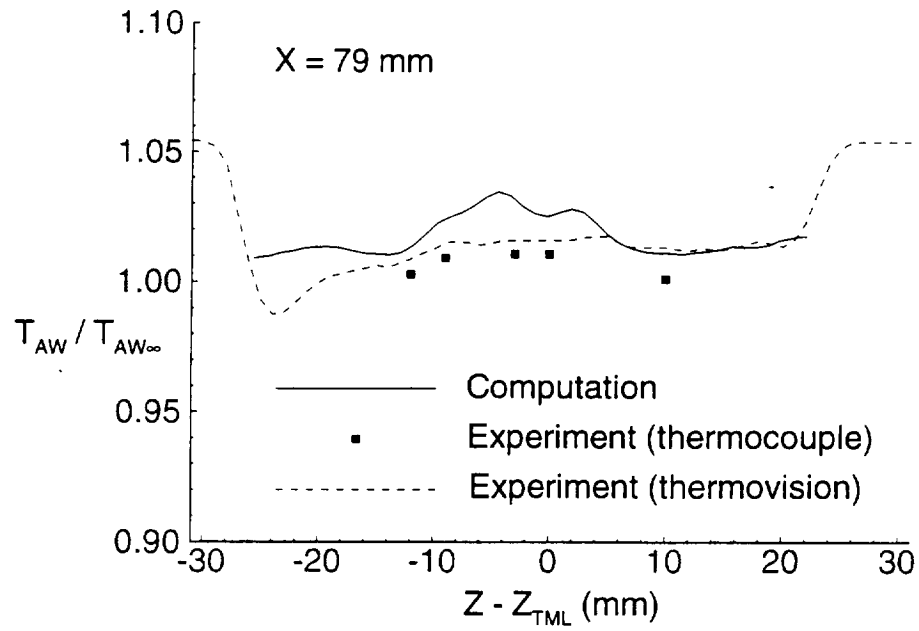
Figure 6.32: Adiabatic wall temperature at $x = 79$ mm for $7° \times 11°$
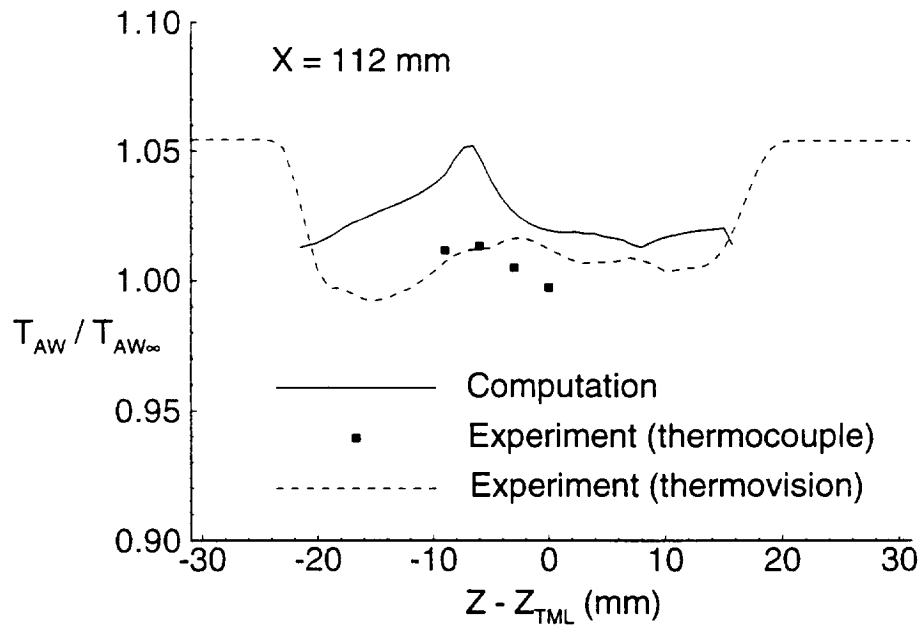
Figure 6.33: Adiabatic wall temperature at $x = 112$ mm for $7° \times 11°$

COMPUTATION T_{AW} / T_{AW}

| 1 | 2 | 3 | 4 | 5 | 6 | 7 | 8 |
| 0.968 | 0.981 | 0.994 | 1.007 | 1.020 | 1.032 | 1.045 | 1.058 |

X / δ

| | | | |
| 10 | 20 | 30 | 40 |
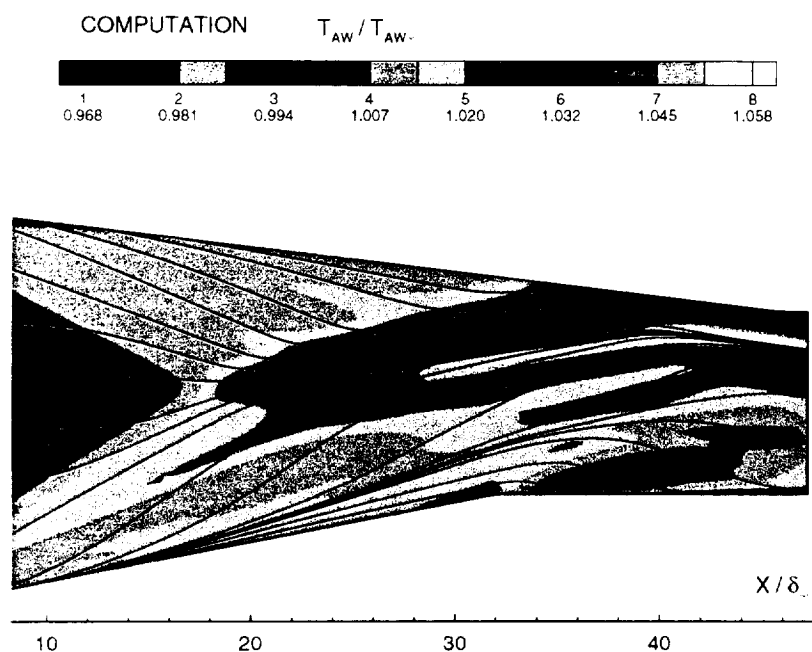
Figure 6.34: Adiabatic wall temperature contours for $7° \times 11°$: computation

EXPERIMENT T_{AW} / T_{AW} $T_{AW} = 239$ K

| 1 | 2 | 3 | 4 | 5 | 6 | 7 | 8 |
| 0.968 | 0.981 | 0.994 | 1.007 | 1.020 | 1.032 | 1.045 | 1.058 |

X / δ

| | | | |
| 10 | 20 | 30 | 40 |
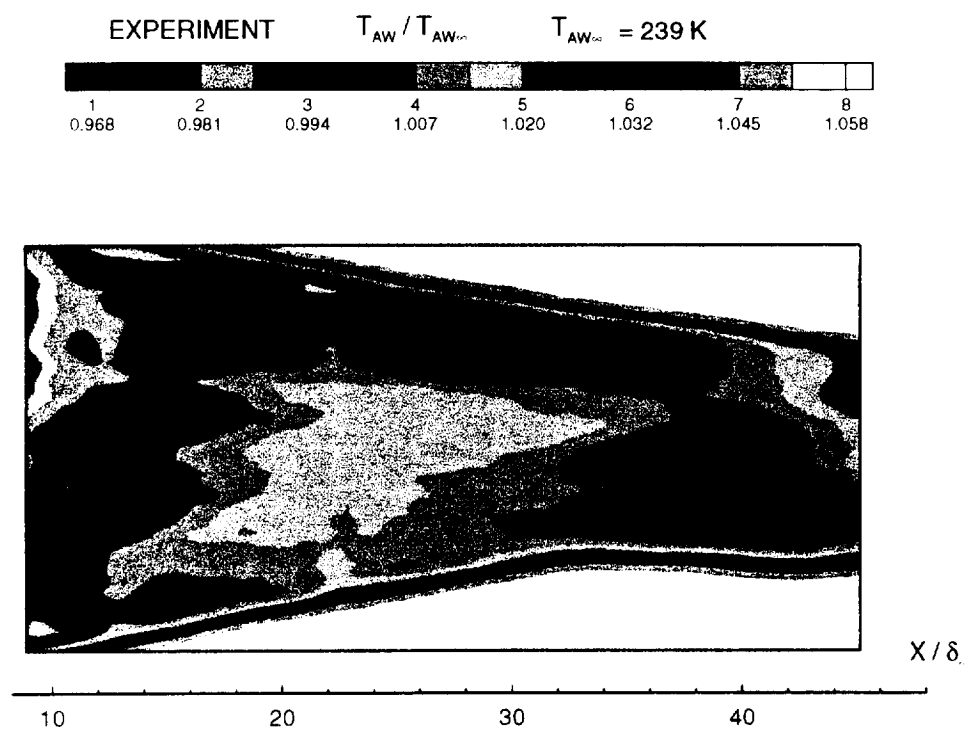
Figure 6.35: Adiabatic wall temperature contours for $7° \times 11°$: experiment

6.2 Crossing Shock $7° \times 7°$

The computed skin friction lines and experimental surface flow visualization for the $7° \times 7°$ configuration are presented in Figs. 6.36 and 6.37, respectively. The separation lines originating from the fin leading edges are apparent in the computation and experiment. The computed and experimental separation line angles agree within 7%. Similar to the previous case, the computed skin friction lines do not intersect, but, after changing direction, slowly converge towards each other. Two weak divergence lines **3** and **4** can be found near the fin surfaces. The computational flow pattern is completely symmetric, however, experimental results display slight asymmetric behavior downstream in the vicinity of the centerline.

The computed and experimental surface pressure, normalized by the freestream static pressure p_∞, are displayed in Figs. 6.38 and 6.39 along the Throat Middle Line and at the three streamwise locations. The computed and experimental surface pressure on TML and in all three x locations are in excellent agreement with experiment.

The computed and experimental surface heat transfer coefficient C_h is presented in Figs. 6.40 to 6.43. The results exhibit significantly better agreement with the experimental measurements than in the previously considered $7° \times 11°$ configuration case. Even downstream of the crossing shock intersection (*i.e.* for $x > 90$ mm on the TML) the computations are virtually within the experimental uncertainty. The adiabatic wall temperature, presented in Figs. 6.44 to 6.47) is again in excellent agreement with experiment.

It is not yet clear why the same turbulence model provides for good heat transfer predictions in the $7° \times 7°$ case and for much worse predictions in the $7° \times 11°$ case. A possible explanation, suggested by Dr. A.A. Zheltovodov, is the partial relaminarization of the flow under the influence of the favorable crossflow pressure gradient, which can cause a decline in the value of the heat transfer coefficient in the $7° \times 11°$ case. The regions of favorable pressure gradient are evident in Fig. 6.4, where surface streamlines are colored according to *static pressure*.
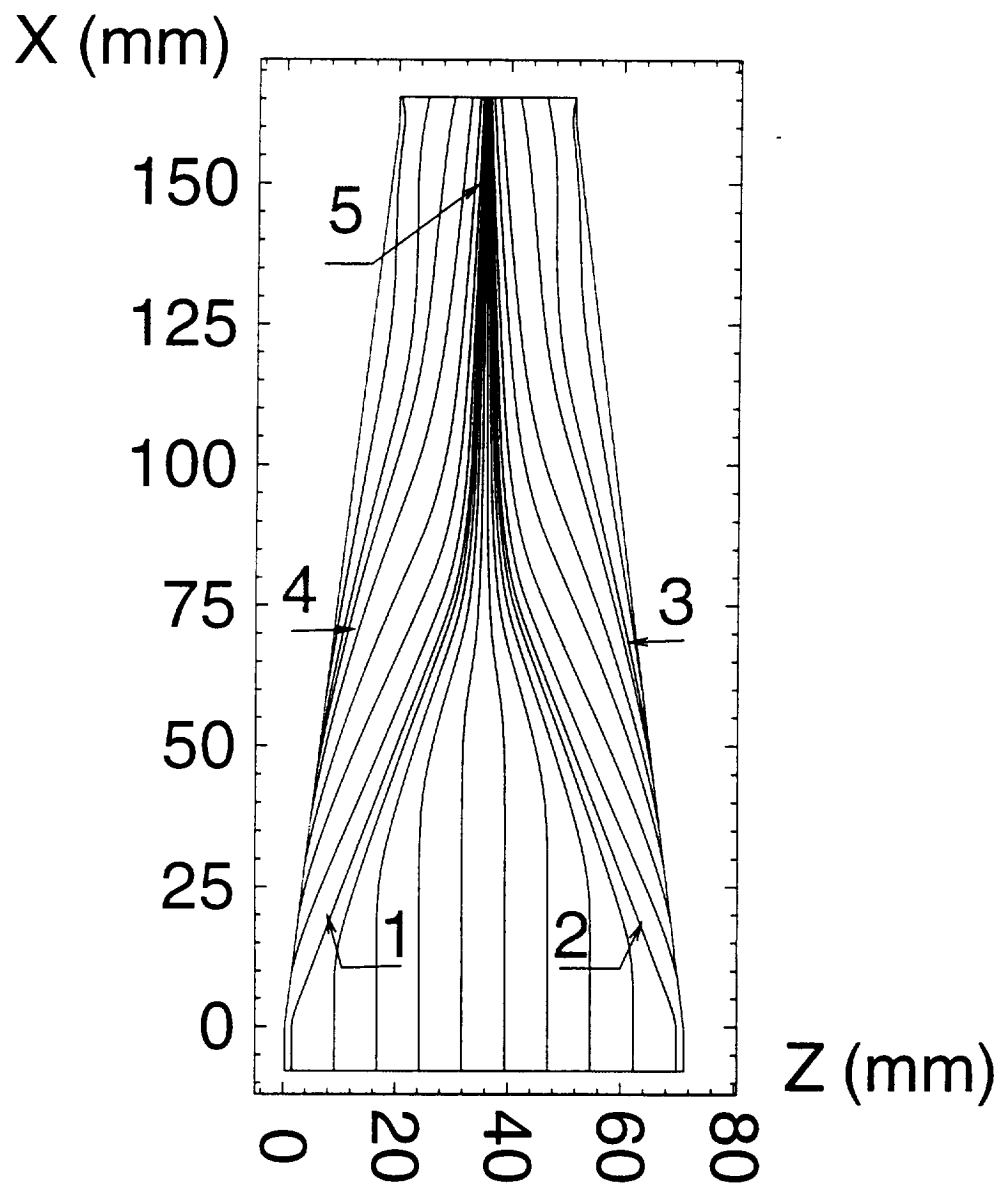
Figure 6.36: Computed skin friction lines for 7° × 7°:

1 Left incident separation line

2 Right incident separation line

3, 4 Lines of divergence

5 Downstream coalescence line

Figure 6.37: Experimental surface flow for 7° × 7°
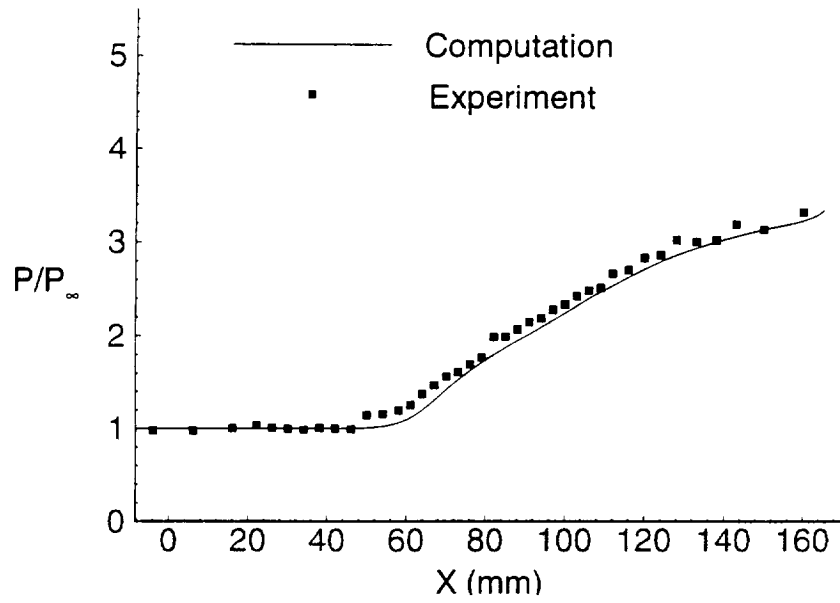
Figure 6.38: Wall pressure on TML for $7° \times 7°$
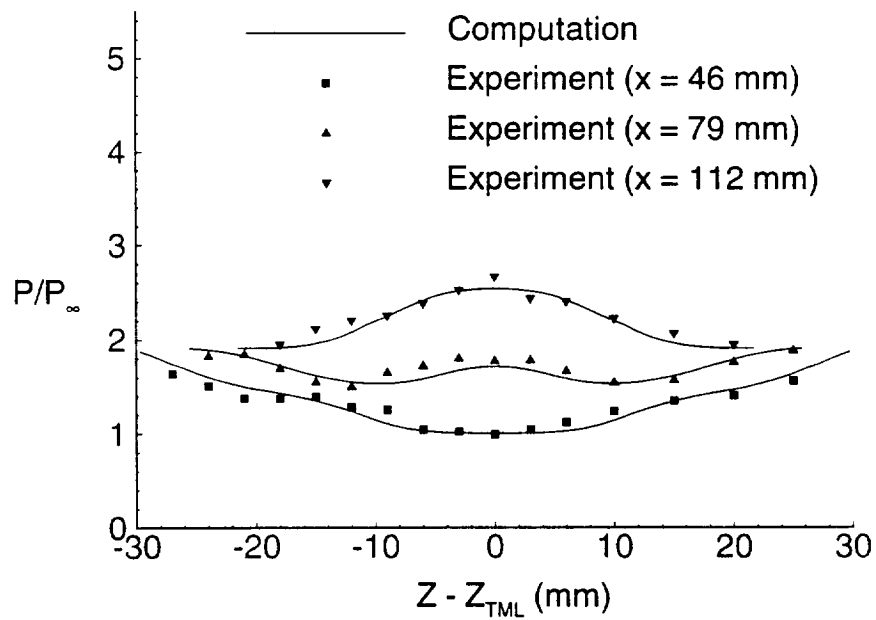
Figure 6.39: Wall pressure at $x = 46$ mm, $x = 79$ mm and $x = 112$ mm for $7° \times 7°$
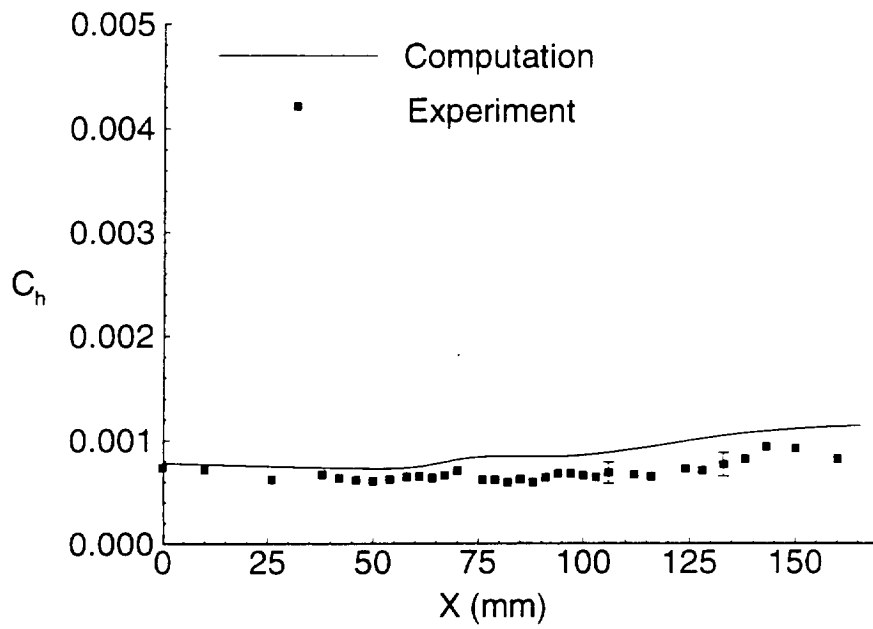
Figure 6.40: Heat transfer on TML for $7° \times 7°$
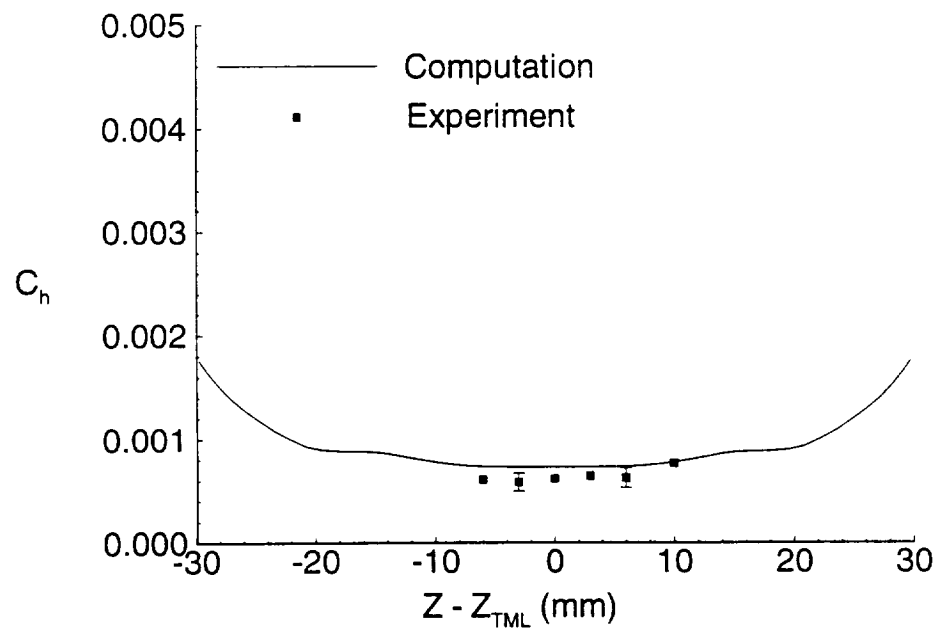
Figure 6.41: Heat transfer at $x = 46$ mm for $7° \times 7°$
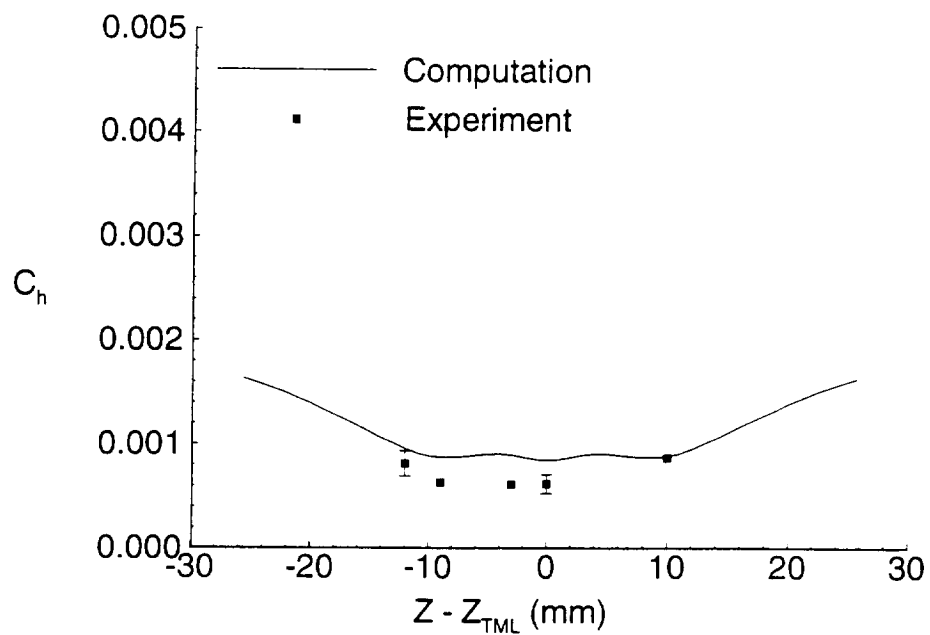
Figure 6.42: Heat transfer at x = 79 mm for $7° \times 7°$
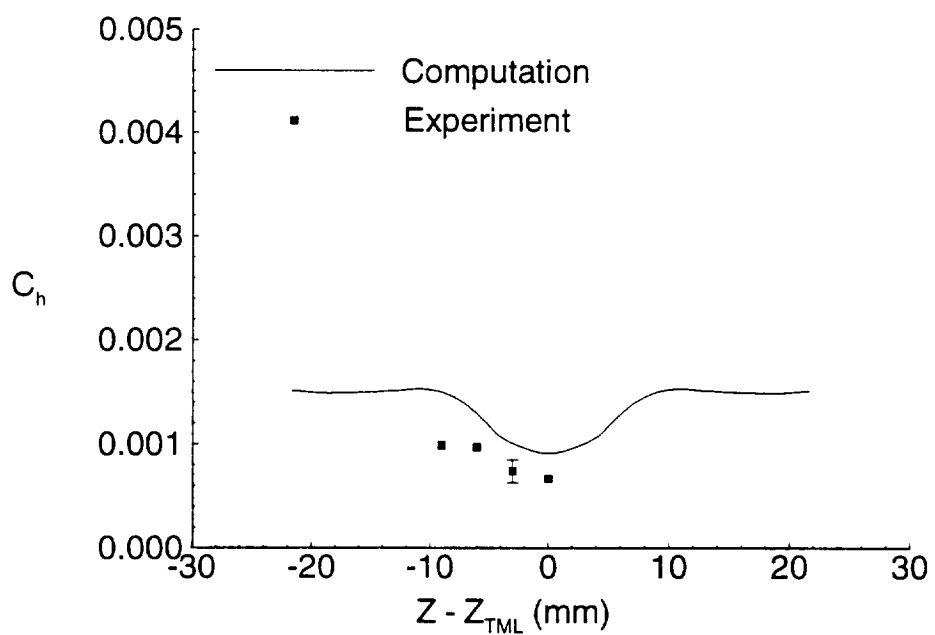
Figure 6.43: Heat transfer at x = 112 mm for $7° \times 7°$
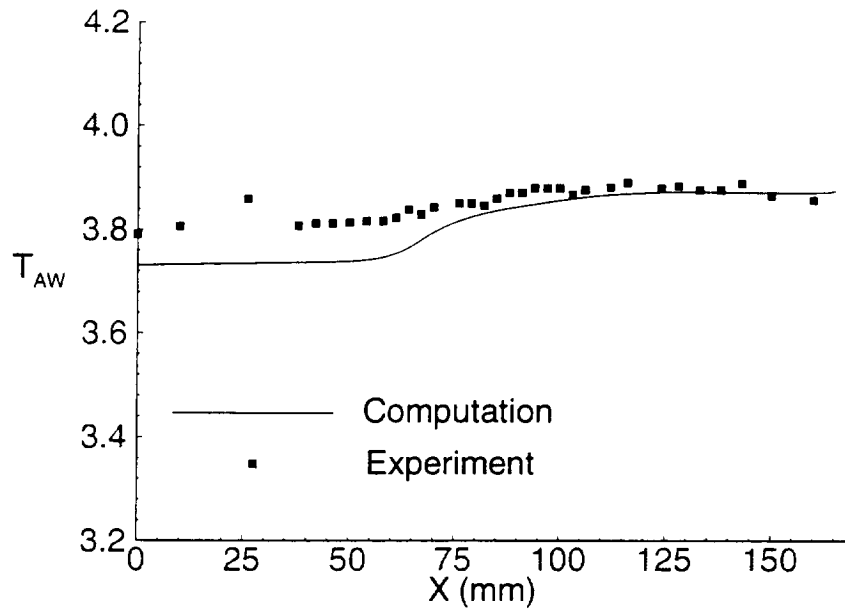
Figure 6.44: Adiabatic wall temperature on TML for 7° × 7°
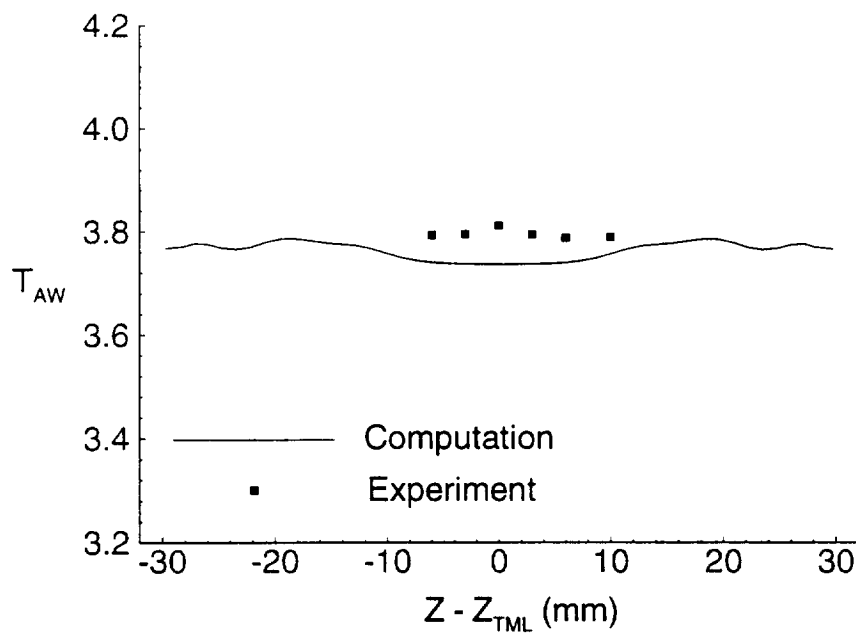
Figure 6.45: Adiabatic wall temperature at $x = 46$ mm for 7° × 7°
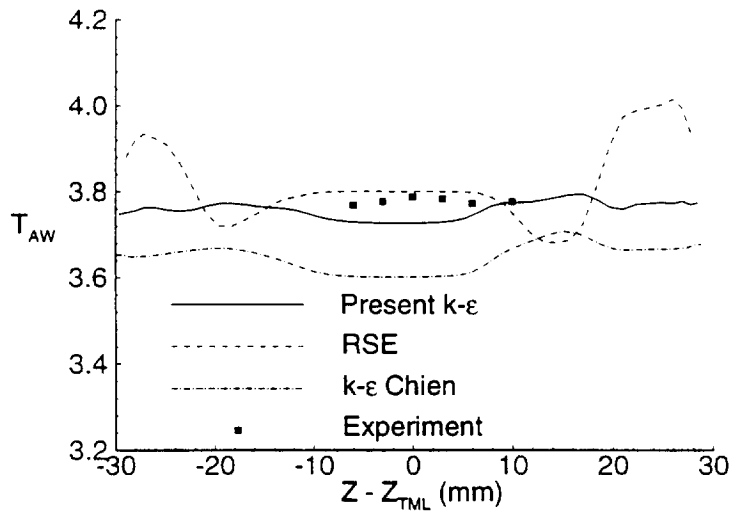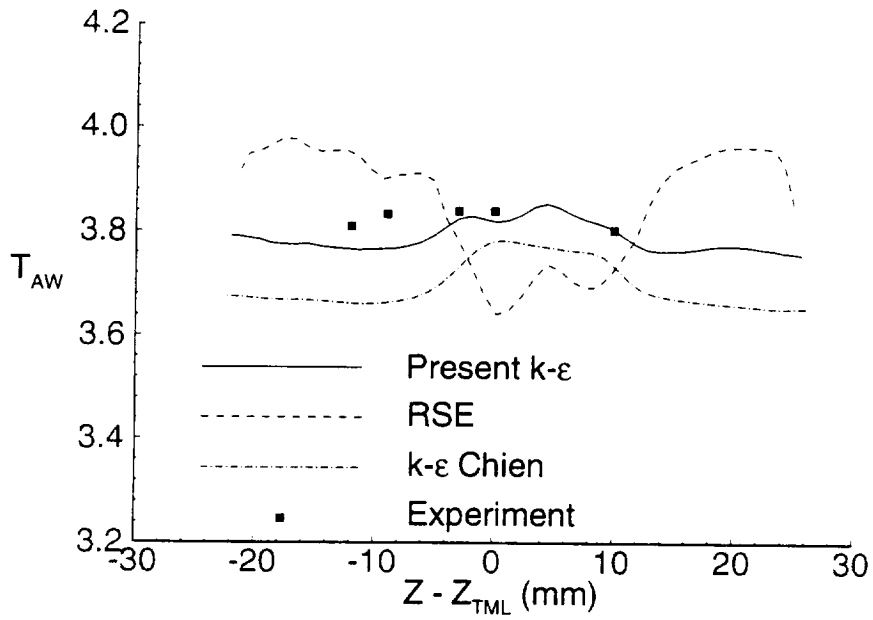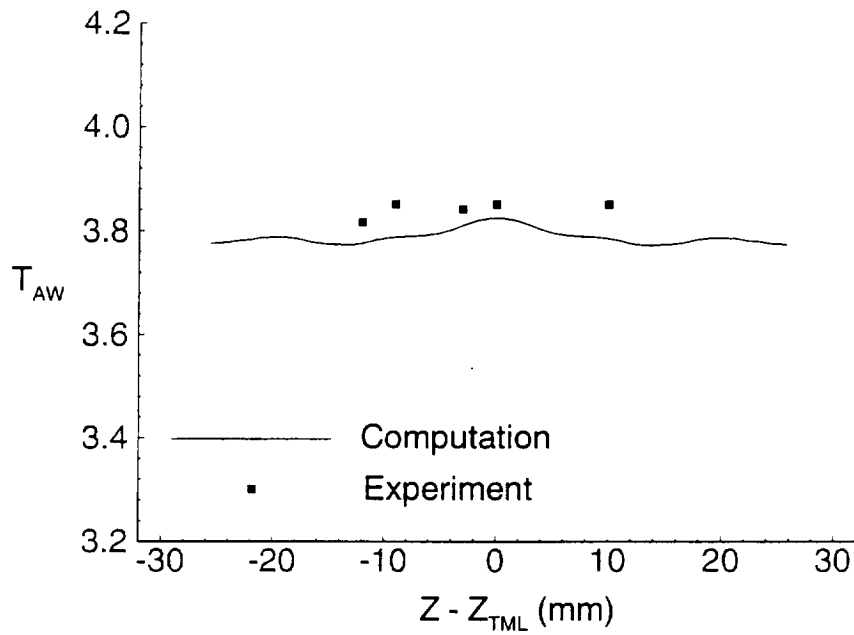
Figure 6.46: Adiabatic wall temperature at $x = 79$ mm for $7° \times 7°$
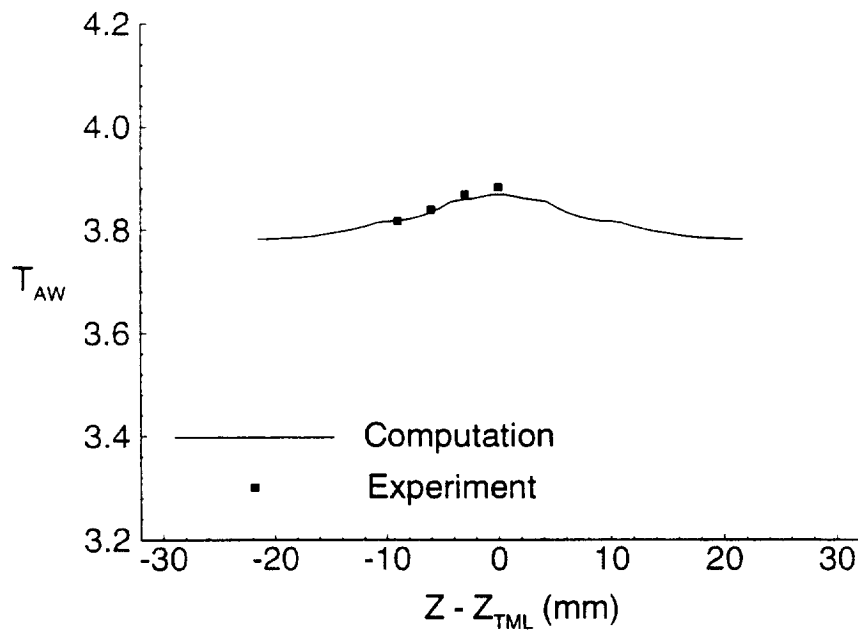
Figure 6.47: Adiabatic wall temperature at $x = 112$ mm for $7° \times 7°$

6.3 Crossing Shock $15° \times 15°$

The computed skin friction lines and experimental surface flow visualization for the $15° \times 15°$ configuration are presented in Figs. 6.48 and 6.49, respectively. The two separation lines 1 and 2 originating from the fin leading edges are apparent in the computation and experiment. The computed and experimental separation line angles agree within 12%. The computed skin friction lines show complex behavior in the vicinity of the intersection of the separation lines (Fig. 6.50). Two lines of coalescence 3 and 4, which are caused by secondary separation of the low Mach number fluid beneath the previously separated main flow [24], form downstream in qualitative agreement with experiment. The second coalescence line was not present in previous computations which may be attributable to the insufficient resolution. Two strong divergence lines 5 and 6 are located near the fin surfaces.

The computed and experimental surface pressure, normalized by the freestream static pressure p_∞, are displayed in Figs. 6.51 and 6.52-6.54 along the Throat Middle Line and at the three streamwise locations respectively. The computed surface pressure on the centerline is overpredicted by 22 % in the vicinity of the crossing shock interaction. However, pressure distribution in spanwise direction is in good agreement with the experiment.

The computed and experimental surface heat transfer coefficient C_h is presented in Figs. 6.55 to 6.58. The x-location represented at Figs. 6.23 is upstream of the interaction of the shocks and the computed heat transfer at this location is in reasonable agreement with experimental values. As in the previously considered $7° \times 11°$ case, computation overpredicts the heat transfer rate downstream of the interaction by a factor of 1.8. Computation also predicts significant drop in heat transfer coefficient at the intersection point, which is not present in experimental results. Comparison of the computed and experimental heat transfer at $x = 79$ and $x = 112$ mm downstream of the intersection of the λ–shock structures, shows significant disagreement.

Unlike in the previous computations, the adiabatic wall temperature along the centerline presented in Fig. 6.59, is 3% higher than corresponding experimental result after
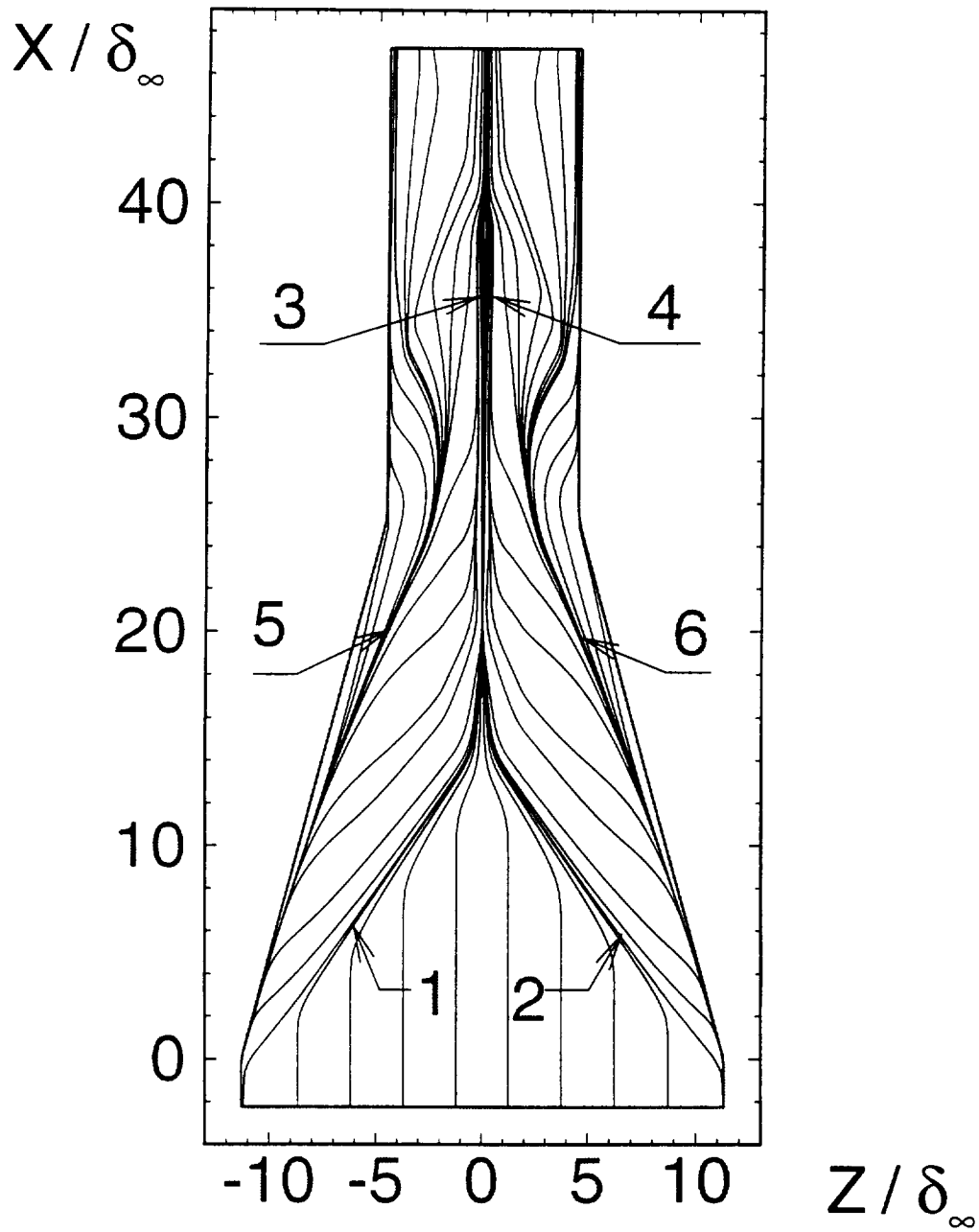
Figure 6.48: Computed skin friction lines for $15° \times 15°$:

1 Left incident separation line

2 Right incident separation line

3 Left downstream coalescence line

4 Right downstream coalescence line

5,6 Lines of divergence
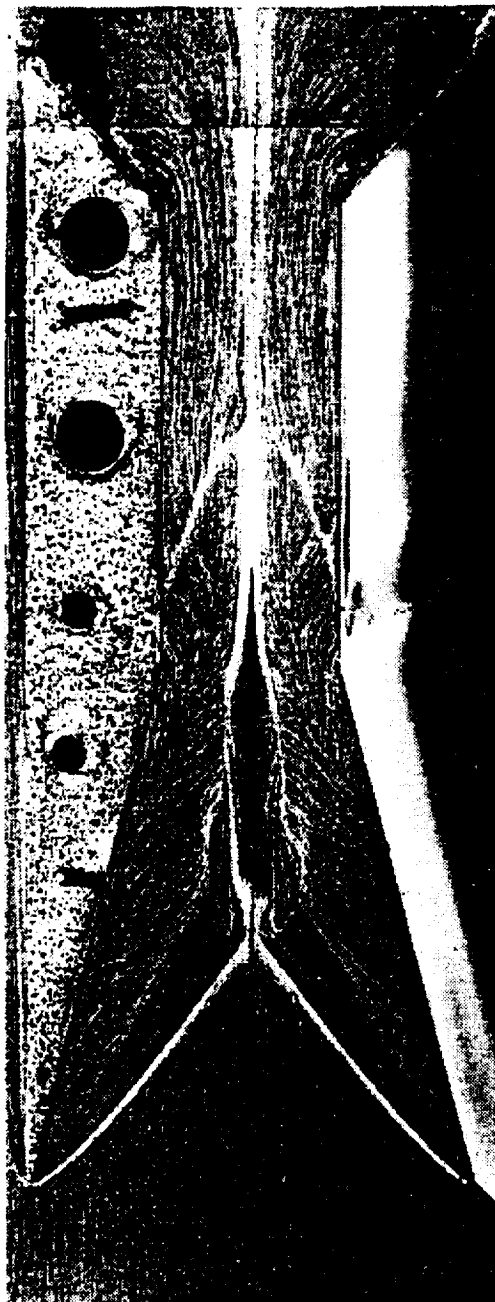
Figure 6.49: Experimental surface flow for 15° × 15°
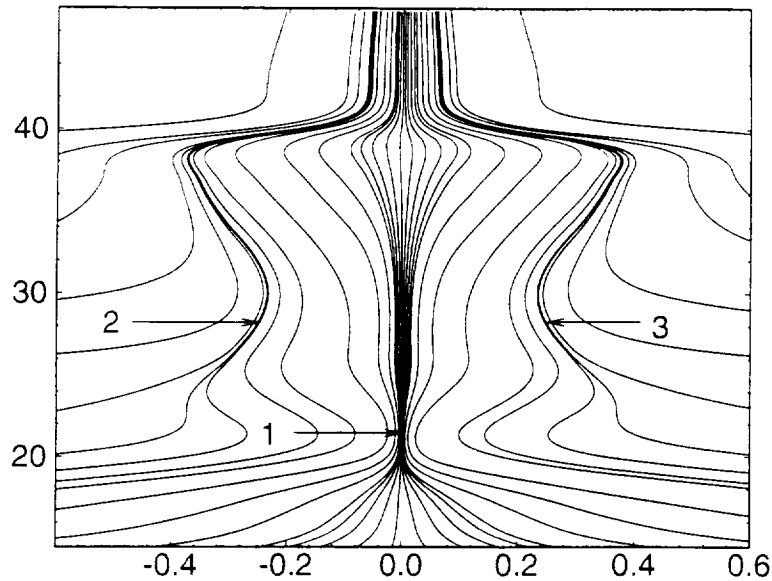
Figure 6.50: Computed skin friction lines for $15° \times 15°$ in the vicinity of the intersection point:

1 Intersection point

2 Left downstream coalescence line

3 Right downstream coalescence line.

the shock intersection. However, the streamwise temperature distribution (Figs. 6.60 to 6.62) is again in excellent agreement with experiment.

Figs. 6.63 and 6.64 contain contour plots of the adiabatic wall temperature, nondimensionalized by the adiabatic wall temperature at infinity. The experimental results were obtained using thermovision technique. The results are in qualitative agreement. Computations overpredict by several percent a slight temperature rise at the centerline and in the vicinity of the lines of coalescence downstream of the interaction of the two crossing shocks. The temperature decrease at the rarefaction fan when the flow expands behind the corners, is also predicted.
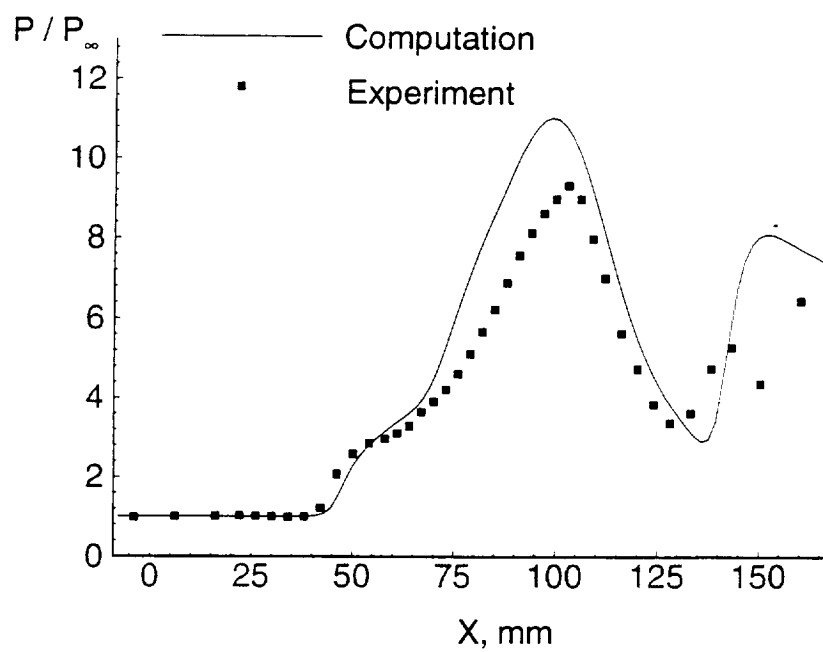
Figure 6.51: Wall pressure on TML for $15° \times 15°$
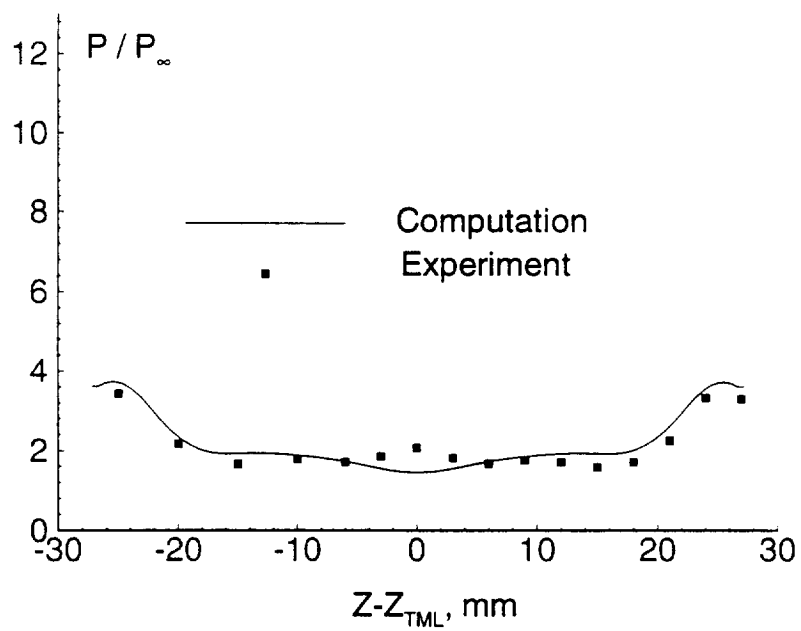
Figure 6.52: Wall pressure at $x = 46$ mm for $15° \times 15°$
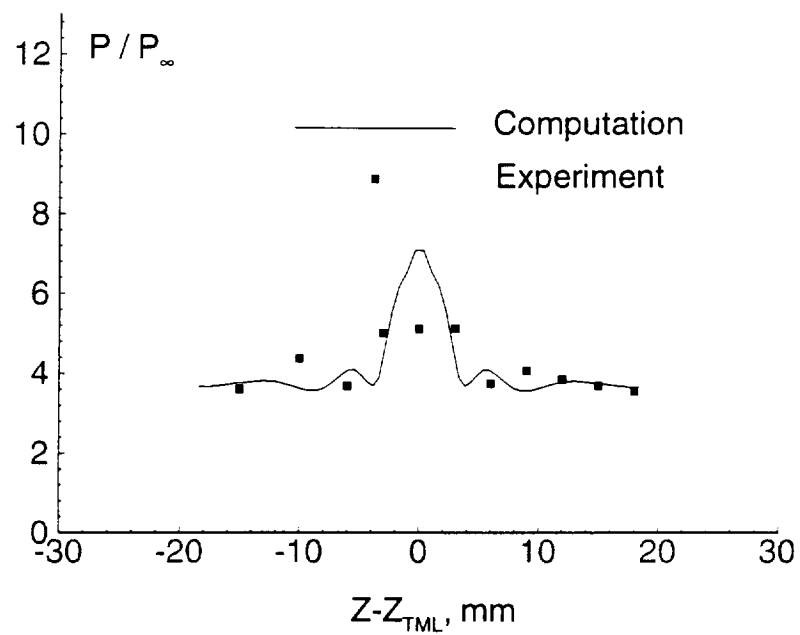
Figure 6.53: Wall pressure at $x = 79$ mm for $15° \times 15°$
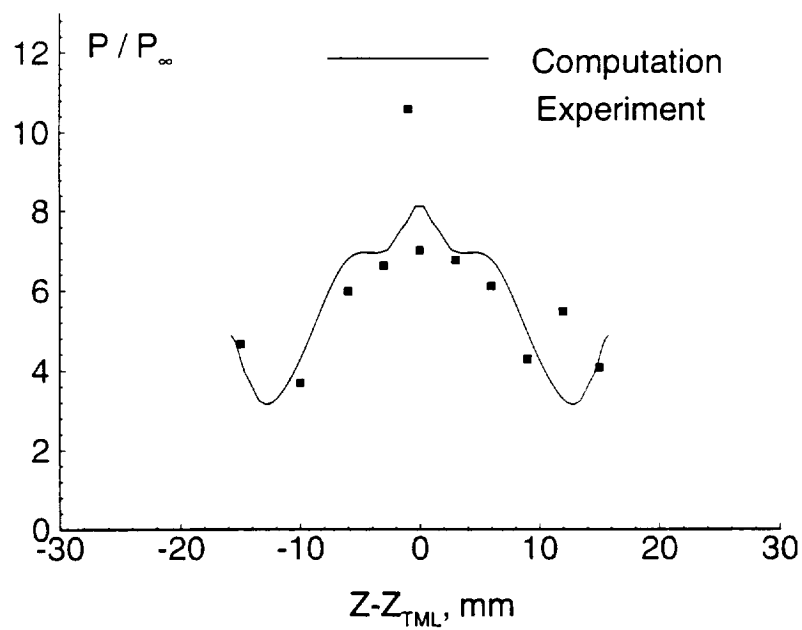
Figure 6.54: Wall pressure at $x = 112$ mm for $15° \times 15°$
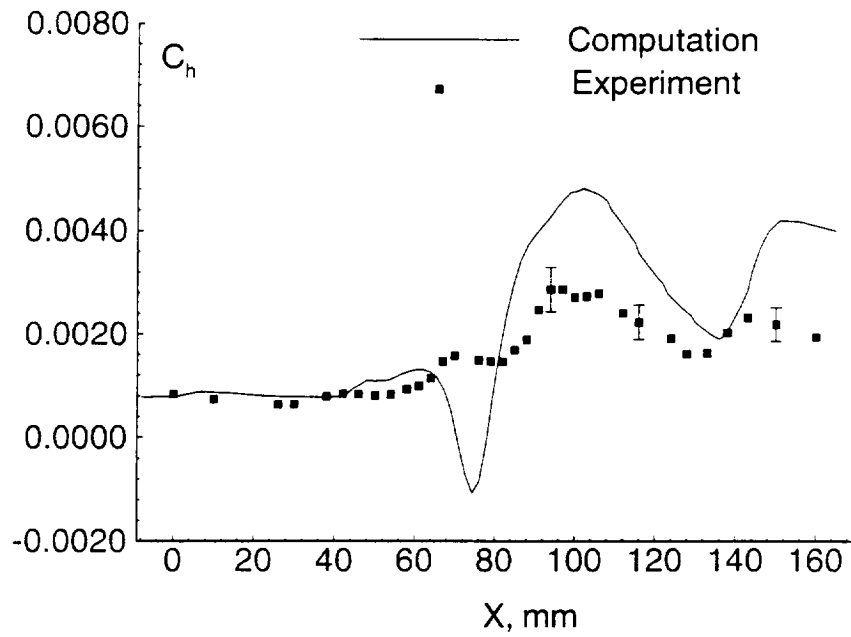
Figure 6.55: Heat transfer on TML for 15° × 15°
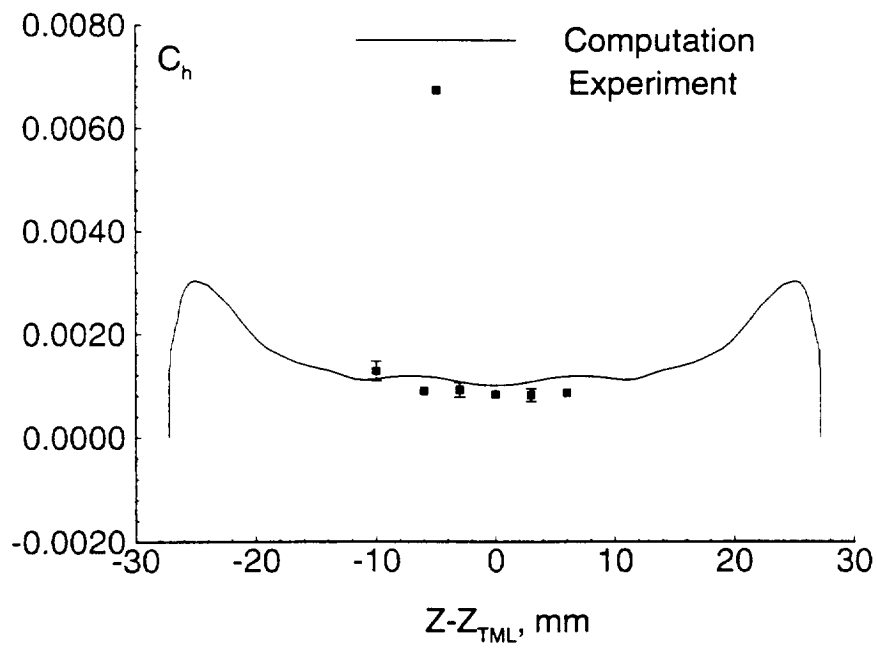
Figure 6.56: Heat transfer at $x = 46$ mm for 15° × 15°
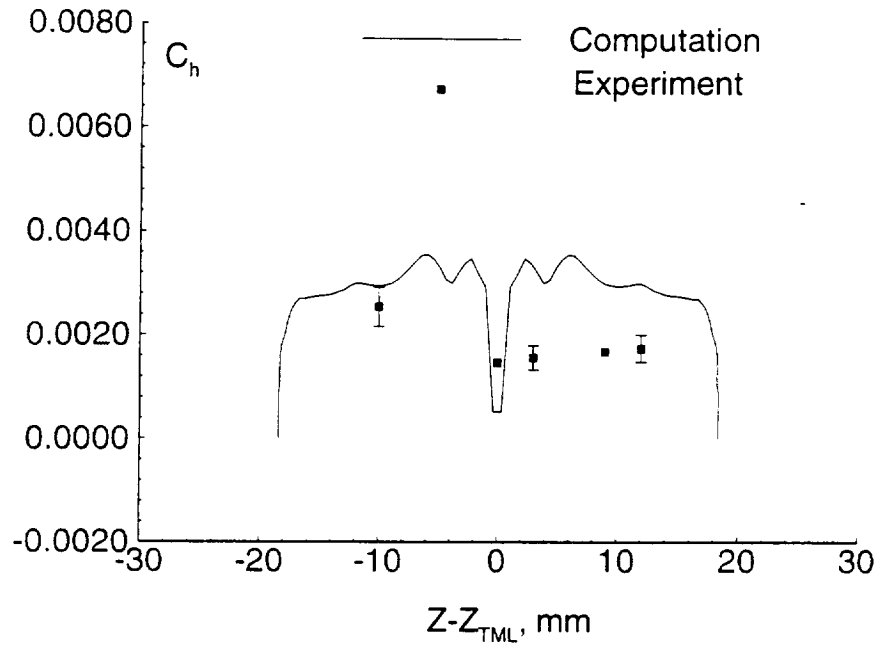
Figure 6.57: Heat transfer at x = 79 mm for $15° \times 15°$
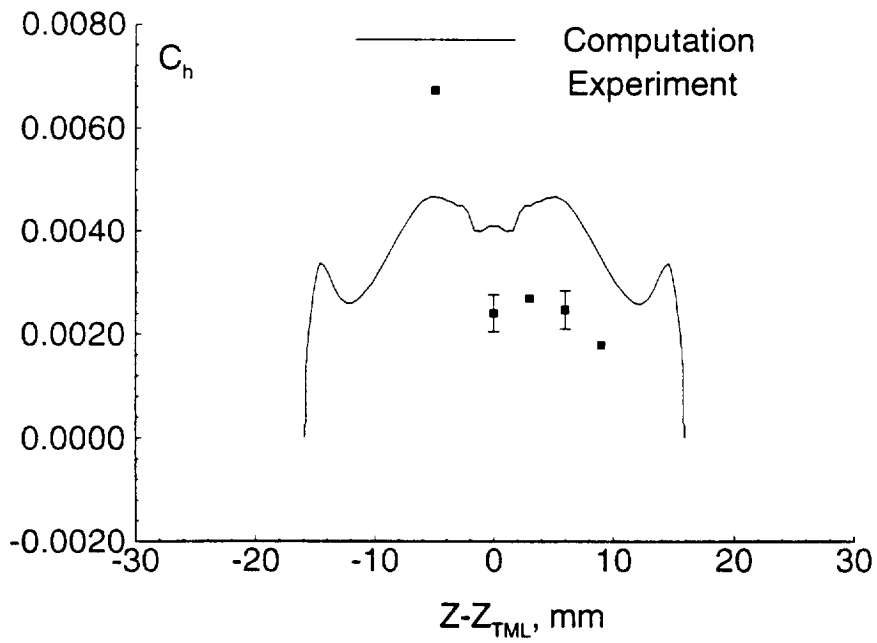
Figure 6.58: Heat transfer at x = 112 mm for $15° \times 15°$
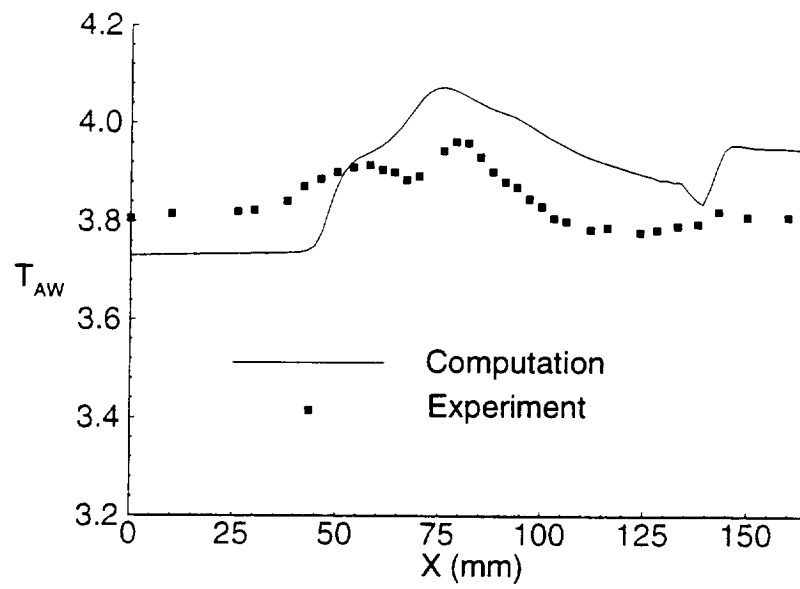
Figure 6.59: Adiabatic wall temperature on TML for $15° \times 15°$
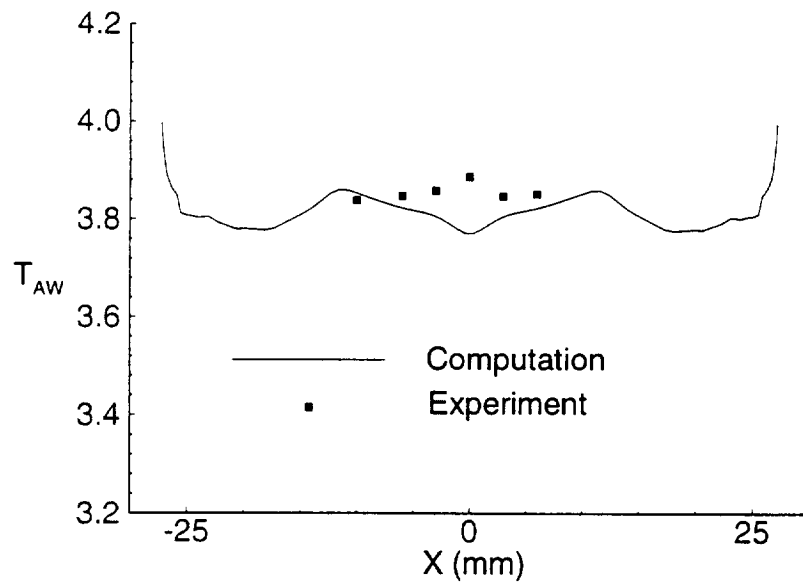
Figure 6.60: Adiabatic wall temperature at $x = 46$ mm for $15° \times 15°$
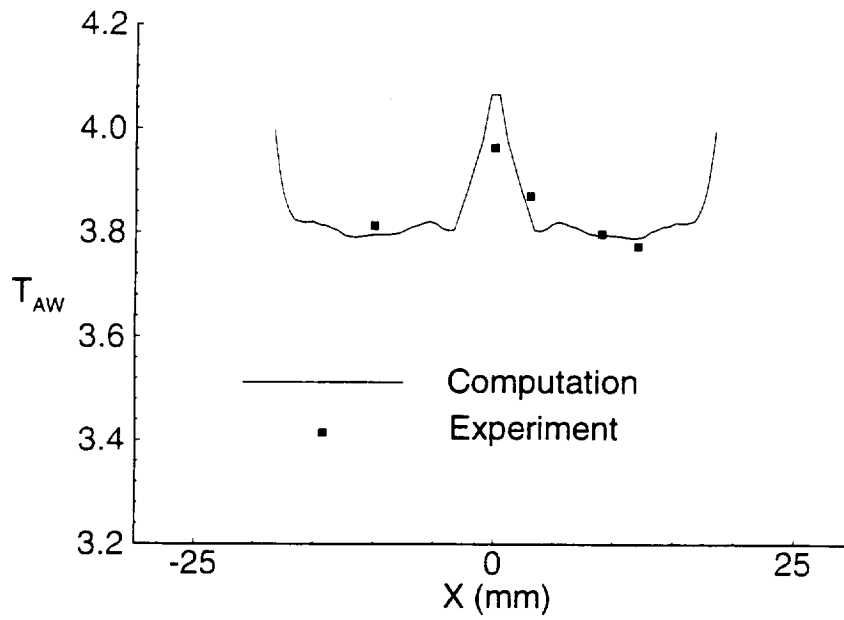
Figure 6.61: Adiabatic wall temperature at $x = 79$ mm for $15° \times 15°$
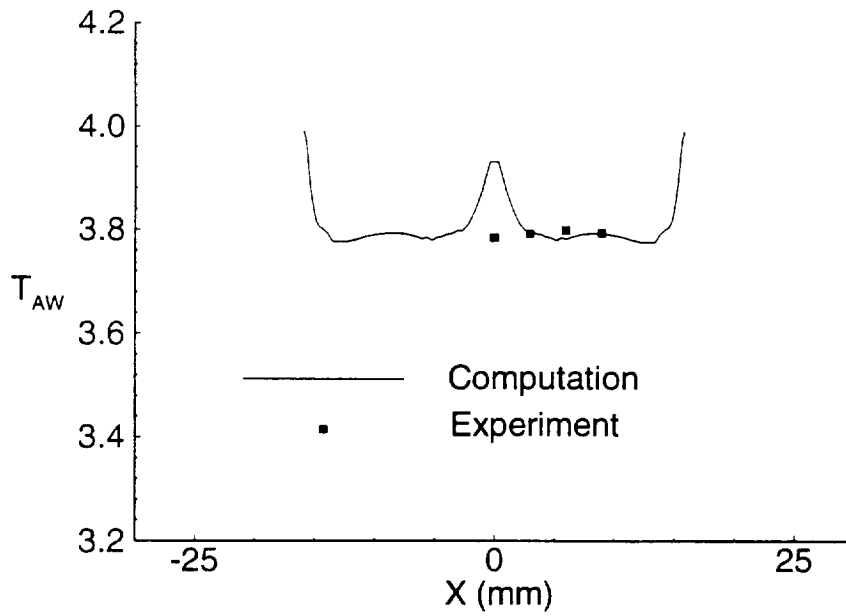
Figure 6.62: Adiabatic wall temperature at $x = 112$ mm for $15° \times 15°$
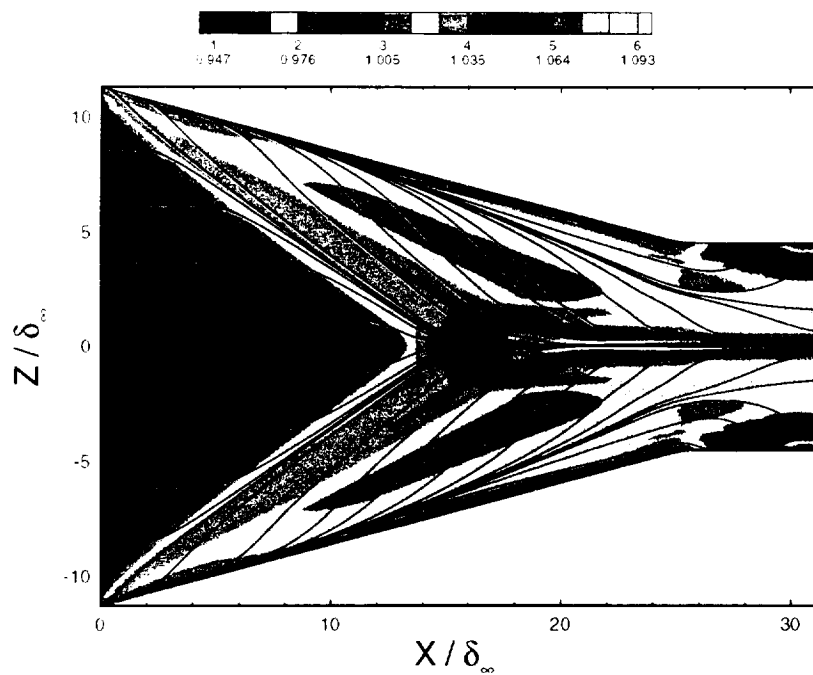
Figure 6.63: Computed adiabatic wall temperature contours at the flat plate surface for $15° \times 15°$
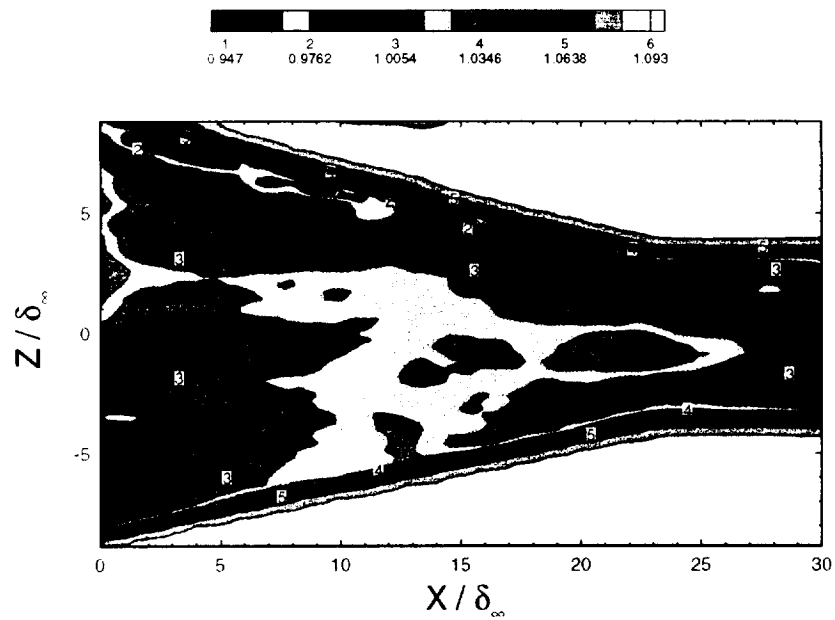
Figure 6.64: Experimental adiabatic wall temperature contours at the flat plate surface for $15° \times 15°$

6.4   Influence of Computational Parameters

6.4.1   Grid Refinement Study

A grid refinement study was performed for the $7° \times 11°$ case in order to investigate the influence of the grid resolution on the results. The grid refinement study was performed by doubling the number of the grid nodes in each direction one at a time. The details of the grids involved in the grid refinement study can be found in the Table 5.2 in the previous chapter (cases 1c, 1d and 1e).

It was found that the pressure distribution on the bottom surface is virtually insensitive to the grid refinement, as it is shown in Fig.6.65. The heat transfer coefficient on the centerline (Fig. 6.66) varies with the grid resolution within 8% in the region downstream of the crossing shock interaction. This value is significantly less than the deviation of computed heat transfer coefficient from the experimental value, and from this point of view the accuracy of the computation is considered sufficient (i.e., the numerical truncation error for the heat transfer coefficient is small compared to the difference between the computed and experimental values in the 3-D interaction region).
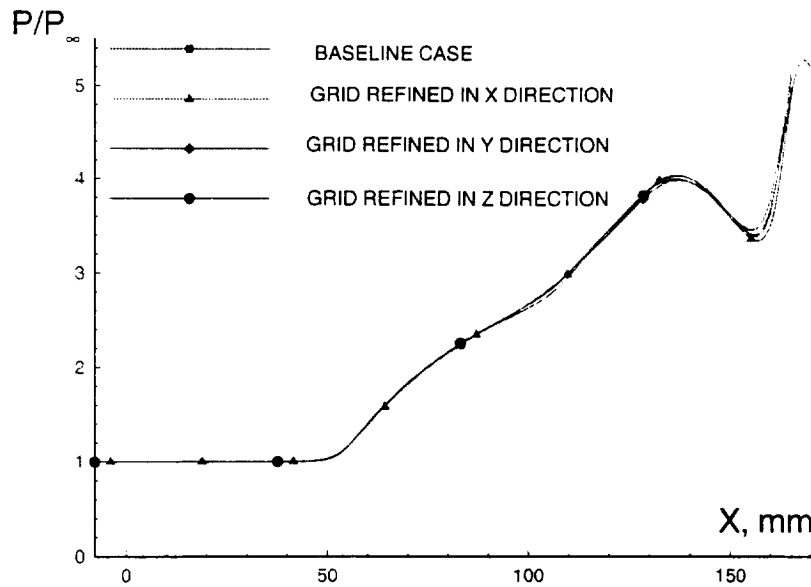
Figure 6.65: Pressure at the centerline for $7° \times 11°$: grid refinement study
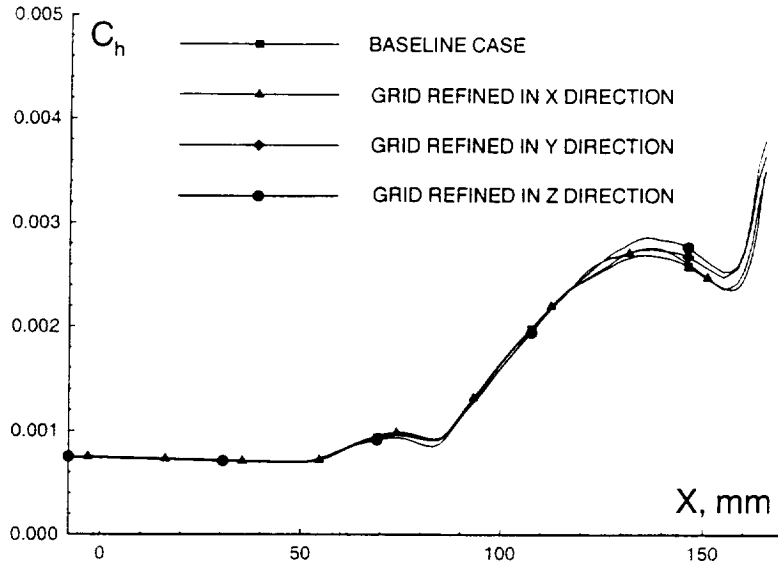
Figure 6.66: Heat transfer coefficient at the centerline:
grid refinement study for $7° \times 11°$

6.4.2 Influence of the Wall Temperature

Separate computation were performed for the $7° \times 11°$ case in order to investigate the influence of the wall temperature on the heat transfer coefficient. As briefly described in the previous chapter, in order to determine the heat transfer coefficient

$$C_h = q_w(x, z) / \{\rho_\infty U_\infty c_p[T_w(x, z) - T_{aw}(x, z)]\}$$

two computations are needed, one with the fixed bottom wall temperature T_w, and another one to determine the adiabatic wall temperature $T_{AW} = T_{AW}(x, z)$. In order to verify the legitimacy of the present approach for computing C_h and to investigate the influence of the choice of T_w on C_h, two computations with two different values of T_w (265K and 270K) were performed.

Figs. 6.67 and 6.68 contain heat transfer distributions along the centerline and at one of the crossections respectively, obtained with two different wall temperatures. The results show that the influence of the choice of wall temperature on the heat transfer coefficient is negligible as expected.
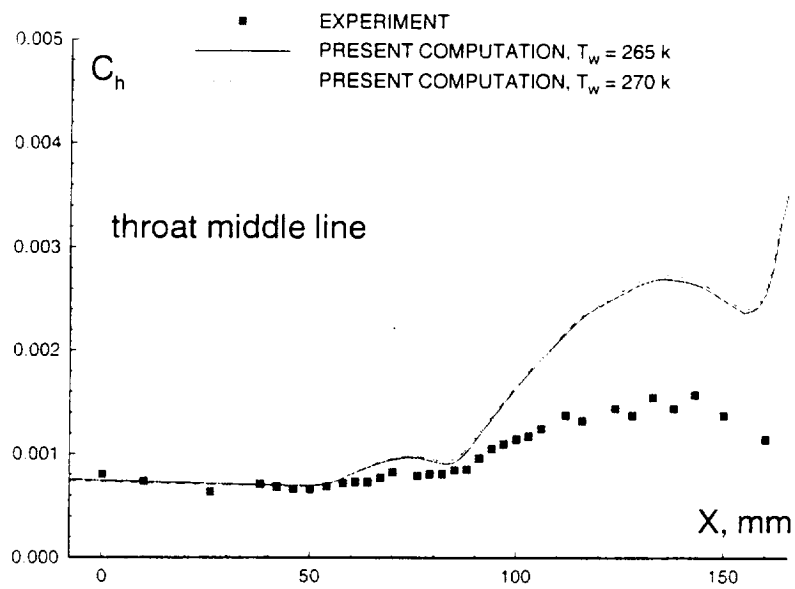
Figure 6.67: Heat transfer coefficient for different T_W at the centerline
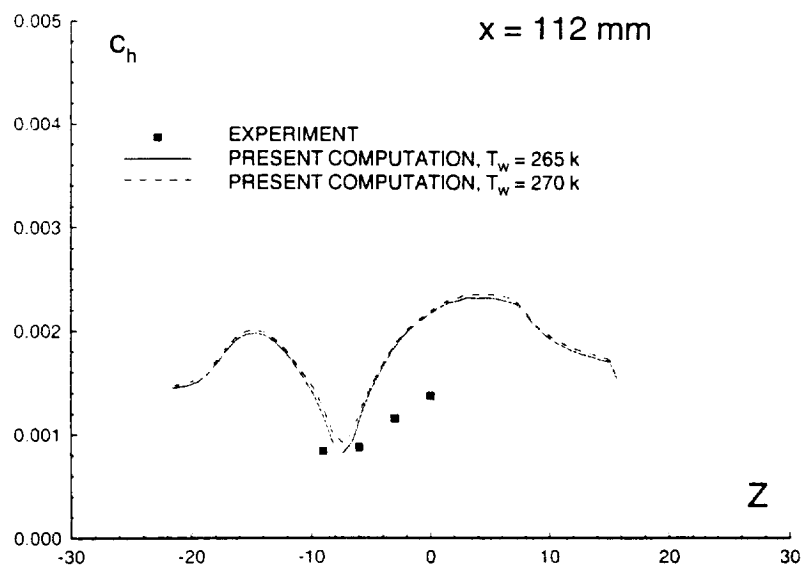
Figure 6.68: Heat transfer coefficient for different T_W at $x=112$mm

Chapter 7

CONCLUSIONS

7.1 Conclusions

A crossing shock wave-turbulent boundary layer interaction has been studied numerically. The shock waves are generated by a pair of fins which are mounted normal to a flat plate and form a converging channel. The focus of the study has been to investigate the ability of the low Reynolds number correction to the "standard" $k - \epsilon$ two equation turbulence model to provide for improvement in the predictions of adiabatic wall temperature and heat transfer rates during the interaction of the shock waves with the turbulent boundary layer on the flat plate. Three configurations with fin angles of $7° \times 11°$, $7° \times 7°$ and $15° \times 15°$ have been examined at Mach 3.95. Experimental data available for comparison includes surface pressure, heat transfer, adiabatic wall temperature and surface flow visualization. The results obtained with this new turbulence model are also compared for the $7° \times 11°$ configuration to the previous computational predictions obtained with the Chien's low Re number correction [24] to the two-equation $k-\epsilon$ model and to the corresponding computations with a full Reynolds stress equation model [61].

Computations employ the 3-D Reynolds-averaged compressible Navier-Stokes equations with turbulence represented by the two equation $k-\epsilon$ model with the low Reynolds number correction of Knight. A series of test computations has been conducted to validate the solver. The grid refinement study was performed and influence of computational parameters was examined.

The principal conclusions are:

- The computed surface pressure displays good agreement with experiment for all

three turbulence models for the $7° \times 11°$ configuration. For the $15° \times 15°$ configuration pressure is overpredicted by 22 % at the centerline in the vicinity of the point of the intersection of the oblique shocks but exhibits good agreement in other regions.

- The computed surface skin friction lines and experimental surface flow visualization display close agreement in the location of the initial separation lines, and are in qualitative agreement within the crossing shock interaction region. However, in a major difference with the Chien's model results for the $7° \times 11°$ configuration, the secondary separation line is not predicted by the present computation due to the difference in computed pressure distribution in the spanwise direction. The secondary separation line is present in the $15° \times 15°$ computation.

- For the $7° \times 11°$ configuration, the computed heat transfer is significantly over-predicted by all three models within the region downstream of the intersection of the λ-shocks generated by the fins. However, a modest improvement is achieved compared to the computations with Chien's model. For the $15° \times 15°$ configuration, the computed heat transfer within the region downstream of the intersection is also significantly overpredicted by the present computation.

- For the $7° \times 7°$ configuration, the computed heat transfer is in a good agreement with the experimental results within the whole computational domain.

- The adiabatic wall temperature is accurately predicted for all considered configurations, except that it is overpredicted by 3% in the vicinity of the centerline in the $15° \times 15°$ case.

7.2 Discussion of the Results of the Validation of the Low Reynolds number correction of Knight

The main objective of the present research was the validation of the low Reynolds number modification of Knight to the standard $k - \epsilon$ model in application to a crossing

shock flow. The model predicts adiabatic wall temperature better, than other considered models. However, the surface heat transfer downstream of the interaction of the shocks is still overpredicted by the present model for the $7° \times 11°$ and $15° \times 15°$ configurations. The results with the current model exhibit a modest improvement compared to the Chien's model results, however, the difference is small compared to the deviation with experiment. Even the full Reynolds stress equation model, which is considerably more complex and takes better account of the flow physics, does not provide for essential improvement in the prediction of the wall heat transfer rate. In the $7° \times 7°$ case computations are in reasonable agreement with experiment for all variables including surface heat transfer.

In summary, all three considered turbulence models overpredict C_h downstream of the interaction. The reason for that is not clear and further research is needed. Several explanations could be suggested. The first possible explanation, suggested by Dr. A.A. Zheltovodov, is the partial relaminarization of the flow under the influence of the favorable crossflow pressure gradient, which can cause a decline in the value of the heat transfer coefficient in the $7° \times 11°$ case. The regions of favorable pressure gradient are evident in Fig. 6.4, where surface streamlines are colored according to static pressure. The second possible reason is that all three considered models have a build-in assumption of the presure gradient being small, which is not the case in the present computation. The current model was tested in [6] for a 2-D boundary layer flow with adverse pressure gradient. Results showed close agreement with experimental velocity and Mach number and disagreement for the surface skin friction and Reynolds shear stress. The $k - \epsilon$ model is known to perform worse in the presense of a strong adverse pressure gradient and separation [55]. The third possibility is a nonadequate resolution of the secondary structures, located underneath of the main separation region, at least in the $15° \times 15°$ case.

7.3 Future Work

Substantial research efforts have been invested into studying shock wave-turbulent boundary layer interactions, in particular, crossing shock interaction. However, a complete understanding of the flow physics has not been achieved so far and further research is needed.

In the field of experimental investigation of crossing shock interaction flows substantially more detailed experimental measurements for asymmetric cases are needed in order to provide for further insights into the problem and to validate computational results and different turbulence models. In particular, more measurements of main flowfield and wave structure as well as of turbulence statistics, wall heat flux and shear stress are needed.

In the field of numerical investigation of crossing chock flows a significant improvement can be achieved by utilizing adaptive grids. Crossing shock flows usually manifest a complex wave structure, especially within boundary layer, with some of the waves being weak, and no possibility exists to predict the wave structure a priori (except for main "inviscid" shocks). Consequently, better predictions could be obtained with adaptive grids, both structured and unstructured.

Appendix A

Jacobian Matrices

Explicit form of the Jacobian matrices is presented in this appendix. The matrices are obtained analytically in [22] by rewriting the flux vectors in terms of conservative variables and differentiating each flux with respect to each conservative variable.

The Jacobian matrices A, B and C obtained by differentiating inviscid fluxes with respect to conservative variables, are :

$$A = \begin{pmatrix}
0 & l_x & l_y & l_z & 0 & 0 & 0 \\
-uU + l_x(\gamma-1)\mathcal{K} & U + l_x(2-\gamma)u & ul_y - l_x(\gamma-1)v & ul_z - l_x(\gamma-1)w & l_x(\gamma-1) & -l_x(\gamma-1) & 0 \\
-vU + l_y(\gamma-1)\mathcal{K} & vl_x - l_y(\gamma-1)u & U + l_y(2-\gamma)v & vl_z - l_y(\gamma-1)w & l_y(\gamma-1) & -l_y(\gamma-1) & 0 \\
-wU + l_z(\gamma-1)\mathcal{K} & wl_x - l_z(\gamma-1)U & wl_y - l_z(\gamma-1)V & U + l_z(2-\gamma)w & l_z(\gamma-1) & -l_z(\gamma-1) & 0 \\
U[-\gamma e + 2(\gamma-1)\mathcal{K}] & -(\gamma-1)Uu + l_x\mathcal{M} & -(\gamma-1)Uv + l_y\mathcal{M} & -(\gamma-1)Uw + l_z\mathcal{M} & \gamma U & -(\gamma-1)U & 0 \\
-Uk & l_xk & l_yk & l_zk & 0 & U & 0 \\
-U\epsilon & l_x\epsilon & l_y\epsilon & l_x\epsilon & 0 & 0 & U
\end{pmatrix} \quad (A.1)$$

$$B = \begin{pmatrix}
0 & m_x & m_y & m_z & 0 & 0 & 0 \\
-uV + m_x(\gamma-1)\mathcal{K} & V + m_x(2-\gamma)u & um_y - m_x(\gamma-1)v & um_z - m_x(\gamma-1)w & m_x(\gamma-1) & -m_x(\gamma-1) & 0 \\
-vV + m_y(\gamma-1)\mathcal{K} & vm_x - m_y(\gamma-1)u & V + m_y(2-\gamma)v & vm_z - m_y(\gamma-1)w & m_y(\gamma-1) & -m_y(\gamma-1) & 0 \\
-wV + m_z(\gamma-1)\mathcal{K} & wm_x - m_z(\gamma-1)V & wm_y - m_z(\gamma-1)V & V + m_z(2-\gamma)w & m_z(\gamma-1) & -m_z(\gamma-1) & 0 \\
V[-\gamma e + 2(\gamma-1)\mathcal{K}] & -(\gamma-1)Vu + m_x\mathcal{M} & -(\gamma-1)Vv + m_y\mathcal{M} & -(\gamma-1)Vw + m_z\mathcal{M} & \gamma V & -(\gamma-1)V & 0 \\
-Vk & m_xk & m_yk & m_zk & 0 & V & 0 \\
-V\epsilon & m_x\epsilon & m_y\epsilon & m_z\epsilon & 0 & 0 & V
\end{pmatrix} \quad (A.2)$$

$$C = \begin{pmatrix}
0 & m_x & m_y & m_z & 0 & 0 & 0 \\
-uW + n_x(\gamma-1)\mathcal{K} & W + n_x(2-\gamma)u & uny - n_x(\gamma-1)v & un_z - n_x(\gamma-1)w & n_x(\gamma-1) & -n_x(\gamma-1) & 0 \\
-vW + ny(\gamma-1)\mathcal{K} & vn_x - ny(\gamma-1)u & W + ny(2-\gamma)v & vn_z - ny(\gamma-1)w & ny(\gamma-1) & -ny(\gamma-1) & 0 \\
-wW + n_z(\gamma-1)\mathcal{K} & wn_x - n_z(\gamma-1)W & wny - n_z(\gamma-1)W & W + n_z(2-\gamma)w & n_z(\gamma-1) & -n_z(\gamma-1) & 0 \\
W[-\gamma e + 2(\gamma-1)\mathcal{K}] & -(\gamma-1)Wu + n_x\mathcal{M} & -(\gamma-1)Wv + ny\mathcal{M} & -(\gamma-1)Ww + n_z\mathcal{M} & \gamma W & -(\gamma-1)W & 0 \\
-Wk & n_xk & nyk & n_zk & 0 & W & 0 \\
-W\epsilon & n_x\epsilon & ny\epsilon & n_z\epsilon & 0 & 0 & W
\end{pmatrix} \quad (A.3)$$

where $\mathcal{M} = [\gamma e - (\gamma - 1)\mathcal{K}]$, $\mathcal{K} = \frac{u^2 + v^2 + w^2}{2}$, $U = l_x u + l_y v + l_z w$, $V = m_x u + m_y v + m_z w$, and $W = n_x u + n_y v + n_z w$.

The Jacobians are evaluated at the cell faces using the conservative variables in the neighboring cells.

The Jacobian matrices L, M and N obtained by differentiating viscous fluxes with respect to conservative variables, are presented below.

$$L^L_{i+\frac{1}{2}} = \begin{pmatrix} 0 & 0 & 0 & 0 & 0 & 0 & 0 \\ \alpha_{i+\frac{1}{2}}\frac{[c_1 u_i + c_4 v_i + c_7 w_i]}{\rho_i} & -\alpha_{i+\frac{1}{2}}\frac{c_1}{\rho_i} & -\alpha_{i+\frac{1}{2}}\frac{c_4}{\rho_i} & -\alpha_{i+\frac{1}{2}}\frac{c_7}{\rho_i} & 0 & 0 & 0 \\ \alpha_{i+\frac{1}{2}}\frac{[c_4 u_i + c_{12} v_i + c_{15} w_i]}{\rho_i} & -\alpha_{i+\frac{1}{2}}\frac{c_4}{\rho_i} & -\alpha_{i+\frac{1}{2}}\frac{c_{12}}{\rho_i} & -\alpha_{i+\frac{1}{2}}\frac{c_{15}}{\rho_i} & 0 & 0 & 0 \\ \alpha_{i+\frac{1}{2}}\frac{[c_7 u_i + c_{15} v_i + c_{22} w_i]}{\rho_i} & -\alpha_{i+\frac{1}{2}}\frac{c_7}{\rho_i} & -\alpha_{i+\frac{1}{2}}\frac{c_{15}}{\rho_i} & -\alpha_{i+\frac{1}{2}}\frac{c_{22}}{\rho_i} & 0 & 0 & 0 \\ l_{5.1} & l_{5.2} & l_{5.3} & l_{5.4} & -c_{25}\alpha_Q\frac{\partial T}{\partial \rho e}\big|_i & -c_{25}\alpha_Q\frac{\partial T}{\partial \rho k}\big|_i & 0 \\ c_{25}\alpha_k\frac{k_i}{\rho_i} + \left(\rho k\big|_{i+1} - \rho k\big|_i\right)\frac{\partial \beta_k}{\partial \rho} & 0 & 0 & 0 & 0 & -c_{25}\left(\alpha_k\frac{1}{\rho_i} + \beta_k\right) & 0 \\ c_{25}\alpha_\epsilon\frac{\epsilon_i}{\rho_i} & 0 & 0 & 0 & 0 & 0 & -c_{25}\alpha_\epsilon\frac{1}{\rho_i} \end{pmatrix}$$ (A.4)

Here

$$L^L_{i+\frac{1}{2}} \equiv \frac{\partial R_{i+\frac{1}{2}}}{\partial Q_i}$$

$$l_{5.1} = -c_{25}\alpha_Q\frac{\partial T}{\partial \rho}\big|_i + \alpha_{i+\frac{1}{2}}\left[c_1\frac{u_i^2}{\rho_i} + c_{12}\frac{v_i^2}{\rho_i} + c_{22}\frac{w_i^2}{\rho_i} + 2c_4\frac{u_i v_i}{\rho_i} + 2c_7\frac{u_i w_i}{\rho_i} + 2c_{15}\frac{v_i w_i}{\rho_i}\right]$$

$$l_{5.2} = -c_{25}\alpha_Q\frac{\partial T}{\partial \rho u}\big|_i + \alpha_{i+\frac{1}{2}}\left[-c_1\frac{u_i}{\rho_i} - c_4\frac{v_i}{\rho_i} - c_7\frac{w_i}{\rho_i}\right]$$

$$l_{5.3} = -c_{25}\alpha_Q\frac{\partial T}{\partial \rho v}\big|_i + \alpha_{i+\frac{1}{2}}\left[-c_{12}\frac{v_i}{\rho_i} - c_4\frac{u_i}{\rho_i} - c_{15}\frac{w_i}{\rho_i}\right]$$

$$l_{5.4} = -c_{25}\alpha_Q\frac{\partial T}{\partial \rho w}\big|_i + \alpha_{i+\frac{1}{2}}\left[-c_{22}\frac{w_i}{\rho_i} - c_7\frac{u_i}{\rho_i} - c_{15}\frac{v_i}{\rho_i}\right]$$

$$\frac{\partial T}{\partial \rho} = \gamma(\gamma - 1)M_\infty^2\left[-\frac{e}{\rho} + \frac{u^2 + v^2 + w^2}{\rho} + \frac{k}{\rho}\right]$$

$$\frac{\partial T}{\partial \rho u} = -\gamma(\gamma - 1)M_\infty^2\frac{u}{\rho}$$

$$\frac{\partial T}{\partial \rho v} = -\gamma(\gamma - 1)M_\infty^2\frac{v}{\rho}$$

$$\frac{\partial T}{\partial \rho w} = -\gamma(\gamma - 1)M_\infty^2\frac{w}{\rho}$$

$$\frac{\partial T}{\partial \rho e} = \gamma (\gamma - 1) M_\infty^2 \frac{1}{\rho}$$

$$\frac{\partial T}{\partial \rho k} = -\gamma (\gamma - 1) M_\infty^2 \frac{1}{\rho} \qquad (A.5)$$

The diffusion coefficients are defined as

$$\alpha_{i+\frac{1}{2}} = \frac{1}{2} \frac{1}{\text{Re}} \left\{ \frac{(\mu + \mu_t)}{\nu} |_{i+1} + \frac{(\mu + \mu_t)}{\nu} |_i \right\}$$

$$\alpha_{Q\, i+\frac{1}{2}} = \frac{1}{(\gamma - 1) M_\infty^2} \frac{1}{\text{Re}} \frac{1}{2} \left\{ \left(\frac{\mu_t}{Pr_t \nu} \right) |_{i+1} + \left(\frac{\mu_t}{Pr_t \nu} \right) |_i \right\}$$

$$\alpha_{\epsilon\, i+\frac{1}{2}} = \frac{1}{\text{Re}} \frac{1}{2} \left\{ \left(\frac{\left(\mu + \frac{\mu_t}{\sigma_\epsilon} \right)}{\nu} \right) |_{i+1} + \left(\frac{\left(\mu + \frac{\mu_t}{\sigma_\epsilon} \right)}{\nu} \right) |_i \right\}$$

$$\alpha_{k\, i+\frac{1}{2}} = \frac{1}{\text{Re}} \frac{1}{2} \left\{ \left(\frac{\mu}{\nu} \right) |_{i+1} + \left(\frac{\mu}{\nu} \right) |_i \right\}$$

$$\beta_{k\, i+\frac{1}{2}} = \frac{1}{\text{Re}} \frac{1}{2} \left\{ \left(\frac{\mu_t}{\rho \sigma_k \nu} \right) |_{i+1} + \left(\frac{\mu_t}{\rho \sigma_k \nu} \right) |_i \right\}$$

$$\frac{\partial \beta_{k\, i+\frac{1}{2}}}{\partial \rho} = -\frac{1}{\text{Re}} \frac{1}{2} \left(\frac{\mu_t}{\rho^2 \sigma_k \nu} \right) \qquad (A.6)$$

$$
_{+\frac{1}{2}} = \begin{pmatrix}
0 & 0 & 0 & 0 & 0 & 0 & 0 \\
-\alpha_{i+\frac{1}{2}} \frac{[c_1 u_{i+1} + c_4 v_{i+1} + c_7 w_{i+1}]}{\rho_{i+1}} & \alpha_{i+\frac{1}{2}} \frac{c_1}{\rho_{i+1}} & \alpha_{i+\frac{1}{2}} \frac{c_4}{\rho_{i+1}} & \alpha_{i+\frac{1}{2}} \frac{c_7}{\rho_{i+1}} & 0 & 0 & 0 \\
-\alpha_{i+\frac{1}{2}} \frac{[c_4 u_{i+1} + c_{12} v_{i+1} + c_{15} w_{i+1}]}{\rho_{i+1}} & \alpha_{i+\frac{1}{2}} \frac{c_4}{\rho_{i+1}} & \alpha_{i+\frac{1}{2}} \frac{c_{12}}{\rho_{i+1}} & \alpha_{i+\frac{1}{2}} \frac{c_{15}}{\rho_{i+1}} & 0 & 0 & 0 \\
-\alpha_{i+\frac{1}{2}} \frac{[c_7 u_{i+1} + c_{15} v_{i+1} + c_{22} w_{i+1}]}{\rho_{i+1}} & \alpha_{i+\frac{1}{2}} \frac{c_7}{\rho_{i+1}} & \alpha_{i+\frac{1}{2}} \frac{c_{15}}{\rho_{i+1}} & \alpha_{i+\frac{1}{2}} \frac{c_{22}}{\rho_{i+1}} & 0 & 0 & 0 \\
l_{5,1} & l_{5,2} & l_{5,3} & l_{5,4} & c_{25} \alpha_Q \frac{\partial T}{\partial \rho e} |_{i+1} & c_{25} \alpha_Q \frac{\partial T}{\partial \rho k} |_{i+1} & 0 \\
-c_{25} \alpha_k \frac{k_{i+1}}{\rho_{i+1}} + \left(\rho k |_{i+1} + \rho k |_{i+1} \right) \frac{\partial \beta_k}{\partial \rho} & 0 & 0 & 0 & 0 & c_{25} \left(\alpha_k \frac{1}{\rho_{i+1}} + \beta_k \right) & 0 \\
-c_{25} \alpha_\epsilon \frac{\epsilon_{i+1}}{\rho_{i+1}} & 0 & 0 & 0 & 0 & 0 & c_{25} \alpha_\epsilon \frac{1}{\rho_{i+1}}
\end{pmatrix} \qquad (A.7)
$$

Here

$$L^R_{i+\frac{1}{2}} \equiv \frac{\partial R_{i+\frac{1}{2}}}{\partial Q_{i+1}}$$

$$l_{5,1} = c_{25} \alpha_Q \frac{\partial T}{\partial \rho} |_{i+1} - \alpha_{i+\frac{1}{2}} \left[c_1 \frac{u_{i+1}^2}{\rho_{i+1}} + c_{12} \frac{v_{i+1}^2}{\rho_{i+1}} + c_{22} \frac{w_{i+1}^2}{\rho_{i+1}} \right.$$

$$\left. + 2 c_4 \frac{u_{i+1} v_{i+1}}{\rho_{i+1}} + 2 c_7 \frac{u_{i+1} w_{i+1}}{\rho_{i+1}} + 2 c_{15} \frac{v_{i+1} w_{i+1}}{\rho_{i+1}} \right]$$

$$l_{5,2} = c_{25} \alpha_Q \frac{\partial T}{\partial \rho u} |_{i+1} + \alpha_{i+\frac{1}{2}} \left[c_1 \frac{u_{i+1}}{\rho_{i+1}} + c_4 \frac{v_{i+1}}{\rho_{i+1}} + c_7 \frac{w_{i+1}}{\rho_{i+1}} \right]$$

Here

$$
M^L_{j+\frac{1}{2}} =
\begin{pmatrix}
0 & 0 & 0 & 0 & 0 \\
\alpha_{j+\frac{1}{2}} \frac{b_2}{\rho_j} & -\alpha_{j+\frac{1}{2}} \frac{b_2}{\rho_j} & 0 & 0 & 0 \\
\alpha_{j+\frac{1}{2}} \frac{\rho_j}{\rho_j} & -\alpha_{j+\frac{1}{2}} \frac{b_5}{\rho_j} & -\alpha_{j+\frac{1}{2}} \frac{b_6}{\rho_j} & 0 & 0 \\
\alpha_{j+\frac{1}{2}} \frac{b_{8}u_j+b_{16}v_j+b_{23}w_j}{\rho_j} & -\alpha_{j+\frac{1}{2}} \frac{b_8}{\rho_j} & -\alpha_{j+\frac{1}{2}} \frac{b_{16}}{\rho_j} & -\alpha_{j+\frac{1}{2}} \frac{b_{23}}{\rho_j} & 0 \\
b_{25}\alpha\frac{k_j}{\rho_j}+(\rho k|_{j+1}-\rho k|_j)\frac{\partial b_k}{\partial\rho} & m_{5,1} & m_{5,2} & m_{5,3} & m_{5,4} \\
b_{25}\alpha_c\frac{c_j}{\rho_j} & & & & \\
\end{pmatrix}
$$
(matrix abbreviated)

$$M^L_{j+\frac{1}{2}} \equiv \frac{\partial S_{j+\frac{1}{2}}}{\partial Q_j}$$

The diffusion coefficients are defined as

$$\alpha_{j+\frac{1}{2}} = \frac{1}{2}\frac{1}{Re}\left\{\frac{(\mu+\mu_t)}{\nu}\Big|_{j+1}+\frac{(\mu+\mu_t)}{\nu}\Big|_j\right\}$$

$$\alpha_{Qj+\frac{1}{2}} = \frac{1}{(\gamma-1)M_\infty^2}\frac{1}{Re}\frac{1}{2}\left\{\left(\frac{\mu}{Pr_t\nu}+\frac{\mu_t}{Pr_t\nu}\right)\Big|_{j+1}+\left(\frac{\mu}{Pr_t\nu}+\frac{\mu_t}{Pr_t\nu}\right)\Big|_j\right\}$$

$$\alpha_{ej+\frac{1}{2}} = \frac{1}{Re}\frac{1}{2}\left\{\left(\frac{\mu+\frac{\mu_t}{\sigma_c}}{\nu}\right)\Big|_{j+1}+\left(\frac{\mu+\frac{\mu_t}{\sigma_c}}{\nu}\right)\Big|_j\right\}$$

$$\alpha_{kj+\frac{1}{2}} = \frac{1}{Re}\frac{1}{2}\left\{\left(\frac{\mu}{\nu}\right)\Big|_{j+1}+\left(\frac{\mu}{\nu}\right)\Big|_j\right\}$$

$$\beta_{k\,j+\frac{1}{2}} = \frac{1}{Re}\frac{1}{2}\left\{\left(\frac{\mu_t}{\rho\sigma_k\nu}\right)\big|_{j+1} + \left(\frac{\mu_t}{\rho\sigma_k\nu}\right)\big|_j\right\}$$

$$\frac{\partial\beta_{k\,j+\frac{1}{2}}}{\partial\rho} = -\frac{1}{Re}\frac{1}{2}\left(\frac{\mu_t}{\rho^2\sigma_k\nu}\right) \tag{A.9}$$

$$
R_{j+\frac{1}{2}} = \begin{pmatrix}
0 & 0 & 0 & 0 & 0 & 0 & 0 \\
-\alpha_{j+\frac{1}{2}}\frac{[b_2u_{j+1}+b_5v_{j+1}+b_8w_{j+1}]}{\rho_{j+1}} & \alpha_{j+\frac{1}{2}}\frac{b_2}{\rho_{j+1}} & \alpha_{j+\frac{1}{2}}\frac{b_5}{\rho_{j+1}} & \alpha_{j+\frac{1}{2}}\frac{b_8}{\rho_{j+1}} & 0 & 0 & 0 \\
-\alpha_{j+\frac{1}{2}}\frac{[b_5u_{j+1}+b_{13}v_{j+1}+b_{16}w_{j+1}]}{\rho_{j+1}} & \alpha_{j+\frac{1}{2}}\frac{b_5}{\rho_{j+1}} & \alpha_{j+\frac{1}{2}}\frac{b_{13}}{\rho_{j+1}} & \alpha_{j+\frac{1}{2}}\frac{b_{16}}{\rho_{j+1}} & 0 & 0 & 0 \\
-\alpha_{j+\frac{1}{2}}\frac{[b_8u_{j+1}+b_{16}v_{j+1}+b_{23}w_{j+1}]}{\rho_{j+1}} & \alpha_{j+\frac{1}{2}}\frac{b_8}{\rho_{j+1}} & \alpha_{j+\frac{1}{2}}\frac{b_{16}}{\rho_{j+1}} & \alpha_{j+\frac{1}{2}}\frac{b_{23}}{\rho_{j+1}} & 0 & 0 & 0 \\
m_{5,1} & m_{5,2} & m_{5,3} & m_{5,4} & b_{25}\alpha_Q\frac{\partial T}{\partial\rho e}\big|_{j+1} & b_{25}\alpha_Q\frac{\partial T}{\partial\rho k}\big|_{j+1} & 0 \\
-b_{25}\alpha_k\frac{k_{j+1}}{\rho_{j+1}}+\left(\rho k\big|_{j+1}+\rho k\big|_{j+1}\right)\frac{\partial\beta_k}{\partial\rho} & 0 & 0 & 0 & 0 & b_{25}\left(\alpha_k\frac{1}{\rho_{j+1}}+\beta_k\right) & 0 \\
-b_{25}\alpha_\epsilon\frac{\epsilon_{j+1}}{\rho_{j+1}} & 0 & 0 & 0 & 0 & 0 & b_{25}\alpha_\epsilon\frac{1}{\rho_{j+1}}
\end{pmatrix} \tag{A.10}
$$

Here

$$M^R_{j+\frac{1}{2}} \equiv \frac{\partial S_{j+\frac{1}{2}}}{\partial Q_{j+1}}$$

$$m_{5,1} = b_{25}\alpha_Q\frac{\partial T}{\partial\rho}\big|_{j+1} - \alpha_{j+\frac{1}{2}}\left[b_2\frac{u^2_{j+1}}{\rho_{j+1}}+b_{13}\frac{v^2_{j+1}}{\rho_{j+1}}+b_{23}\frac{w^2_{j+1}}{\rho_{j+1}}\right.$$
$$\left.+2b_5\frac{u_{j+1}v_{j+1}}{\rho_{j+1}}+2b_8\frac{u_{j+1}w_{j+1}}{\rho_{j+1}}+2b_{16}\frac{v_{j+1}w_{j+1}}{\rho_{j+1}}\right]$$

$$m_{5,2} = b_{25}\alpha_Q\frac{\partial T}{\partial\rho u}\big|_{j+1} + \alpha_{j+\frac{1}{2}}\left[b_2\frac{u_{j+1}}{\rho_{j+1}}+b_5\frac{v_{j+1}}{\rho_{j+1}}+b_8\frac{w_{j+1}}{\rho_{j+1}}\right]$$

$$m_{5,3} = b_{25}\alpha_Q\frac{\partial T}{\partial\rho v}\big|_{j+1} + \alpha_{j+\frac{1}{2}}\left[b_{13}\frac{v_{j+1}}{\rho_{j+1}}+b_5\frac{u_{j+1}}{\rho_{j+1}}+b_{16}\frac{w_{j+1}}{\rho_{j+1}}\right]$$

$$m_{5,4} = b_{25}\alpha_Q\frac{\partial T}{\partial\rho w}\big|_{j+1} + \alpha_{j+\frac{1}{2}}\left[b_{23}\frac{w_{j+1}}{\rho_{j+1}}+b_8\frac{u_{j+1}}{\rho_{j+1}}+b_{16}\frac{v_{j+1}}{\rho_{j+1}}\right]$$

$$
N^L_{k+\frac{1}{2}} = \begin{pmatrix}
0 & 0 & 0 & 0 & 0 & 0 & 0 \\
\alpha_{k+\frac{1}{2}}\frac{[d_3u_k+d_6v_k+d_9w_k]}{\rho_k} & -\alpha_{k+\frac{1}{2}}\frac{d_3}{\rho_k} & -\alpha_{k+\frac{1}{2}}\frac{d_6}{\rho_k} & -\alpha_{k+\frac{1}{2}}\frac{d_9}{\rho_k} & 0 & 0 & 0 \\
\alpha_{k+\frac{1}{2}}\frac{[d_6u_k+d_{14}v_k+d_{17}w_k]}{\rho_k} & -\alpha_{k+\frac{1}{2}}\frac{d_6}{\rho_k} & -\alpha_{k+\frac{1}{2}}\frac{d_{14}}{\rho_k} & -\alpha_{k+\frac{1}{2}}\frac{d_{17}}{\rho_k} & 0 & 0 & 0 \\
\alpha_{k+\frac{1}{2}}\frac{[d_9u_k+d_{17}v_k+d_{24}w_k]}{\rho_k} & -\alpha_{k+\frac{1}{2}}\frac{d_9}{\rho_k} & -\alpha_{k+\frac{1}{2}}\frac{d_{17}}{\rho_k} & -\alpha_{k+\frac{1}{2}}\frac{d_{24}}{\rho_k} & 0 & 0 & 0 \\
n_{5,1} & n_{5,2} & n_{5,3} & n_{5,4} & -d_{25}\alpha_Q\frac{\partial T}{\partial\rho e}\big|_k & -d_{25}\alpha_Q\frac{\partial T}{\partial\rho k}\big|_k & 0 \\
d_{25}\alpha_k\frac{k_k}{\rho_k}+\left(\rho k\big|_{k+1}-\rho k\big|_k\right)\frac{\partial\beta_k}{\partial\rho} & 0 & 0 & 0 & 0 & -d_{25}\left(\alpha_k\frac{1}{\rho_k}+\beta_k\right) & 0 \\
d_{25}\alpha_\epsilon\frac{\epsilon_k}{\rho_k} & 0 & 0 & 0 & 0 & 0 & -d_{25}\alpha_\epsilon\frac{1}{\rho_k}
\end{pmatrix} \tag{A.11}
$$

Here

$$N^L_{k+\frac{1}{2}} \equiv \frac{\partial T_{k+\frac{1}{2}}}{\partial Q_k}$$

$$n_{5,1} = -d_{25}\alpha_Q \frac{\partial T}{\partial \rho}\Big|_k + \alpha_{k+\frac{1}{2}}\left[d_3\frac{u_k^2}{\rho_k} + d_{14}\frac{v_k^2}{\rho_k} + d_{24}\frac{w_k^2}{\rho_k} + 2d_6\frac{u_k v_k}{\rho_k} + 2d_9\frac{u_k w_k}{\rho_k} + 2d_{17}\frac{v_k w_k}{\rho_k}\right]$$

$$n_{5,2} = -d_{25}\alpha_Q \frac{\partial T}{\partial \rho u}\Big|_k + \alpha_{k+\frac{1}{2}}\left[-d_3\frac{u_k}{\rho_k} - d_6\frac{v_k}{\rho_k} - d_9\frac{w_k}{\rho_k}\right]$$

$$n_{5,3} = -d_{25}\alpha_Q \frac{\partial T}{\partial \rho v}\Big|_k + \alpha_{k+\frac{1}{2}}\left[-d_{14}\frac{v_k}{\rho_k} - d_6\frac{u_k}{\rho_k} - d_{17}\frac{w_k}{\rho_k}\right]$$

$$n_{5,4} = -d_{25}\alpha_Q \frac{\partial T}{\partial \rho w}\Big|_k + \alpha_{k+\frac{1}{2}}\left[-d_{24}\frac{w_k}{\rho_k} - d_9\frac{u_k}{\rho_k} - d_{17}\frac{v_k}{\rho_k}\right]$$

The diffusion coefficients are defined as

$$\alpha_{k+\frac{1}{2}} = \frac{1}{2}\frac{1}{Re}\left\{\frac{(\mu+\mu_t)}{\nu}\Big|_{k+1} + \frac{(\mu+\mu_t)}{\nu}\Big|_k\right\}$$

$$\alpha_{Q\,k+\frac{1}{2}} = \frac{1}{(\gamma-1)M_\infty^2}\frac{1}{Re}\frac{1}{2}\left\{\left(\frac{\mu_t}{Pr_t\nu}\right)\Big|_{k+1} + \left(\frac{\mu_t}{Pr_t\nu}\right)\Big|_k\right\}$$

$$\alpha_{\epsilon\,k+\frac{1}{2}} = \frac{1}{Re}\frac{1}{2}\left\{\left(\frac{\left(\mu+\frac{\mu_t}{\sigma_\epsilon}\right)}{\nu}\right)\Big|_{k+1} + \left(\frac{\left(\mu+\frac{\mu_t}{\sigma_\epsilon}\right)}{\nu}\right)\Big|_k\right\}$$

$$\alpha_{k\,k+\frac{1}{2}} = \frac{1}{Re}\frac{1}{2}\left\{\left(\frac{\mu}{\nu}\right)\Big|_{k+1} + \left(\frac{\mu}{\nu}\right)\Big|_k\right\}$$

$$\beta_{k\,k+\frac{1}{2}} = \frac{1}{Re}\frac{1}{2}\left\{\left(\frac{\mu_t}{\rho\sigma_k\nu}\right)\Big|_{k+1} + \left(\frac{\mu_t}{\rho\sigma_k\nu}\right)\Big|_k\right\}$$

$$\frac{\partial \beta_{k\,k+\frac{1}{2}}}{\partial \rho} = -\frac{1}{Re}\frac{1}{2}\left(\frac{\mu_t}{\rho^2\sigma_k\nu}\right) \tag{A.12}$$

$$N^L_{+\frac{1}{2}} = \begin{pmatrix} 0 & 0 & 0 & 0 & 0 & 0 & 0 \\ -\alpha_{k+\frac{1}{2}}\frac{[d_3 u_{k+1}+d_6 v_{k+1}+d_9 w_{k+1}]}{\rho_{k+1}} & \alpha_{k+\frac{1}{2}}\frac{d_3}{\rho_{k+1}} & \alpha_{k+\frac{1}{2}}\frac{d_6}{\rho_{k+1}} & \alpha_{k+\frac{1}{2}}\frac{d_9}{\rho_{k+1}} & 0 & 0 & 0 \\ -\alpha_{k+\frac{1}{2}}\frac{[d_6 u_{k+1}+d_{14} v_{k+1}+d_{17} w_{k+1}]}{\rho_{k+1}} & \alpha_{k+\frac{1}{2}}\frac{d_6}{\rho_{k+1}} & \alpha_{k+\frac{1}{2}}\frac{d_{14}}{\rho_{k+1}} & \alpha_{k+\frac{1}{2}}\frac{d_{18}}{\rho_{k+1}} & 0 & 0 & 0 \\ -\alpha_{k+\frac{1}{2}}\frac{[d_9 u_{k+1}+d_{17} v_{k+1}+d_{24} w_{k+1}]}{\rho_{k+1}} & \alpha_{k+\frac{1}{2}}\frac{d_9}{\rho_{k+1}} & \alpha_{k+\frac{1}{2}}\frac{d_{17}}{\rho_{k+1}} & \alpha_{k+\frac{1}{2}}\frac{d_{24}}{\rho_{k+1}} & 0 & 0 & 0 \\ n_{5,1} & n_{5,2} & n_{5,3} & n_{5,4} & d_{25}\alpha_Q\frac{\partial T}{\partial\rho\epsilon}\Big|_{k+1} & d_{25}\alpha_Q\frac{\partial T}{\partial\rho k}\Big|_{k+1} & 0 \\ -d_{25}\alpha_k\frac{k_{k+1}}{\rho_{k+1}} + (\rho k\Big|_{k+1}+\rho k\Big|_{k+1})\frac{\partial\beta_k}{\partial\rho} & 0 & 0 & 0 & 0 & d_{25}\left(\alpha_k\frac{1}{\rho_{k+1}}+\beta_k\right) & 0 \\ -d_{25}\alpha_\epsilon\frac{\epsilon_{k+1}}{\rho_{k+1}} & 0 & 0 & 0 & 0 & 0 & d_{25}\alpha_\epsilon\frac{1}{\rho_{k+1}} \end{pmatrix} \tag{A.13}$$

Here

$$N^R_{k+\frac{1}{2}} \equiv \frac{\partial T_{k+\frac{1}{2}}}{\partial Q_{k+1}}$$

$$n_{5,1} = d_{25}\alpha_Q \frac{\partial T}{\partial \rho}\mid_{k+1} - \alpha_{k+\frac{1}{2}}\left[d_3\frac{u_{k+1}^2}{\rho_{k+1}} + d_{14}\frac{v_{k+1}^2}{\rho_{k+1}} + d_{24}\frac{w_{k+1}^2}{\rho_{k+1}}\right.$$

$$\left. +2d_6\frac{u_{k+1}v_{k+1}}{\rho_{k+1}} + 2d_9\frac{u_{k+1}w_{k+1}}{\rho_{k+1}} + 2d_{17}\frac{v_{k+1}w_{k+1}}{\rho_{k+1}}\right]$$

$$n_{5,2} = d_{26}\alpha_Q \frac{\partial T}{\partial \rho u}\mid_{k+1} + \alpha_{k+\frac{1}{2}}\left[d_3\frac{u_{k+1}}{\rho_{k+1}} + d_6\frac{v_{k+1}}{\rho_{k+1}} + d_9\frac{w_{k+1}}{\rho_{k+1}}\right]$$

$$n_{5,3} = d_{25}\alpha_Q \frac{\partial T}{\partial \rho v}\mid_{k+1} + \alpha_{k+\frac{1}{2}}\left[d_{14}\frac{v_{k+1}}{\rho_{k+1}} + d_6\frac{u_{k+1}}{\rho_{k+1}} + d_{17}\frac{w_{k+1}}{\rho_{k+1}}\right]$$

$$n_{5,4} = d_{25}\alpha_Q \frac{\partial T}{\partial \rho w}\mid_{k+1} + \alpha_{k+\frac{1}{2}}\left[d_{24}\frac{w_{k+1}}{\rho_{k+1}} + d_9\frac{u_{k+1}}{\rho_{k+1}} + d_{17}\frac{v_{k+1}}{\rho_{k+1}}\right]$$

The Jacobians are evaluated at the cell faces using the conservative variables in the neighboring cells.

The Jacobian matrix O was not obtained by differentiating source terms with respect to conservative variables. Instead, it was evaluated as follows:

$$O = \begin{pmatrix} 0 & 0 & 0 & 0 & 0 & \frac{\Delta(\text{SourceTerms})}{\Delta(\rho k)} & 0 \\ 0 & 0 & 0 & 0 & 0 & 0 & \frac{\Delta(\text{SourceTerms})}{\Delta(\rho \epsilon)} \end{pmatrix} \quad (A.14)$$

The resulting matrix is:

$$O = \begin{pmatrix} 0 & 0 & 0 & 0 & 0 & \frac{\epsilon}{k} & 0 \\ 0 & 0 & 0 & 0 & 0 & 0 & \frac{C_{\epsilon_2} f_2 \epsilon}{k} \end{pmatrix} \quad (A.15)$$

Such approach was previously employed in the CRAFT code with the Chien's $k - \epsilon$ model. Contribution from Production terms is neglected. Only diagonal elements are used to enchance diagonal dominance.

Appendix B

Tabular Form of the Low Reynolds Number Correction for f_μ

The following are the partial results found by Knight for the computation of f_μ versus R_t [6].

R_t	f_μ	R_t	f_μ	R_t	f_μ
0.0	0.031481	0.11572E-07	0.031481	0.65107E-07	0.031481
0.22891E-06	0.031481	0.62229E-06	0.031481	0.14382E-05	0.031481
0.29723E-05	0.031481	0.56618E-05	0.031481	0.10136E-04	0.031481
0.17282E-04	0.031481	0.28333E-04	0.031481	0.44974E-04	0.031481
0.69491E-04	0.031481	0.10495E-03	0.031481	0.15544E-03	0.031481
0.22637E-03	0.031481	0.32485E-03	0.031481	0.46016E-03	0.031481
0.64444E-03	0.031481	0.89336E-03	0.031481	0.12272E-02	0.031481
0.16722E-02	0.031481	0.22617E-02	0.031481	0.30388E-02	0.031481
0.40582E-02	0.031481	0.53898E-02	0.031481	0.71224E-02	0.031481
0.93687E-02	0.031481	0.12271E-01	0.031481	0.16010E-01	0.031481
0.20814E-01	0.031481	0.26968E-01	0.031481	0.34833E-01	0.031481
0.44863E-01	0.031481	0.57624E-01	0.031481	0.73828E-01	0.031481
0.94362E-01	0.031481	0.12034E+00	0.031481	0.15313E+00	0.031481
0.19446E+00	0.031481	0.24645E+00	0.031481	0.31175E+00	0.031481
0.39360E+00	0.031481	0.49603E+00	0.031481	0.62395E+00	0.031481
0.78339E+00	0.031481	0.98173E+00	0.031481	0.12279E+01	0.031481
1.5327	0.031481	1.9092	0.031481	2.3729	0.031481
2.9424	0.031481	3.6394	0.031481	4.4897	0.031481
5.5228	0.031481	6.7728	0.031481	8.2783	0.031481
10.083	0.031481	12.233	0.031481	14.781	0.031481
17.782	0.031481	21.293	0.031481	25.369	0.031481
30.068	0.031481	35.439	0.031481	41.529	0.031481
48.372	0.031633	55.991	0.031972	64.394	0.032508
73.570	0.033258	83.491	0.034240	94.107	0.035475
105.35	0.036988	117.13	0.038812	129.35	0.040981

Table B.1: Tabular Form of f_μ vs. Re_t

R_t	f_μ	R_t	f_μ	R_t	f_μ
141.89	0.043536	154.64	0.046524	167.49	0.049999
180.31	0.054020	193.02	0.058652	205.53	0.063969
217.78	0.070048	229.74	0.076975	241.37	0.084840
252.68	0.093735	263.67	0.103757	274.37	0.115004
284.80	0.127571	295.00	0.141547	305.00	0.157011
314.84	0.174022	324.53	0.192609	334.12	0.212758
343.62	0.234389	353.05	0.257334	362.44	0.281294
371.81	0.305798	381.20	0.330134	390.66	0.353272
399.79	0.372845	408.68	0.387696	417.44	0.397520
426.14	0.406392	434.79	0.414960	443.39	0.423240
451.95	0.431248	460.46	0.439000	468.93	0.446509
477.36	0.453786	485.76	0.460845	494.12	0.467695
502.46	0.474347	510.76	0.480810	519.04	0.487093
527.29	0.493203	535.51	0.499150	543.71	0.504939
551.88	0.510578	560.03	0.516072	568.17	0.521429
576.28	0.526653	584.37	0.531750	592.44	0.536724
600.50	0.541582	608.53	0.546326	616.55	0.550962
624.56	0.555493	632.55	0.559923	640.52	0.564256
648.48	0.568495	656.42	0.572644	664.35	0.576705
672.27	0.580682	680.18	0.584577	688.07	0.588393
695.95	0.592133	703.82	0.595800	711.68	0.599394
719.52	0.602920	727.36	0.606378	735.18	0.609772
743.00	0.613102	750.80	0.616371	758.60	0.619581
766.39	0.622733	774.16	0.625829	781.93	0.628871
789.69	0.631860	797.44	0.634798	805.18	0.637686
812.92	0.640525	820.64	0.643317	828.36	0.646063
836.07	0.648764	843.77	0.651422	851.47	0.654037
859.16	0.656610	866.84	0.659144	874.51	0.661638
882.18	0.664094	889.84	0.666513	897.50	0.668895
905.14	0.671241	912.79	0.673553	920.42	0.675831
928.05	0.678076	935.68	0.680288	943.29	0.682469
950.91	0.684619	958.51	0.686739	966.11	0.688830
973.71	0.690892	981.30	0.692925	988.89	0.694931
996.47	0.696910	1004.04	0.698863	1011.61	0.700790
1019.18	0.702692	1026.74	0.704569	1034.29	0.706422
1041.84	0.708251	1049.39	0.710057	1056.93	0.711840
1064.47	0.713601	1072.00	0.715340	1079.53	0.717058
1087.05	0.718755	1094.57	0.720431	1102.09	0.722087
1109.60	0.723723	1117.11	0.725340	1124.61	0.726938
1132.11	0.728517	1139.61	0.730078	1147.10	0.731621

Table B.2: Tabular Form of f_μ vs. Re_t (Continued)

R_t	f_μ	R_t	f_μ	R_t	f_μ
1154.59	0.733147	1162.07	0.734655	1169.56	0.736146
1177.03	0.737621	1184.51	0.739079	1191.98	0.740521
1199.44	0.741947	1206.91	0.743358	1214.37	0.744753
1221.82	0.746134	1229.27	0.747499	1236.72	0.748851
1244.17	0.750188	1251.61	0.751511	1259.05	0.752820
1266.49	0.754116	1273.92	0.755399	1281.36	0.756668
1288.78	0.757925	1296.21	0.759169	1303.63	0.760401
1311.05	0.761620	1318.46	0.762827	1325.88	0.764023
1333.29	0.765206	1340.69	0.766379	1348.10	0.767540
1355.50	0.768690	1362.90	0.769829	1370.30	0.770957
1377.69	0.772074	1385.08	0.773182	1392.47	0.774278
1399.85	0.775365	1407.24	0.776442	1414.62	0.777509
1422.00	0.778566	1429.37	0.779613	1436.74	0.780651
1444.12	0.781680	1451.48	0.782700	1458.85	0.783711
1466.21	0.784713	1473.57	0.785706	1480.93	0.786690
1488.29	0.787666	1495.64	0.788634	1503.00	0.789593
1510.35	0.790544	1517.69	0.791487	1525.04	0.792422
1532.38	0.793350	1539.72	0.794269	1547.06	0.795181
1554.40	0.796086	1561.73	0.796983	1569.06	0.797872
1576.39	0.798755	1583.72	0.799630	1591.05	0.800499
1598.37	0.801360	1605.70	0.802215	1613.02	0.803062
1620.33	0.803903	1627.65	0.804738	1634.96	0.805566
1642.28	0.806387	1649.59	0.807203	1656.90	0.808012
1664.20	0.808814	1671.51	0.809611	1678.81	0.810402
1686.11	0.811186	1693.41	0.811965	1700.71	0.812738
1708.00	0.813505	1715.30	0.814267	1722.59	0.815023
1729.88	0.815773	1737.17	0.816518	1744.46	0.817257
1751.74	0.817992	1759.02	0.818720	1766.31	0.819444
1773.59	0.820163	1780.86	0.820876	1788.14	0.821584
1795.42	0.822288	1802.69	0.822986	1809.96	0.823680
1817.23	0.824368	1824.50	0.825052	1831.77	0.825731
1839.03	0.826406	1846.29	0.827076	1853.56	0.827742
1860.82	0.828402	1868.08	0.829059	1875.33	0.829711
1882.59	0.830359	1889.84	0.831002	1897.10	0.831641
1904.35	0.832276	1911.60	0.832907	1918.85	0.833534
1926.10	0.834156	1933.34	0.834775	1940.58	0.835389
1947.83	0.836000	1955.07	0.836607	1962.31	0.837209
1969.55	0.837808	1976.78	0.838403	1984.02	0.838995
1991.25	0.839583	1998.49	0.840167	2005.72	0.840747
2012.95	0.841324	2020.18	0.841897	2027.41	0.842467

Table B.3: Tabular Form of f_μ vs. Re_t (Continued)

R_t	f_μ	R_t	f_μ	R_t	f_μ
2034.63	0.843033	2041.86	0.843596	2049.08	0.844155
2056.30	0.844711	2063.52	0.845263	2070.74	0.845813
2077.96	0.846359	2085.18	0.846901	2092.39	0.847441
2099.61	0.847977	2106.82	0.848510	2114.03	0.849040
2121.24	0.849567	2128.45	0.850091	2135.66	0.850612
2142.87	0.851129	2150.07	0.851644	2157.28	0.852156
2164.48	0.852665	2171.68	0.853171	2178.89	0.853674
2186.09	0.854174	2193.28	0.854672	2200.48	0.855166
2207.68	0.855658	2214.87	0.856147	2222.07	0.856633
2229.26	0.857117	2236.45	0.857598	2243.64	0.858077
2250.83	0.858552	2258.02	0.859025	2265.21	0.859496
2272.39	0.859964	2279.58	0.860429	2286.76	0.860892
2293.94	0.861353	2301.12	0.861811	2308.31	0.862267
2315.48	0.862720	2322.66	0.863170	2329.84	0.863619
2337.02	0.864065	2344.19	0.864509	2351.37	0.864950
2358.54	0.865389	2365.71	0.865826	2372.88	0.866260
2380.05	0.866693	2387.22	0.867123	2394.39	0.867550
2401.55	0.867976	2408.72	0.868400	2415.88	0.868821
2423.05	0.869240	2430.21	0.869657	2437.37	0.870072
2444.53	0.870485	2451.69	0.870896	2458.85	0.871305
2466.01	0.871712	2473.17	0.872117	2480.32	0.872520
2487.48	0.872921	2494.63	0.873319	2501.78	0.873716
2508.94	0.874111	2516.09	0.874505	2523.24	0.874896
2530.39	0.875285	2537.53	0.875673	2544.68	0.876058
2551.83	0.876442	2558.97	0.876824	2566.12	0.877204
2573.26	0.877582	2580.40	0.877959	2587.54	0.878334
2594.68	0.878707	2601.82	0.879078	2608.96	0.879448
2616.10	0.879815	2623.24	0.880181	2630.37	0.880546
2637.51	0.880909	2644.64	0.881270	2651.78	0.881629
2658.91	0.881987	2666.04	0.882343	2673.17	0.882698
2680.30	0.883051	2687.43	0.883402	2694.56	0.883752
2701.69	0.884100	2708.82	0.884447	2715.94	0.884792
2723.07	0.885136	2730.19	0.885478	2737.31	0.885819
2744.44	0.886158	2751.56	0.886495	2758.68	0.886832
2765.80	0.887166	2772.92	0.887499	2780.04	0.887831
2787.15	0.888162	2794.27	0.888491	2801.39	0.888818
2808.50	0.889144	2815.61	0.889469	2822.73	0.889792
2829.84	0.890114	2836.95	0.890435	2844.06	0.890754
2851.17	0.891072	2858.28	0.891388	2865.39	0.891704
2872.50	0.892018	2879.61	0.892330	2886.71	0.892642

Table B.4: Tabular Form of f_μ vs. Re_t (Continued)

R_t	f_μ	R_t	f_μ	R_t	f_μ
2893.82	0.892952	2900.92	0.893260	2908.03	0.893568
2915.13	0.893874	2922.23	0.894179	2929.33	0.894483
2936.43	0.894785	2943.53	0.895086	2950.63	0.895386
2957.73	0.895685	2964.83	0.895983	2971.93	0.896279
2979.02	0.896574	2986.12	0.896868	2993.21	0.897161
3000.31	0.897453	3007.40	0.897744	3014.49	0.898033
3021.59	0.898321	3028.68	0.898608	3035.77	0.898894
3042.86	0.899179	3049.95	0.899463	3057.04	0.899746
3064.12	0.900027	3071.21	0.900308	3078.30	0.900587
3085.38	0.900865	3092.47	0.901143	3099.55	0.901419
3106.63	0.901694	3113.72	0.901968	3120.80	0.902241
3127.88	0.902513	3134.96	0.902784	3142.04	0.903054
3149.12	0.903323	3156.20	0.903591	3163.28	0.903858
3170.35	0.904124	3177.43	0.904388	3184.51	0.904652
3191.58	0.904915	3198.66	0.905177	3205.73	0.905438
3212.80	0.905698	3219.88	0.905957	3226.95	0.906216
3234.02	0.906473	3241.09	0.906729	3248.16	0.906984
3255.23	0.907239	3262.30	0.907492	3269.36	0.907745
3276.43	0.907997	3283.50	0.908247	3290.56	0.908497
3297.63	0.908746	3304.69	0.908994	3311.76	0.909241
3318.82	0.909488	3325.88	0.909733	3332.95	0.909978
3340.01	0.910222	3347.07	0.910464	3354.13	0.910706
3361.19	0.910948	3368.25	0.911188	3375.31	0.911427
3382.36	0.911666	3389.42	0.911904	3396.48	0.912141
3403.53	0.912377	3410.59	0.912612	3417.64	0.912847
3424.70	0.913081	3431.75	0.913314	3438.80	0.913546
3445.86	0.913777	3452.91	0.914008	3459.96	0.914238
3467.01	0.914467	3474.06	0.914695	3481.11	0.914923
3488.16	0.915149	3495.20	0.915375	3502.25	0.915600
3509.30	0.915825	3516.34	0.916049	3523.39	0.916272
3530.44	0.916494	3537.48	0.916715	3544.52	0.916936
3551.57	0.917156	3558.61	0.917376	3565.65	0.917594
3572.69	0.917812	3579.73	0.918029	3586.77	0.918246
3593.81	0.918462	3600.85	0.918677	3607.89	0.918891
3614.93	0.919105	3621.97	0.919318	3629.01	0.919530
3636.04	0.919742	3643.08	0.919953	3650.11	0.920163
3657.15	0.920373	3664.18	0.920582	3671.22	0.920790
3678.25	0.920998	3685.28	0.921205	3692.31	0.921411
3699.34	0.921617	3706.38	0.921822	3713.41	0.922026
3720.44	0.922230	3727.46	0.922433	3734.49	0.922636

Table B.5: Tabular Form of f_μ vs. Re_t (Continued)

R_t	f_μ	R_t	f_μ	R_t	f_μ
3741.52	0.922838	3748.55	0.923039	3755.58	0.923239
3762.60	0.923440	3769.63	0.923639	3776.65	0.923838
3783.68	0.924036	3790.70	0.924234	3797.73	0.924430
3804.75	0.924627	3811.77	0.924823	3818.80	0.925018
3825.82	0.925212	3832.84	0.925406	3839.86	0.925600
3846.88	0.925793	3853.90	0.925985	3860.92	0.926177
3867.94	0.926368	3874.96	0.926558	3881.97	0.926748
3888.99	0.926938	3896.01	0.927127	3903.02	0.927315
3910.04	0.927503	3917.05	0.927690	3924.07	0.927877
3931.08	0.928063	3938.10	0.928248	3945.11	0.928433
3952.12	0.928618	3959.13	0.928802	3966.15	0.928985
3973.16	0.929168	3980.17	0.929351	3987.18	0.929532
3994.19	0.929714	4001.20	0.929894	4008.20	0.930075
4015.21	0.930254	4022.22	0.930434	4029.23	0.930612
4036.23	0.930791	4043.24	0.930968	4050.25	0.931146
4057.25	0.931322	4064.26	0.931499	4071.26	0.931674
4078.26	0.931849	4085.27	0.932024	4092.27	0.932198
4099.27	0.932372	4106.27	0.932545	4113.28	0.932718
4120.28	0.932891	4127.28	0.933062	4134.28	0.933234
4141.28	0.933405	4148.27	0.933575	4155.27	0.933745
4162.27	0.933914	4169.27	0.934084	4176.27	0.934252
4183.26	0.934420	4190.26	0.934588	4197.25	0.934755
4204.25	0.934922	4211.24	0.935088	4218.24	0.935254
4225.23	0.935419	4232.23	0.935584	4239.22	0.935749
4246.21	0.935913	4253.20	0.936076	4260.20	0.936239
4267.19	0.936402	4274.18	0.936564	4281.17	0.936726
4288.16	0.936888	4295.15	0.937049	4302.14	0.937209
4309.12	0.937369	4316.11	0.937529	4323.10	0.937688
4330.09	0.937847	4337.07	0.938006	4344.06	0.938164
4351.05	0.938322	4358.03	0.938479	4365.02	0.938636
4372.00	0.938792	4378.99	0.938948	4385.97	0.939104
4392.95	0.939259	4399.94	0.939414	4406.92	0.939568
4413.90	0.939722	4420.88	0.939876	4427.86	0.940029
4434.84	0.940182	4441.82	0.940334	4448.80	0.940486
4455.78	0.940638	4462.76	0.940789	4469.74	0.940940
4476.72	0.941091	4483.70	0.941241	4490.67	0.941391
4497.65	0.941540	4504.63	0.941689	4511.60	0.941838
4518.58	0.941986	4525.55	0.942134	4532.53	0.942281
4539.50	0.942428	4546.48	0.942575	4553.45	0.942722
4560.42	0.942868	4567.40	0.943013	4574.37	0.943159

Table B.6: Tabular Form of f_μ vs. Re_t (Continued)

R_t	f_μ	R_t	f_μ	R_t	f_μ
4581.34	0.943304	4588.31	0.943448	4595.28	0.943593
4602.25	0.943736	4609.22	0.943880	4616.19	0.944023
4623.16	0.944166	4630.13	0.944309	4637.10	0.944451
4644.07	0.944593	4651.04	0.944734	4658.00	0.944875
4664.97	0.945016	4671.94	0.945156	4678.90	0.945296
4685.87	0.945436	4692.84	0.945576	4699.80	0.945715
4706.77	0.945854	4713.73	0.945992	4720.69	0.946130
4727.66	0.946268	4734.62	0.946405	4741.58	0.946542
4748.55	0.946679	4755.51	0.946816	4762.47	0.946952
4769.43	0.947088	4776.39	0.947223	4783.35	0.947358
4790.31	0.947493	4797.27	0.947628	4804.23	0.947762
4811.19	0.947896	4818.15	0.948030	4825.11	0.948163
4832.06	0.948296	4839.02	0.948429	4845.98	0.948561
4852.94	0.948693	4859.89	0.948825	4866.85	0.948956
4873.80	0.949087	4880.76	0.949218	4887.71	0.949349
4894.67	0.949479	4901.62	0.949609	4908.58	0.949739
4915.53	0.949868	4922.48	0.949997	4929.44	0.950126
4936.39	0.950254	4943.34	0.950383	4950.29	0.950511
4957.24	0.950638	4964.19	0.950766	4971.14	0.950893
4978.09	0.951019	4985.04	0.951146	4991.99	0.951272
4998.94	0.951398	5005.89	0.951524	5012.84	0.951649
5019.79	0.951774	5026.73	0.951899	5033.68	0.952023
5040.63	0.952147	5047.58	0.952271	5054.52	0.952395
5061.47	0.952518	5068.41	0.952642	5075.36	0.952764
5082.30	0.952887	5089.25	0.953009	5096.19	0.953131
5103.14	0.953253	5110.08	0.953375	5117.02	0.953496
5123.96	0.953617	5130.91	0.953738	5137.85	0.953858
5144.79	0.953978	5151.73	0.954098	5158.67	0.954218
5165.61	0.954337	5172.55	0.954456	5179.49	0.954575
5186.43	0.954694	5193.37	0.954812	5200.31	0.954931
5207.25	0.955048	5214.19	0.955166	5221.13	0.955283
5228.07	0.955401	5235.00	0.955517	5241.94	0.955634
5248.88	0.955750	5255.81	0.955867	5262.75	0.955982
5269.68	0.956098	5276.62	0.956214	5283.56	0.956329
5290.49	0.956444	5297.42	0.956558	5304.36	0.956673
5311.29	0.956787	5318.23	0.956901	5325.16	0.957015
5332.09	0.957128	5339.02	0.957241	5345.96	0.957354
5352.89	0.957467	5359.82	0.957580	5366.75	0.957692
5373.68	0.957804	5380.61	0.957916	5387.54	0.958027
5394.47	0.958139	5401.40	0.958250	5408.33	0.958361

Table B.7: Tabular Form of f_μ vs. Re_t (Continued)

R_t	f_μ	R_t	f_μ	R_t	f_μ
5415.26	0.958471	5422.19	0.958582	5429.12	0.958692
5436.05	0.958802	5442.97	0.958912	5449.90	0.959021
5456.83	0.959131	5463.75	0.959240	5470.68	0.959349
5477.61	0.959457	5484.53	0.959566	5491.46	0.959674
5498.38	0.959782	5505.31	0.959890	5512.23	0.959997
5519.16	0.960105	5526.08	0.960212	5533.01	0.960319
5539.93	0.960425	5546.85	0.960532	5553.78	0.960638
5560.70	0.960744	5567.62	0.960850	5574.54	0.960956
5581.46	0.961061	5588.39	0.961166	5595.31	0.961271
5602.23	0.961376	5609.15	0.961481	5616.07	0.961585
5622.99	0.961689	5629.91	0.961793	5636.83	0.961897
5643.75	0.962000	5650.66	0.962104	5657.58	0.962207
5664.50	0.962310	5671.42	0.962412	5678.34	0.962515
5685.25	0.962617	5692.17	0.962719	5699.09	0.962821
5706.00	0.962923	5712.92	0.963025	5719.84	0.963126
5726.75	0.963227	5733.67	0.963328	5740.58	0.963429
5747.50	0.963529	5754.41	0.963630	5761.33	0.963730
5768.24	0.963830	5775.15	0.963930	5782.07	0.964029
5788.98	0.964129	5795.89	0.964228	5802.81	0.964327
5809.72	0.964426	5816.63	0.964524	5823.54	0.964623
5830.45	0.964721	5837.36	0.964819	5844.28	0.964917
5851.19	0.965015	5858.10	0.965112	5865.01	0.965209
5871.92	0.965307	5878.83	0.965404	5885.74	0.965500
5892.64	0.965597	5899.55	0.965693	5906.46	0.965790
5913.37	0.965886	5920.28	0.965981	5927.19	0.966077
5934.09	0.966173	5941.00	0.966268	5947.91	0.966363
5954.81	0.966458	5961.72	0.966553	5968.63	0.966647
5975.53	0.966742	5982.44	0.966836	5989.34	0.966930
5996.25	0.967024	6003.15	0.967118	6010.06	0.967211
6016.96	0.967305	6023.87	0.967398	6030.77	0.967491
6037.67	0.967584	6044.58	0.967677	6051.48	0.967769
6058.38	0.967861	6065.28	0.967954	6072.19	0.968046
6079.09	0.968137	6085.99	0.968229	6092.89	0.968321
6099.79	0.968412	6106.69	0.968503	6113.60	0.968594
6120.50	0.968685	6127.40	0.968776	6134.30	0.968866
6141.20	0.968957	6148.10	0.969047	6155.00	0.969137
6161.89	0.969227	6168.79	0.969316	6175.69	0.969406
6182.59	0.969495	6189.49	0.969584	6196.39	0.969673
6203.28	0.969762	6210.18	0.969851	6217.08	0.969940
6223.98	0.970028	6230.87	0.970116	6237.77	0.970204

Table B.8: Tabular Form of f_μ vs. Re_t (Continued)

R_t	f_μ	R_t	f_μ	R_t	f_μ
6244.67	0.970292	6251.56	0.970380	6258.46	0.970468
6265.35	0.970555	6272.25	0.970642	6279.14	0.970729
6286.04	0.970816	6292.93	0.970903	6299.83	0.970990
6306.72	0.971076	6313.61	0.971163	6320.51	0.971249
6327.40	0.971335	6334.29	0.971421	6341.19	0.971507
6348.08	0.971592	6354.97	0.971678	6361.87	0.971763
6368.76	0.971848	6375.65	0.971933	6382.54	0.972018
6389.43	0.972103	6396.32	0.972187	6403.21	0.972272
6410.11	0.972356	6417.00	0.972440	6423.89	0.972524
6430.78	0.972608	6437.67	0.972692	6444.56	0.972775
6451.45	0.972859	6458.33	0.972942	6465.22	0.973025
6472.11	0.973108	6479.00	0.973191	6485.89	0.973273
6492.78	0.973356	6499.67	0.973438	6506.55	0.973520
6513.44	0.973602	6520.33	0.973684	6527.22	0.973766
6534.10	0.973848	6540.99	0.973929	6547.88	0.974011
6554.76	0.974092	6561.65	0.974173	6568.53	0.974254
6575.42	0.974335	6582.30	0.974416	6589.19	0.974496
6596.07	0.974577	6602.96	0.974657	6609.84	0.974737
6616.73	0.974817	6623.61	0.974897	6630.50	0.974977
6637.38	0.975056	6644.26	0.975136	6651.15	0.975215
6658.03	0.975294	6664.91	0.975373	6671.80	0.975452
6678.68	0.975531	6685.56	0.975610	6692.44	0.975688
6699.33	0.975766	6706.21	0.975845	6713.09	0.975923
6719.97	0.976001	6726.85	0.976079	6733.73	0.976156
6740.61	0.976234	6747.49	0.976311	6754.37	0.976389
6761.26	0.976466	6768.14	0.976543	6775.02	0.976620
6781.89	0.976697	6788.77	0.976773	6795.65	0.976850
6802.53	0.976926	6809.41	0.977003	6816.29	0.977079
6823.17	0.977155	6830.05	0.977231	6836.93	0.977307
6843.80	0.977382	6850.68	0.977458	6857.56	0.977533
6864.44	0.977609	6871.31	0.977684	6878.19	0.977759
6885.07	0.977834	6891.94	0.977909	6898.82	0.977983
6905.70	0.978058	6912.57	0.978132	6919.45	0.978207
6926.33	0.978281	6933.20	0.978355	6940.08	0.978429
6946.95	0.978502	6953.83	0.978576	6960.70	0.978650
6967.58	0.978723	6974.45	0.978797	6981.33	0.978870
6988.20	0.978943	6995.08	0.979016	7001.95	0.979089
7008.82	0.979161	7015.70	0.979234	7022.57	0.979306
7029.44	0.979379	7036.32	0.979451	7043.19	0.979523
7050.06	0.979595	7056.93	0.979667	7063.81	0.979739
7070.68	0.979811	7077.55	0.979882	7084.42	0.979954

Table B.9: Tabular Form of f_μ vs. Re_t (Continued)

R_t	f_μ	R_t	f_μ	R_t	f_μ
7091.30	0.980025	7098.17	0.980096	7105.04	0.980167
7111.91	0.980238	7118.78	0.980309	7125.65	0.980380
7132.52	0.980450	7139.39	0.980521	7146.26	0.980591
7153.13	0.980662	7160.00	0.980732	7166.87	0.980802
7173.74	0.980872	7180.61	0.980942	7187.48	0.981011
7194.35	0.981081	7201.22	0.981151	7208.09	0.981220
7214.96	0.981289	7221.83	0.981358	7228.70	0.981427
7235.57	0.981496	7242.43	0.981565	7249.30	0.981634
7256.17	0.981703	7263.04	0.981771	7269.91	0.981840
7276.77	0.981908	7283.64	0.981976	7290.51	0.982044
7297.38	0.982112	7304.24	0.982180	7311.11	0.982248
7317.98	0.982315	7324.84	0.982383	7331.71	0.982450
7338.58	0.982518	7345.44	0.982585	7352.31	0.982652
7359.17	0.982719	7366.04	0.982786	7372.91	0.982853
7379.77	0.982919	7386.64	0.982986	7393.50	0.983052
7400.37	0.983119	7407.23	0.983185	7414.10	0.983251
7420.96	0.983317	7427.83	0.983383	7434.69	0.983449
7441.55	0.983515	7448.42	0.983580	7455.28	0.983646
7462.15	0.983711	7469.01	0.983776	7475.87	0.983842
7482.74	0.983907	7489.60	0.983972	7496.46	0.984037
7503.33	0.984102	7510.19	0.984166	7517.05	0.984231
7523.91	0.984295	7530.78	0.984360	7537.64	0.984424
7544.50	0.984488	7551.36	0.984552	7558.23	0.984616
7565.09	0.984680	7571.95	0.984744	7578.81	0.984808
7585.67	0.984871	7592.53	0.984935	7599.40	0.984998
7606.26	0.985062	7613.12	0.985125	7619.98	0.985188
7626.84	0.985251	7633.70	0.985314	7640.56	0.985377
7647.42	0.985439	7654.28	0.985502	7661.14	0.985565
7668.00	0.985627	7674.86	0.985689	7681.72	0.985752
7688.58	0.985814	7695.44	0.985876	7702.30	0.985938
7709.16	0.986000	7716.02	0.986061	7722.88	0.986123
7729.74	0.986185	7736.60	0.986246	7743.46	0.986307
7750.32	0.986369	7757.17	0.986430	7764.03	0.986491
7770.89	0.986552	7777.75	0.986613	7784.61	0.986674
7791.47	0.986734	7798.32	0.986795	7805.18	0.986855
7812.04	0.986916	7818.90	0.986976	7825.76	0.987036
7832.61	0.987097	7839.47	0.987157	7846.33	0.987217
7853.19	0.987277	7860.04	0.987336	7866.90	0.987396
7873.76	0.987456	7880.61	0.987515	7887.47	0.987575
7894.33	0.987634	7901.18	0.987693	7908.04	0.987752
7914.90	0.987811	7921.75	0.987870	7928.61	0.987929

Table B.10: Tabular Form of f_μ vs. Re_t (Continued)

R_t	f_μ	R_t	f_μ	R_t	f_μ
7935.47	0.987988	7942.32	0.988047	7949.18	0.988105
7956.03	0.988164	7962.89	0.988222	7969.74	0.988280
7976.60	0.988339	7983.46	0.988397	7990.31	0.988455
7997.17	0.988513	8004.02	0.988571	8010.88	0.988629
8017.73	0.988686	8024.59	0.988744	8031.44	0.988801
8038.30	0.988859	8045.15	0.988916	8052.01	0.988974
8058.86	0.989031	8065.71	0.989088	8072.57	0.989145
8079.42	0.989202	8086.28	0.989259	8093.13	0.989315
8099.99	0.989372	8106.84	0.989429	8113.69	0.989485
8120.55	0.989541	8127.40	0.989598	8134.26	0.989654
8141.11	0.989710	8147.96	0.989766	8154.82	0.989822
8161.67	0.989878	8168.52	0.989934	8175.38	0.989990
8182.23	0.990045	8189.08	0.990101	8195.94	0.990156
8202.79	0.990212	8209.64	0.990267	8216.49	0.990322
8223.35	0.990377	8230.20	0.990432	8237.05	0.990487
8243.90	0.990542	8250.76	0.990597	8257.61	0.990652
8264.46	0.990706	8271.31	0.990761	8278.17	0.990815
8285.02	0.990870	8291.87	0.990924	8298.72	0.990978
8305.58	0.991032	8312.43	0.991086	8319.28	0.991140
8326.13	0.991194	8332.98	0.991248	8339.83	0.991302
8346.69	0.991355	8353.54	0.991409	8360.39	0.991462
8367.24	0.991516	8374.09	0.991569	8380.94	0.991622
8387.79	0.991676	8394.65	0.991729	8401.50	0.991782
8408.35	0.991835	8415.20	0.991887	8422.05	0.991940
8428.90	0.991993	8435.75	0.992045	8442.60	0.992098
8449.45	0.992150	8456.30	0.992203	8463.16	0.992255
8470.01	0.992307	8476.86	0.992359	8483.71	0.992411
8490.56	0.992463	8497.41	0.992515	8504.26	0.992567
8511.11	0.992619	8517.96	0.992670	8524.81	0.992722
8531.66	0.992774	8538.51	0.992825	8545.36	0.992876
8552.21	0.992928	8559.06	0.992979	8565.91	0.993030
8572.76	0.993081	8579.61	0.993132	8586.46	0.993183
8593.31	0.993234	8600.16	0.993284	8607.01	0.993335
8613.86	0.993385	8620.71	0.993436	8627.56	0.993486
8634.41	0.993537	8641.26	0.993587	8648.11	0.993637
8654.96	0.993687	8661.81	0.993737	8668.66	0.993787
8675.51	0.993837	8682.36	0.993887	8689.21	0.993937
8696.06	0.993986	8702.91	0.994036	8709.76	0.994085
8716.61	0.994135	8723.46	0.994184	8730.31	0.994234
8737.15	0.994283	8744.00	0.994332	8750.85	0.994381
8757.70	0.994430	8764.55	0.994479	8771.40	0.994528

Table B.11: Tabular Form of f_μ vs. Re_t (Continued)

R_t	f_μ	R_t	f_μ	R_t	f_μ
8778.25	0.994576	8785.10	0.994625	8791.95	0.994674
8798.80	0.994722	8805.65	0.994771	8812.50	0.994819
8819.35	0.994867	8826.19	0.994916	8833.04	0.994964
8839.89	0.995012	8846.74	0.995060	8853.59	0.995108
8860.44	0.995156	8867.29	0.995204	8874.14	0.995251
8880.99	0.995299	8887.84	0.995347	8894.68	0.995394
8901.53	0.995442	8908.38	0.995489	8915.23	0.995536
8922.08	0.995584	8928.93	0.995631	8935.78	0.995678
8942.63	0.995725	8949.48	0.995772	8956.33	0.995819
8963.17	0.995865	8970.02	0.995912	8976.87	0.995959
8983.72	0.996005	8990.57	0.996052	8997.42	0.996098
9004.27	0.996145	9011.12	0.996191	9017.97	0.996237
9024.81	0.996283	9031.66	0.996330	9038.51	0.996376
9045.36	0.996422	9052.21	0.996467	9059.06	0.996513
9065.91	0.996559	9072.76	0.996605	9079.61	0.996650
9086.46	0.996696	9093.30	0.996741	9100.15	0.996787
9107.00	0.996832	9113.85	0.996877	9120.70	0.996922
9127.55	0.996968	9134.40	0.997013	9141.25	0.997058
9148.10	0.997103	9154.95	0.997147	9161.79	0.997192
9168.64	0.997237	9175.49	0.997282	9182.34	0.997326
9189.19	0.997371	9196.04	0.997415	9202.89	0.997459
9209.74	0.997504	9216.59	0.997548	9223.44	0.997592
9230.29	0.997636	9237.14	0.997680	9243.99	0.997724
9250.83	0.997768	9257.68	0.997812	9264.53	0.997856
9271.38	0.997899	9278.23	0.997943	9285.08	0.997987
9291.93	0.998030	9298.78	0.998073	9305.63	0.998117
9312.48	0.998160	9319.33	0.998203	9326.18	0.998247
9333.03	0.998290	9339.88	0.998333	9346.73	0.998376
9353.58	0.998418	9360.43	0.998461	9367.28	0.998504
9374.13	0.998547	9380.98	0.998589	9387.83	0.998632
9394.68	0.998674	9401.53	0.998717	9408.38	0.998759
9415.23	0.998802	9422.08	0.998844	9428.93	0.998886
9435.78	0.998928	9442.63	0.998970	9449.48	0.999012
9456.33	0.999054	9463.18	0.999096	9470.03	0.999138
9476.88	0.999179	9483.73	0.999221	9490.58	0.999263
9497.43	0.999304	9504.28	0.999345	9511.13	0.999387
9517.98	0.999428	9524.83	0.999469	9531.68	0.999511
9538.54	0.999552	9545.39	0.999593	9552.24	0.999634
9559.09	0.999675	9565.94	0.999716	9572.79	0.999756
9579.64	0.999797	9586.49	0.999838	9593.34	0.999879
9600.20	0.999919	9613.90	1.000000	∞	1.000000

Table B.12: Tabular Form of f_μ vs. Re_t (Continued)

Appendix C

Eigenvectors

The sets of left and right eigenvectors in the way they are used in the CRAFT code [37] are presented here.

The eigenvalues are

$$\Lambda = diag\,(U + C, U - C, U, U, U, U, U) \tag{C.1}$$

where $U = l_x u + l_y v + l_z w$, $C = c\sqrt{l_x^2 + l_y^2 + l_z^2}$.

The left eigenvectors are:

$$
L = \begin{pmatrix}
(\gamma - 1)(\mathcal{K} - h) + c(c - \hat{U}) & -u(\gamma - 1) + c\hat{l}_x & -v(\gamma - 1) + c\hat{l}_y & -w(\gamma - 1) + c\hat{l}_z & \gamma - 1 & 0 & 0 \\
(\gamma - 1)(\mathcal{K} - h) + c(c + \hat{U}) & -u(\gamma - 1) - c\hat{l}_x & -v(\gamma - 1) - c\hat{l}_y & -w(\gamma - 1) - c\hat{l}_z & \gamma - 1 & 0 & 0 \\
\mathcal{K} - h & -u & -v & -w & 1 & 0 & 0 \\
-\hat{V} & p_x & p_y & p_z & 0 & 0 & 0 \\
-\hat{W} & q_x & q_y & q_z & 0 & 0 & 0 \\
-k0 & 0 & 0 & 0 & 1 & 0 \\
-\epsilon & 0 & 0 & 0 & 0 & 0 & 1
\end{pmatrix} \tag{C.2}
$$

The right eigenvectors are:

$$
R = \begin{pmatrix}
\frac{1}{2c^2} & \frac{1}{2c^2} & -\frac{\gamma-1}{c^2} & 0 & 0 & 0 & 0 \\
\frac{u+\hat{l}_x c}{2c^2} & \frac{u-\hat{l}_x c}{2c^2} & -\frac{(\gamma-1)u}{c^2} & p_x & q_x & 0 & 0 \\
\frac{v+\hat{l}_y c}{2c^2} & \frac{v-\hat{l}_y c}{2c^2} & -\frac{(\gamma-1)v}{c^2} & p_y & q_y & 0 & 0 \\
\frac{w+\hat{l}_z c}{2c^2} & \frac{w-\hat{l}_z c}{2c^2} & -\frac{(\gamma-1)w}{c^2} & p_z & q_z & 0 & 0 \\
\frac{h+\mathcal{K}+c\hat{U}}{c^2} & \frac{h+\mathcal{K}-c\hat{U}}{c^2} & \frac{c^2-(\gamma-1)(h+\mathcal{K})}{c^2} & \hat{V} & \hat{W} & 0 & 0 \\
\frac{k}{2c^2} & \frac{k}{2c^2} & \frac{-(\gamma-1)k}{c^2} & 0 & 0 & 1 & 0 \\
\frac{\epsilon}{2c^2} & \frac{\epsilon}{2c^2} & \frac{-(\gamma-1)\epsilon}{c^2} & 0 & 0 & 0 & 1
\end{pmatrix} \tag{C.3}
$$

where c is the speed of sound, $\mathcal{K} = \frac{u^2+v^2+w^2}{2}$, $\hat{U} = \hat{l}_x u + \hat{l}_y v + \hat{l}_z w$, $\hat{V} = p_x u + p_y v + p_z w$, $\hat{W} = q_x u + q_y v + q_z w$, $\hat{l}$ is the unit cell normal and $p = (p_x, p_y, p_z)^{\mathrm{T}}$, $q = (q_x, q_y, q_z)^{\mathrm{T}}$ are two arbitrary unit vectors perpendicular to each other and vector $\hat{l}$.

References

[1] B. Baldwin and H. Lomax. Thin Layer Approximation and Algebraic Model for Separated Flows. AIAA Paper 78-257, 1978.

[2] J. Bardina and T. Coakley. Three-Dimensional Navier-Stokes Simulations with Two-Equation Turbulence Models of Intersecting Shock Waves/Turbulent Boundary Layer at Mach 8.3. AIAA Paper 94-1905, June 1994.

[3] J. Bardina and T. Coakley. The Structure of Intersecting Shock-Waves/Turbulent Boundary Layer Interaction Flow. AIAA Paper 95-2215, June 1995.

[4] P. Batcho, A. Ketchum, S. Bogdonoff, and E. Fernando. Preliminary Study of the Interactions Caused by Crossing Shock Waves and a Turbulent Boundary Layer. AIAA Paper 89-0359, 1989.

[5] R. Becht. Evaluation of a Low Reynolds Number Correction to the $k - \epsilon$ Two Equation Compressible Turbulence Model. Master's thesis, Rutgers University, 1994.

[6] R. Becht and D. Knight. A Simple Low Reynolds Number Modification for the Compressible $k - \epsilon$ Model. AIAA Paper 95-1111, January 1995.

[7] P. Bradshaw. Compressible Turbulent Shear Layers. *Annual Review of Fluid Mechanics*, 9:33–54, 1977.

[8] S. Chakravarthy and S. Osher. A New Class of High Accuracy TVD Schemes for Hyperbolic Conservation Laws. AIAA Paper 85-0363, 1985.

[9] K.-Y. Chien. Predictions of Channel and Boundary Layer Flows with a Low Reynolds Number Turbulence Model. *AIAA Journal*, 20:33–38, January 1982.

[10] G. Degrez, editor. *AGARD Special Course on Shock-Wave/Turbulent Boundary-Layer Interactions in Supersonic and Hypersonic Flow*. Advisory Group for Aerospace Research and Development, August 1993. AGARD Report 792.

[11] Department of Mechhanical and Aerospace Engineering, Rutgers University. *Proceedings of the AFOSR Workshop on Fluid Dynamics of High Speed Inlets*, New Brunswick, NJ, May 1994 1994.

[12] C. Edwards. A Forebody Design Technique for Highly Integrated Bottom - Mounted Scramjets with Application to a Hypersonic Research Airplane. Technical Report TN D-8369, NASA, December 1976.

[13] D. Gaitonde and D. Knight. Numerical Experiments on the 3-D Shock-Wave Boundary Layer Interaction Generated by a Sharp Fin. AIAA Paper 88-0309, 1988.

[14] D. Gaitonde and D. Knight. Numerical Investigation of Bleed on Three-Dimensional Turbulent Interactions Due to Sharp Fins. *AIAA Journal*, 29:1878–1885, 1991.

[15] D. Gaitonde and J. Shang. Calculations on a Double - Fin Turbulent Interaction at High Speed. AIAA Paper 93-3432, 1993.

[16] T. Garrison and G. Settles. Flowfield Visualization of Crossing Shock-Wave/Boundary Layer Interactions. AIAA Paper 92-0750, 1992.

[17] T. Garrison and G. Settles. Laser Interferometer Skin Friction Measurements of Crossing - Shock Wave / Turbulent Boundary - Layer Interactions. AIAA Paper 93-3072, 1993.

[18] T. Garrison, G. Settles, N. Narayanswami, and D. Knight. Structure of Crossing-Shock Wave/Turbulent Boundary Layer Interactions. AIAA Paper 92-3670, 1992.

[19] T. Garrison, G. Settles, N. Narayanswami, and D. Knight. Comparison of Flow-field Surveys and Computations of a Crossing - Shock Wave / Boundary - Layer Interaction. AIAA Paper 94-2273, 1994.

[20] T. Garrison, G. Settles, N. Narayanswami, and D. Knight. Comparison of Flow-field Surveys and Computations of a Crossing - Shock Wave / Boundary - Layer Interaction. AIAA Paper 94-2273, 1994.

[21] W. Jones and B. Launder. The Prediction of Laminarization with a Two-Equation Model of Turbulence. *Int. Journal of Heat and Mass Transfer*, 15:301–304, 1972.

[22] D. Knight. Notes about the CRAFT Code. Unpublished, 1994.

[23] D. Knight, D. Badekas, C. Horstman, and G. Settles. Quasi-conical Flow-field Structure of the Three-Dimensional Single Fin Interaction. *AIAA Journal*, 30:2809–2816, 1992.

[24] D. Knight, T. Garrison, G. Settles, A. Zheltovodov, A. Maksimov, A. Shevchenko, and S. Vorontsov. Asymmetric Crossing shock Wave - Turbulent Boundary Layer Interaction. AIAA Paper 95-0231, 1995.

[25] D. Knight, C. Horstman, and S. Bogdonoff. Structure of Supersonic Turbulent Flow Past a Swept Compression Corner. *AIAA Journal*, 30:890–896, 1992.

[26] D. Knight, C. Horstman, and D. Monson. The Hypersonic Shock Wave-Turbulent Boundary Layer Interaction Generated by a Sharp Fin at Mach 8.2. AIAA Paper 92-0747, 1992.

[27] D. Knight, C. Horstman, and G. Settles. Three Dimensional Shock Wave - Turbulent Boundary Layer Interactions Generated by a Sharp Fin at Mach 4. AIAA Paper 91-0648, 1991.

[28] D. Knight, C. Horstman, G. Settles, and A. Zheltovodov. 3-D Shock Wave-Turbulent Boundary Layer Interactions Generated by a Single Fin. *The Russian Journal of Theoretical and Applied Mechanics*, 2(3), 1992.

[29] D. Knight, C. Horstman, B. Shapey, and S. Bogdonoff. Structure of Supersonic Turbulent Flow Past a Sharp Fin. *AIAA Journal*, 25:1331–1337, 1987.

[30] D. Knight, D. Raufer, C. Horstman, A. Ketchum, and S. Bogdonoff. Supersonic Turbulent Flow Past a 3-D Swept Compression Corner at Mach 3 - Part II. AIAA Paper 88-0310, 1988.

[31] M. Kussoy, K. Horstman, and C. Horstman. Hypersonic Crossing Shock Wave / Turbulent Boundary Layer Interactions. *AIAA Journal*, 31:2197–2203, December 1993.

[32] C. Lam and K. Bremhorst. Modified Form of the $k-\epsilon$ Model for Predicting Wall Turbulence. *Journal of Fluids Engineering*, 103:456–460, 1981.

[33] B. Launder and B. Sharma. Application of the Energy Dissipation Model of Turbulence to the Calculation of Flow Near a Spinning Disk. *Letters in Heat and Mass Transfer*, 1:131–138, 1974.

[34] Y. Lee, G. Settles, and C. Horstman. Heat Transfer Measurements and CFD Comparison of Swept Shock Wave/Boundary Layer Interactions. AIAA Paper 92-3665, 1992.

[35] D. Mee, R. Stalker, and J. Stollery. Glancing Interactions between Single and Intersecting Oblique Shock Waves and a Turbulent Boundary Layer. *Journal of Fluid Mechanics*, 170:411–433, 1986.

[36] F.R. Menter. Zonal Two Equation $k-\omega$ Turbulence Models for Aerodynamics Flows. AIAA Paper No. 93-2906, 1993.

[37] G. Molvik and C. Merkle. A Set of Strongly Coupled, Upwind Algorithms for Computing Flows in Chemical Nonequilibrium. AIAA Paper 89-0199, 1989.

[38] A. Monin and A. Yaglom. *Statistical Fluid Mechanics: Mechanics of Turbulence.* The MIT Press, Cambridge, 1971.

[39] J. H. Morrison. A Compressible Navier-Stokes Solver with Two-Equation and Reynolds Stress Turbulence Closure Models. CR 4440, NASA, May 1992.

[40] N. Narayanswami, C. C. Horstman, and D. Knight. Computation of Crossing Shock Turbulent Boundary Layer Interaction at Mach 8.3. *AIAA Journal*, 31:1369–1376, August 1993.

[41] N. Narayanswami, C. C. Horstman, and D. Knight. Numerical Simulation of Crossing Shock / Turbulent Boundary Layer Interaction at Mach 8.3 - Comparison of Zero- and Two- Equation Turbulence Models. AIAA Paper 93-0779, 1993.

[42] N. Narayanswami, D. Knight, S. Bogdonoff, and C. Horstman. Interaction Between Crossing Oblique Shocks and a Turbulent Boundary Layer. *AIAA Journal*, 30:1945–1952, 1992.

[43] N. Narayanswami, D. Knight, and C. C. Horstman. Investigation of a Hypersonic Crossing Shock Wave / Turbulent Boundary Layer Interaction. *Shock Waves*, 3:35–48, 1993.

[44] D. Reddy. 3-D Navier-Stokes Analysis of Crossing, Glancing Shocks/Turbulent Boundary Layer Interaction. AIAA Paper 91-1758, 1991.

[45] P. Rodi, D. Dolling, and D. Knight. An Experimental/Computational Study of Heat Transfer in Sharp Fin Induced Turbulent Interactions at Mach 5. AIAA Paper 91-1764, 1991.

[46] W. Rodi. Experience with Two-Layer Models Combining the $k - \epsilon$ with a One-Equation Model Near the Wall. AIAA Paper 91-0216, 1991.

[47] P. Roe. Approximate Riemann Solvers, Parameter Vectors, and Difference Schemes. *Journal of Computational Physics*, 43:357–372, 1981.

[48] L. Rosenhead, editor. *Laminar Boundary Layers*, pages 46–113. Oxford, New York, 1963.

[49] S. Sarkar, G. Erlebacher, M. Hussaini, and H. Kreiss. The Analysis and Modelling of Dilatational Terms in Compressible Turbulence. *Journal of Fluid Mechanics*, 227:473–493, 1991.

[50] G. Settles, C. Horstman, and T. McKenzie. Experimental and Computational Study of a Swept Compression Corner Interaction Flowfield. *AIAA Journal*, 24:744–752, 1986.

[51] P. Spalart. Direct Simulation of a Turbulent Boundary Layer up to $Re_\theta = 1410$. *Journal of Fluid Mechanics*, 187:61–98, 1988.

[52] C. Speziale, R. Abid, and E. Clay Anderson. A Critical Evaluation of Two-Equation Models for Near Wall Turbulence. AIAA Paper 90-1481, 1990.

[53] F. White. *Viscous Fluid Flow*. McGraw Hill, New York, 1974.

[54] D. C. Wilcox. A Half Century Historical Review of the $k - \omega$ Model. AIAA Paper 91-0615, 1991.

[55] D. C. Wilcox. Application of Low Reynolds Number Two-Equation Turbulence Models to High Reynolds Number Flows. International Conference on Near-Wall Turbulent Flows, March 1993.

[56] D. C. Wilcox. *Turbulence Modelling for CFD*. DCW Industries, 1993.

[57] K. Williams and W. Hingst. The Effect of Varying Mach Number on Crossing, Glancing Shocks / Turbulent Boundary - Layer Interactions. AIAA Paper 91-2157, 1991.

[58] Y. Zang and D. Knight. Computation of Sharp Fin and Swept Compression Corner Shock/Turbulent Boundary Layer Interactions. AIAA Paper 89-1852, 1989.

[59] O. Zeman. Dilatation Dissipation: The Concept and Application in Modeling Compressible Mixing Layers. *Physics of Fluids A*, 2:178–188, 1990.

[60] G.-C. Zha and E. Bilgen. An Efficient Upwind Relaxation-Sweeping Algorithm for Three-Dimensional Navier-Stokes Equations, 1992.

[61] G.-C. Zha and D. D. Knight. Supersonic Flat Plate Flow Tests for 3D RSE Code. Technical Report 21, Department of Mechanical and Aerospace Engineering, Rutgers University, 1995.

[62] G.-C. Zha and D.D. Knight. Computation of 3D Asymmetric Crossing Shock Wave/Turbulent Boundary Layer Interaction Using a Full Reynolds Stress Equation Turbulence Model. AIAA Paper 96-0040, 1996.

[63] A. Zheltovodov, D. Knight, A. Maksimov, A. Shevchenko, and S. Vorontsov. Experimental Study and Computational Comparison of Crossing Shock Wave - Turbulent Boundary Layer Interaction. In *Proceedings of the International Conference on Methods of Aerophysical Research*, August 1994. Russian Academy of Sciences, Siberian Division.

Vita

Marianna Gnedin

1981-89 Attended Polytechnical Institute, St.-Petersburg, Russia. Majored in Fluid Mechanics.

1989 Diploma in Engineering, Polytechnical Institute, St.-Petersburg, Russia.

1989-1991 Research Assistant, Junior Research Scientist, Ioffe Institute for Physics and Technology, Russian Academy of Sciences, St.-Petersburg, Russia.

1992-95 Graduate work in Mechanical and Aerospace Engineering, Rutgers, The State University of New Jersey, New Brunswick, New Jersey.

1992-93 Graduate Research Assistant, Department of Mechanical and Aerospace Engineering.

1993 Teaching Assistant, Department of Mechanical and Aerospace Engineering.

1994-95 Graduate Research Assistant, Department of Mechanical and Aerospace Engineering.

1995 M.Phil. in Mechanical and Aerospace Engineering, Rutgers, The State University of New Jersey.

1996 Ph.D. in Mechanical and Aerospace Engineering, Rutgers, The State University of New Jersey.

Publications

M. Gnedin and D. Knight, "A Reynolds Stress Equation Turbulence Model for Compressible Flows. Part I: Flat Plate Boundary Layers", AIAA Paper # 95-0860, 33-rd Aerospace Sciences Meeting, Reno, Nevada (1995).

M. Gnedin, D. Knight, A. Zheltovodov, *et al* " A Numerical Study of 3-D Crossing Shock Wave - Turbulent Boundary Layer Interaction", submitted to AIAA 27-th Fluid Dynamics Meeting, New Orleans, LA (1996).

D. Knight, M. Gnedin, A. Zheltovodov, *et al* "3-D Crossing Shock Wave - Turbulent Boundary Layer Interaction", in preparation.